UNIVERSITY OF COPENHAGEN

# Studies of the magnetic properties of $Al(OH)_3$-based layered double hydroxides

MASTER PROJECT

*Rasmus Tang Christiansen*

December 21, 2020

Supervised by
Kim Lefmann

Co-supervisor
Ulla Gro Nielsen

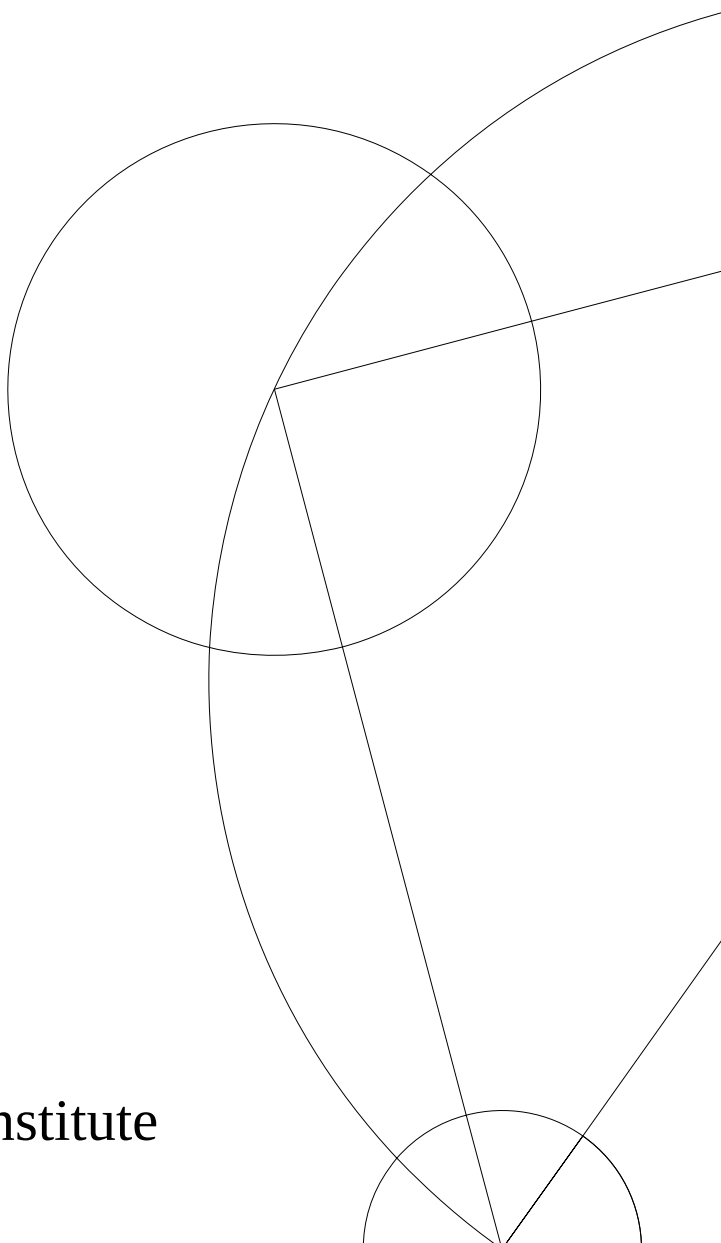

Niels Bohr Institute

# Abstract

In this work, I study a series of $Al(OH)_3$-based layered double hydroxides (LDHs) with $Cu^{2+}$, $Ni^{2+}$ and $Co^{2+}$ as cations. They respectively carry $S = 1/2$, $S = 1$ and $S = 3/2$, which allows me to study the influence of different spin quantum number on otherwise isomorph compounds. Furthermore, the cations are organised in chains, which makes them inherently interesting to study from a quantum mechanical point of view, as quantum effects are more pronounced in the low-dimensional case.

I studied their magnetic properties, which were previously unexplored, through bulk susceptibility and heat capacity measurements. They clearly revealed that none of the three variants order magnetically at $T \geq 2$ K. Modelling of the experimental data predicted that Cu-LDH is a ferromagnetic $S = 1/2$ spin chain with $J = 1.4(3)$ K, and that Co-LDH is mainly governed by a strong zero-field splitting of size $D = 138^{+5}_{-3}$ K with a weak antiferromagnetic exchange of $J \approx -0.1$ K. The predictions on Ni-LDH were less clear cut. I was able to reproduce the data both with pure ZFS and pure exchange models, which respectively yielded $D = -24$ to $-8$ K and $J = 1$ to 4 K depending on the model.

To study Ni-LDH more in-depth, neutron diffraction and spectroscopy experiments were carried out. Diffraction confirmed the absence of magnetic order down to $T = 1.6$ K. In addition, I found no signs of emerging order in the form of magnetic critical scattering, which tells than an eventual ordering temperature will be much lower than $T = 1.6$ K. Spectroscopy found a substantial zero-field splitting of $D = 9.59(2)$ K; a value somewhat different from the modelling prediction. Thus, further modelling of Ni-LDHs properties and more experiments are necessary for unravelling it's true nature.

# Acknowledgements

I owe a range of people my most sincere gratitude for their assistance through my thesis work. Even though this has been an individual project, it is beyond doubt that several individuals have helped shaping the final product.

First and foremost, I want to thank my primary supervisor, Kim Lefmann. At this point, I have worked in close collaboration with Kim for the majority of my time at the University of Copenhagen, and I do not regret it one bit. Aside from his excellent advise and support, he is, on the personal level, a fantastic individual who cares deeply for his students and always goes out of his way to make them feel welcome. For this, I am truly grateful.

Secondly, I want to thank my collaborators at the University of Southern Denmark, Ulla Gro Nielsen and Anders Bruhn Arndal Andersen. Without them, this project would not have seen the light of day, as it is their chemical expertise which lead to the synthesis of the samples I have studied. In addition, I want to thank Anders for our great discussions about our concurrent work on the LDHs, and to thank Ulla for her, at times, more cash supervision, which helped me to work my hardest and do my very best.

I have been lucky to work with a lot of different data during my thesis work, and I owe several people my thanks for that. I want to thank Kasper Steen Pedersen from the Technical University of Denmark, who was so kind to not only make his laboratory available to me, but also to help me perform my experiments. Along the same lines, I want to thank Edgar Sachs from Paris-Lodron University Salzburg, who carried out the calorimetry experiments I present in this work.

Due to the covid-19 pandemic, 2020 has been a strange year in more ways that may immediately spring to mind. We had several neutron scattering experiments planned for this work that we suddenly were not able to physically attend. Luckily, Denis Cheptiakov and Jan Peter Embs, the instrument responsibles at respectively HRPT and FOCUS at SINQ, went out of their way to make the experiments happen anyway. On top of that, I want to say a special thank you to Henrik Jacobsen, who put a lot of time and effort into assisting with these remote beam times, even if he in no way was obliged to do so.

At last, I want to thank everybody from the office on the 3rd floor of the D-building. A supportive and comfortable work environment is immensely important for ones productivity, and they certainly provided that. Even through the covid-19 pandemic, our weekly virtual group meetings were a fix-point which helped me stay sane at the home office.

# Contents

# Chapter 1

# Introduction

Materials science may be one of history's most defining scientific fields. We name most ancient historical periods after the primary material used - stone age, bronze age and iron age, and in recent history e.g. the invention of plastic and the utilisation of silicon have had a major impact on our world. Even today, materials science is thriving. In the last ten years, five Nobel prices have been awarded in relation to materials science[1–5].

The search and synthesis of new materials are generally spilt in two factions: The search for materials with unique utility and/or problem-solving abilities, and the search for realisations of good model systems with which we can test our fundamental theories and expand our overall knowledge. In this work, I cater to both these factions.

I have studied a certain kind of anionic clay, namely a family of aluminium hydroxide-based layered double hydroxides (LDHs) with the formula $M(II)Al_4(OH)_{12}SO_4 \cdot 3\,H_2O$; in the case of my work M(II)=$Cu^{2+}$ ($S = 1/2$), $Ni^{2+}$ ($S = 1$) and $Co^{2+}$ ($S = 3/2$). To our knowledge, the magnetic properties of these compounds are widely unexplored, why they are inherently interesting to study. In addition, versions of similar compounds, hydrotalcite-like LDHs, have unique anion exchange properties[6] and have found use in eq. catalysis[7], energy storage[8] and drug delivery[9], which further intrigues our interest.

Furthermore, $M(II)Al_4$-LDHs have an interesting crystal structure. They are made by inserting divalent cations (M(II)) into exactly half of the vacancies in layered $AlOH_3$, where the additional positive charge is balanced by the presence of anions ($SO_4{}^{2-}$) in the interlayers, which also contain intercalated water[10]. The result is a monoclinic unit cell shown in Figure 1.1 (left)[11], which contains parts of three cation and two anion layers. However, it is the large-scale geometry, as shown in Figure 1.1 (right), which is truly interesting. In each cation layer, the spins are organised in chains along the a-axis. They are separated by "chains" of vacancies, resulting in an interchain spacing which is $\sim 75$ % larger than the in-chain cation spacing. There are 4 bonds between cations along the chain, but 6 bonds between cations in different chains. Also, the layers are stacked such that chains of vacancies lie on top of cation chains. This gives reason to believe that these LDHs could be realizations of isomorph 1D magnetic systems with different spin.

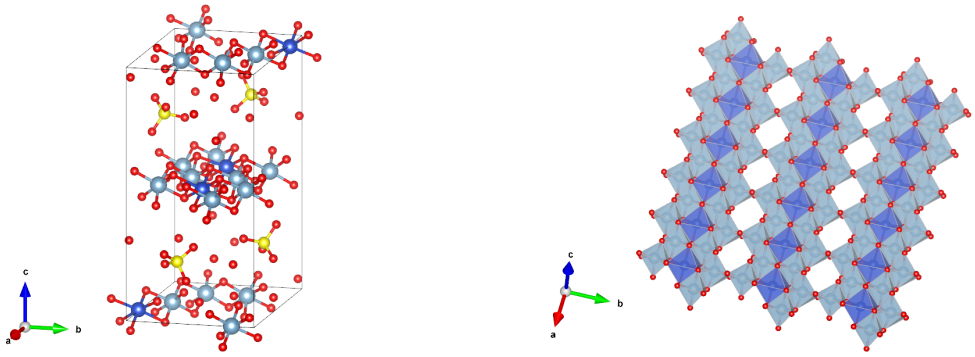

Figure 1.1: **Left:** Unit cell of M(II)$Al_4$-LDH which contains three cation layers separated by interlayers with $SO_4{}^{2-}$ and $H_2O$. **Right:** Large-scale geometry of a cation layer, which contains spin chains along the a-axis. Blue=M(II), grey=Al, red=O and yellow=S. $H_2O$ and H are omitted for clarity. Data from [11] plotted with Vesta[15].

Such low-dimensional magnetic systems are inherently interesting, since quantum mechanical effects are more pronounced in the low-D case. A prime example is the excitation continuum found in copper sulphate[12], a antiferromagnetic $S = 1/2$ spin chain. Another example is the *Mermin-Wagner theorem*, which states that the 1D isotropic spin-S Heisenberg model with finite-range exchange interaction does not order at any finite temperature[13]. Some theoretical frameworks are even able to provide accurate predictions of these quantum effects. Anderson's spin wave theory for the 2D nearest neighbour antiferromagnetic Heisenberg system on a square lattice (like the one depicted in Figure 2.1 (middle)) is a great example. He derived that it's ground state is not the Néel state, in which all spins are oriented perfectly opposite of it's neighbours, as classical theory otherwise predicts. Instead the average $\mathbf{S}_z$-value is reduced by a factor of order $1 - 0.197/S$, which is substantial for $S = 1/2$.[14]. Realizations of low-D magnetic systems in real materials as the LDHs makes it possible to test these kinds predictions, why determining their magnetic properties is important. Also, the study of isomorph compounds with different spins may provide insight into the spin's influence on the physics of these compounds.

My work investigates the magnetic properties of Cu-, Ni- and $CoAl_4$-LDH (or simply Cu-LDH etc.) with bulk measurements of magnetisation and heat capacity, as well as neutron scattering in the case of Ni-LDH. The thesis is split up into four chapters: Theory, Experimental Methods, Results and at last Discussion, Conclusion & Outlook. At first I go through the fundamentals of magnetism in materials, the theory necessary for data analysis and a short review of some previous results on 1D spin systems, which are also known as quantum spin chains (QSCs). In Experimental Methods, I briefly describe the samples I have used, the functionality of a vibrating sample magnetometer and the necessary theory on neutron scattering. In Results, I present data on each compound separately, one type of data at a time. At last, I discuss my findings before summing up the conclusions and giving my thoughts on possible further work.

# Chapter 2

# Theory

In this chapter, I present the needed theory for my thesis. This covers the origin of magnetism (inspired by Chapter 1 in [16]), relevant magnetic interactions, an introduction to fundamental magnetic ordering, a brief review of phase transitions through Landau theory and at last magnetism in materials. Then, I give some examples of ways to model the magnetic susceptibility and heat capacity of materials. In the end, I review some previous results of one-dimensional magnetism. The reader is assumed to be familiar with the basics of crystallography, reciprocal lattices and Brillouin zones as well as undergraduate quantum mechanics.

Regarding notation: It can often be confusing to differentiate between operators and symbols regarding a single electron or a whole ion. I will use lower case symbols for entities regarding electrons (e.g. will the spin be $s$), while upper case symbols will refer to entities regarding ions (e.g. $S$ for the spin of an ion).

## 2.1 Origin of Magnetism

The electron is the orgin of magnetism. It carries two kinds of angular momenta: Orbital angular momentum ($\hbar\mathbf{l}$, $\hbar$ is Planck's reduced contant) as well as intrinsic (spin) angular momentum ($\hbar\mathbf{s}$). Both of these are associated with two distinct magnetic moments

$$\boldsymbol{\mu}_o = \frac{-e}{2m_e}(\mathbf{r}\times\mathbf{p}) = -\mu_B\mathbf{l}, \qquad \boldsymbol{\mu}_s = -g\mu_B\mathbf{s} \tag{2.1.1}$$

where $m_e$ is the mass of an electron, $g = 2.0023$ is the electron g-factor and $\mu_B$ is the Bohr magneton, defined as

$$\mu_B = \frac{e\hbar}{2m_e} \tag{2.1.2}$$

where $e$ is the elementary charge. The total magnetic moment of the electron becomes $\boldsymbol{\mu} = \boldsymbol{\mu}_s + \boldsymbol{\mu}_l$. The Bohr magneton is significantly larger than the magnetic moment of an atomic nucleus, $\mu_N = \mu_B/1836$, why one can neglect the nuclear magnetic moment when considering magnetism in most materials.

Now, materials are not composed purely of electrons; they consist of atoms or ions. However, not all atoms or ions are magnetic, and we need to establish a framework that tells us which are. Magnetism is a quantum mechanical phenomenon[17], thus we need to consider the quantum mechanical electrical ground state in order to answer that question.

Assume that the electrons in an ion are subject to an attractive potential from the nucleus in addition to an average potential from neighbouring electrons, which we both consider to be spherically symmetric. In that case, the spatial eigenfunctions for the electrons are (in spherical coordinates $(r, \theta, \phi)$)[18]

$$\psi_{nlm} = R_{nl}(r)Y_l^{m_l}(\theta, \phi) \tag{2.1.3}$$

where $R_{nl}$ is the radial part and $Y_l^{m_l}$, given by the spherical harmonic functions, is the angular part. Here, $n$, $l$, and $m_l$ are the principal, orbital and magnetic quantum numbers respectively. These numbers, together with the spin quantum number $m_s$, uniquely define the electronic state of the ion.

By definition, the functions $Y_l^{m_l}$ are spherically symmetric, which we also assumed our potential to be. Therefore, the energy eigenvalues ($E_{nl}$) of an ion depend only on the quantum numbers $n$ and $l$. This leads to each eigenenergy being $2(2l+1)$-fold degenerate since $m_l$ takes $2l+1$ integer values and $m_s = \pm 1/2$. Each set of degenerate states is called an electron shell; states with $l = 0, 1, 2, ...$ corresponds to s-, p- and d-shells etc. An ion's total angular momentum is the sum of all electron momenta, $\mathbf{S} = \sum_j \mathbf{s}_j$ and $\mathbf{L} = \sum_j \mathbf{l}_j$, which also explains why an ion is only magnetic when it has one or more partially filled electron shell(s): In a closed shell, the opposite spin directions cancels out.

### 2.1.1 Ground State Selection in Magnetic Ions

Now we have established how an ion becomes magnetic and we are ready to try to determine it's ground state (GS). In principle GS selection sounds simple: Simply place the electrons in the orbitals that minimizes the ion's energy and remember Pauli's exclusion principle. Then sum up $\mathbf{S} = \sum_i \mathbf{s}_i$ and $\mathbf{L} = \sum_i \mathbf{l}_i$ and you have the magnetic moments.

However, it turns out that $\mathbf{S}$ and $\mathbf{L}$ are weakly coupled and not separately conserved due to the spin-orbit (SO) interaction, which I describe in more detail in Section 2.2.4. The SO-interaction breaks the $2(2l+1)$-fold degeneracy of the orbitals and demands the consideration of an ion's total angular momentum $\mathbf{J} = \mathbf{S} + \mathbf{L}$ in order to determine the ground state. Thus, $\mathbf{S}$ and $\mathbf{L}$ cannot be chosen independently. Luckily, a set of empirical rules known as *Hund's rules* tells us how to do that if the ion has exactly one unfilled shell. The rules are (in descending order of importance):

1. Maximize $|\mathbf{S}|$
2. Maximize $|\mathbf{L}|$
3. If the shell is more than half filled, choose $|\mathbf{J}| = L + S$. Else, choose $|\mathbf{J}| = |L - S|$

These rules are based on the assumption that the most important energy to minimize is the electrostatic repulsion between electrons, followed by their individual SO-energy. Classically speaking, the first rule prevents electrons from being packed closely together by residing in the same orbitals, while the second rule favours electrons moving in the same direction around the nucleus, thus avoiding forced crossings. The last term seeks to minimize the SO energy.

Unfortunately, Hund's rules are not always obeyed. The common example of this are the transition metal 3d ions, which are the kind of magnetic ions investigated in this thesis. In that case, measurements of the effective magnetic moment does not comply with the prediction from Hund's rules[17]; instead, they seem to favour ground states with $\mathbf{L} = 0$. This phenomenon is known as *orbital quenching* and is explained by the electron's interaction with the surrounding crystal being more significant than the SO-interaction, contrary to the underlying assumptions of Hund's rules.

To understand this from a mathematical point of view, consider the hermitian orbital angular momentum operator $\mathbf{L} = -i\mathbf{r} \times \nabla$; it is purely imaginary. If we assume that the crystal environment secures that the GS is non-degenerate, then the GS must be real. Applying the purely imaginary operator $\mathbf{L}$ to the real GS means that $\mathbf{L}$'s eigenvalues must be purely imaginary. However, $\mathbf{L}$ is a hermitian operator, so it's eigenvalues also need to be real, and the only number which is both real and purely imaginary is 0.

## 2.2 Magnetic Interactions

In this section, I will go through the most fundamental magnetic interactions, namely the dipole interaction, the Zeeman interaction, the exchange interaction and the spin-orbit interaction. For most of this section (excluding section 2.2.4), I will ignore the electron's orbital angular momentum as is often the case in literature, both for simplicity's sake and due to the fact that $\mathbf{L}$ is mostly ignorable in 3d metal ions due to orbital quenching as mentioned in the above section.

### 2.2.1 Dipole Interaction

Naturally, the first magnetic interaction to consider is the fundamental electromagnetic interaction; the dipole interaction. From electromagnetism, we know that there is an energy associated with two magnetic dipoles $\boldsymbol{\mu}_1$ and $\boldsymbol{\mu}_2$ separated by a distance $\mathbf{r}$[19]

$$E = \frac{\mu_0}{4\pi|\mathbf{r}|^3}\left(\boldsymbol{\mu}_1 \cdot \boldsymbol{\mu}_2 - \frac{3}{|\mathbf{r}|^2}\left(\boldsymbol{\mu}_1 \cdot \mathbf{r}\right)\left(\boldsymbol{\mu}_2 \cdot \mathbf{r}\right)\right) \tag{2.2.1}$$

where $\mu_0$ is the permeability of free space. Typical energies in a crystal are in the ballpark of $0.1\,\mathrm{meV}(\approx 1\,\mathrm{K})$, thus the dipole interaction is quite weak and rarely plays a rôle in the

magnetism of materials. However, in materials where other interactions are also weak, it can play a significant rôle at the lowest temperatures.[17]

### 2.2.2 Zeeman Interaction

Next, we consider how a magnetic moment $\boldsymbol{\mu}$ interacts with a static magnetic field $\boldsymbol{B}$, also known as the *Zeeman interaction*. It is perhaps the simplest magnetic interaction and is given by the Hamiltonian[18]

$$\mathcal{H} = -\boldsymbol{\mu} \cdot \mathbf{B} = -g\mu_B \mathbf{S} \cdot \mathbf{B} \tag{2.2.2}$$

From this equation, one finds that only the magnitude of the magnetic moment and it's orientation with respect to the magnetic field determines the energy.

The Zeeman Hamiltonian is quite easy to solve, and it's solution is the so-called *Larmor Precession* in which the magnetic moment precesses around the $B$-field at a constant angle (determined by the initial conditions) with an angular frequency $\omega$ depending of the field strength as $\hbar\omega = g\mu_B B$.

### 2.2.3 Exchange Interaction

Let us now consider what is often the dominating magnetic interaction in materials, namely the exchange interaction. In phenomenological terms, the origin of the exchange interaction is the overlap between neighbouring electron orbitals.

In a more thorough manner, let us start by considering two ions with spatial coordinates $\mathbf{r}_1$ and $\mathbf{r}_2$ respectively. From quantum mechanics we know such a two-particle (doublet) system splits up in singlet and triplet states with wave functions[18]

$$\Psi_S = \frac{1}{\sqrt{2}} \left(\psi_a(\mathbf{r}_1)\psi_b(\mathbf{r}_2) + \psi_a(\mathbf{r}_2)\psi_b(\mathbf{r}_1)\right) \chi_S \tag{2.2.3}$$

$$\Psi_T = \frac{1}{\sqrt{2}} \left(\psi_a(\mathbf{r}_1)\psi_b(\mathbf{r}_2) - \psi_a(\mathbf{r}_2)\psi_b(\mathbf{r}_1)\right) \chi_T \tag{2.2.4}$$

where the $\psi$'s are the single-electron states and $\chi$ is the spin part of the wave function. By definition the energy difference between these two states are[17]

$$E_S - E_T = 2 \int \mathrm{d}\mathbf{r}_1 \mathrm{d}\mathbf{r}_2 \psi_a^*(\mathbf{r}_1)\psi_b^*(\mathbf{r}_2)\mathcal{H}\psi_a(\mathbf{r}_2)\psi_b(\mathbf{r}_1) \tag{2.2.5}$$

which is also know as the *overlap integral*. Now realise that this difference can be parametrised by the operator $\mathbf{S}_1 \cdot \mathbf{S}_2$ for the doublet system, which has eigenvalues $-3/4$ and $1/4$ for the singlet and triplet state respectively[18], yielding

$$\mathcal{H} = \frac{1}{4}\left(E_S + 3E_T\right) - \left(E_S - E_T\right)\mathbf{S}_1 \cdot \mathbf{S}_2 \tag{2.2.6}$$

which gives the correct energies for both the singlet and triplet state. If we define $J \equiv \frac{1}{2}(E_S - E_T)$ and ignore constant terms we then obtain

$$\mathcal{H} = -2J\mathbf{S}_1 \cdot \mathbf{S}_2 \tag{2.2.7}$$

which is the effective Hamiltonian for the exchange interaction between two ions. Notice that the interaction is essentially determined by $J$, which is a parametrization of the overlap of the single-particle states. $J$ is denoted the *exchange constant* and is determined experimentally for most materials (more on that in Section 2.4.3), since the integral in eq. (2.2.5) can be difficult to solve even approximately.

The exchange Hamiltonian can be generalized to a many-body case by summation, which is known as the Heisenberg model

$$\mathcal{H} = -\sum_{i,j} J_{ij}\mathbf{S}_i \cdot \mathbf{S}_j \tag{2.2.8}$$

where $J_{ij}$ is the exchange constant between an ion with magnetic moment $\mathbf{S}_i$ situated at $\mathbf{r}_i$ and an ion with magnetic moment $\mathbf{S}_j$ situated at $\mathbf{r}_j$. The factor 2 is removed because the summation counts each bond twice. Most often, one assumes an isotropic nearest neighbour (NN) interaction in which case the above equation reduces to

$$\mathcal{H} = -J\sum_{i,j} \mathbf{S}_i \cdot \mathbf{S}_j \tag{2.2.9}$$

where $J$ is the isotropic exchange constant between all NNs. The sign of $J$ has a paramount influence on the magnetic behaviour of materials, which will be described in detail in Section 2.3

### 2.2.4 Spin-Orbit Interaction

At last, let me not ignore the orbital angular momentum any longer. In fact, it turns out that there is an interaction between the spin and orbital angular momentum of a single electron, namely the spin-orbit (SO) interaction. Consider for simplicity a single electron (with velocity $\mathbf{v}$) orbiting a nucleus (with charge $ze$) at a distrance $r$. In the rest frame of the electron, the nucleus will be orbiting the electron with velocity $-\mathbf{v}$. I this rest frame, the moving charge gives rise to a magnetic field given by [17]

$$\mathbf{B} = \frac{ze}{cr^3}\mathbf{r} \times \mathbf{v} = \frac{ze\hbar}{m_e r^3}\mathbf{l} \tag{2.2.10}$$

where $m_e$ is the electron mass and $\hbar\mathbf{l}$ is the orbital angular momentum of the electron. Inserting this into the Zeeman Hamiltonian (eq (2.2.2)) yields the SO Hamiltonian for a single electron:

$$\mathcal{H} = \frac{2zg\mu_B^2}{r^3}\mathbf{s} \cdot \mathbf{l} = \lambda \mathbf{s} \cdot \mathbf{l} \tag{2.2.11}$$

were $\lambda$ is the SO-parameter. The result may seem innocent at first, but when one realises that neither $\mathbf{s}$ nor $\mathbf{l}$ commutes with the Hamiltonian anymore, the significance becomes clear: $m_s$ and $m_l$ are no longer good quantum numbers, which means that one cannot choose $m_s$ and $m_l$ independently to obtain the ground state[18]. Instead, the operator $\mathbf{J} = \mathbf{S} + \mathbf{L}$ commutes with the Hamiltonian and $L+S$, $L+S-1$, ..., $|L-S|$ are the new quantum numbers. This makes it necessary to revisit the definition of the ion's magnetic moment from Section 2.1, which becomes $\boldsymbol{\mu} = g_J \mu_B \mathbf{J}$. Assuming $g_s = 2$ one can show that[17]:

$$g_J = \frac{3}{2} + \frac{S(S+1) - L(L+1)}{2J(J+1)} \tag{2.2.12}$$

## 2.3 Magnetic Order and Phase Transitions

In this section I will describe the fundamental para-, ferro- and antiferromagnetic phases, and how the exchange interaction (Section 2.2.3) is related to those. I will also present *Landau theory*, a mathematical framework that can shed light on the temperature dependence of phase transitions, which will be used to discuss transition from 1D to 3D magnetism in materials.

A fundamental entity when dealing with phase transitions is the *order parameter* (OP). An OP is a function on the outer circumstances, e.g. temperature or pressure, and is chosen such that it is zero when a model prefers one kind of ground state (the disordered state). When tuning the outer parameters, e.g. by cooling or applying pressure, one can change the phase, like when water freezes. In that case, the OP governing the liquid-solid transition will spontaneously become non-zero at $T = 0$ °C.

### 2.3.1 Fundamental Magnetic Phases

Perhaps the most commonly known magnetic phase is ferromagnetism (FM), named after the Latin name for iron (ferrum). Despite giving rise to macroscopic phenomena like permanent magnets, ferromagnetism has a microscopic origin like all types of magnetism. In a ferromagnet the magnetic moment of all ions on the lattice point in the same direction as sketched in Figure 2.1 (left). The order parameter in question is the magnetization per unit volume, $M$. In other words, a ferromagnet will have a finite macroscopic magnetization. From the minus sign in the Heisenberg Hamiltonian, eq. (2.2.9), one finds that a FM ground state will correspond to a positive exchange constant $J$.

Another common magnetic phase is the antiferromagnetic phase (AFM), depicted in Figure 2.1 (middle). In a classical AFM, each magnetic moment will point opposite it's neighbours. One can view this case as a combination of two FM sublattices with opposite magnetization, shown in Figure 2.1 (middle) in red and black respectively. For an AFM,

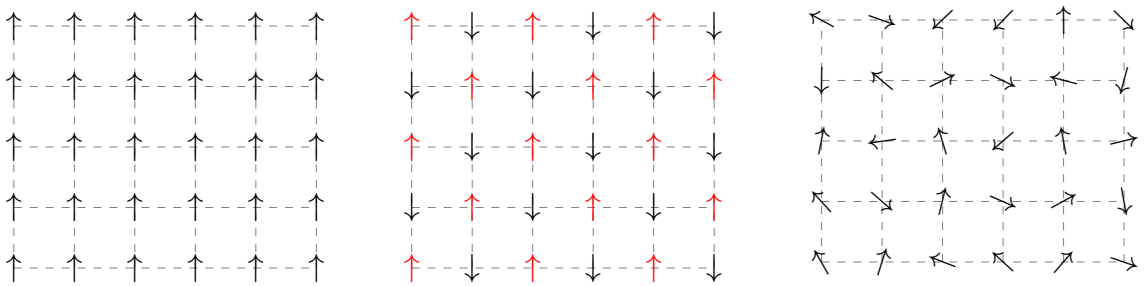

Figure 2.1: Sketch of FM (left), AFM (middle) and PM (right) states on a quadratic lattice with magnetic moments represented by arrows. In the FM case, all spins point in the same direction, while all spins point opposite it's neighbours in the AFM case. For the AFM case, the up and down sublattices are shown as respectively red and black arrows. In the PM phase, spins have a random orientation.

the order parameter is the staggered magnetization, $M_s = M_+ - M_-$, the difference in magnetization between the two sublattices. An AFM ground state will correspond to a negative exchange constant, again due to the minus sign in eq. (2.2.9).

Both types of magnetic order described above share a common feature: They both only exist at sufficiently low temperatures. At large enough temperatures it becomes easier to lower the system's entropy than to lower it's energy, and the ordered phases are destroyed. Instead, the spins become disordered and fluctuate uncorrelatedly in what is known as the paramagnetic (PM) state (Figure 2.1 (right)). Despite the disorder, the interactions described by eq. (2.2.9) are still present - They are simply not strong enough compared to the thermally induced fluctuations to produce an ordered phase. However, a material is still often referred to as "ferromagnetic" or "antiferromagnetic", depending on the sign of $J$ for the material in question, even if it is not in the ordered phase.

Magnetic order is often described by an ordering vector $\mathbf{Q}$. Such a description requires one to use the Fourier transformed version of the Heisenberg Hamiltonian [16]

$$\mathcal{H} = -\frac{1}{2}\sum_{\mathbf{q}} J(\mathbf{q})\mathbf{S}_{\mathbf{q}} \cdot \mathbf{S}_{-\mathbf{q}} \tag{2.3.1}$$

where the Fourier-transformed spins are defined as $\mathbf{S}_{\mathbf{q}} = (N)^{-1/2}\sum_j \mathbf{S}_j \exp(i\mathbf{q}\cdot\mathbf{r}_j)$ and $J(\mathbf{q}) = \sum_\delta J_\delta \exp(i\mathbf{q}\cdot\mathbf{r}_\delta)$ with $\delta$ running over neighbours relative to a spin placed at $\mathbf{r}_j$. The main consequence of this is that the system's energy is given by $E_{min} = -NS^2J(\mathbf{q})$, thus there exists a particular $\mathbf{q} = \mathbf{Q}$ which maximises $J(\mathbf{q})$ and thereby minimises the energy [20]. Thus the ground state has $\mathbf{q} = \mathbf{Q}$, which corresponds to a particular structure found from the inverse Fourier transform of $S_{\mathbf{q}}$. When $\mathbf{Q} = 0$ minimises the energy FM order is realised, while AFM order is appears when $\mathbf{Q}$ is at the Brillouin zone boundary. Other values of $\mathbf{Q}$ will give rise to more exotic, e.g. helical, magnetic structures [20].

### 2.3.2 Landau Theory

Landau theory, originally developed in the early 20th century by the Ukrainian physicist Lev Landau, is a mathematical framework for approximating the Helmholtz free energy of a system as a function of an order parameter and it's governing quantities, around a critical temperature $T_c$ where the system undergoes a second order phase transition [21]. Such an approximation enables expressing a system's thermodynamic quantities, e.g. magnetization or heat capacity, as a function of temperature. This is quite handy, since thermodynamic quantities are measurable. In other words, Landau theory tells us how measurables behave at a phase transition and how to recognize those transitions in experiments.
The completely general form of the Landau theory expansion is

$$F = F_0 + a(P,T)\eta + b(P,T)\eta^2 + c(P,T)\eta^3 + \cdots \tag{2.3.2}$$

where $F$ is the Helmholtz free energy, $F_0$ is the zero-point energy, $\eta$ is the order parameter, $T$ is temperature and $P$ is pressure. Landau's clever restriction is that only terms which respect the symmetries of the system in question are allowed.

#### 2nd order Landau theory for a ferromagnet

Take for example the ferromagnet in Figure 2.1 in which case $\eta = M$. Whether the collective orientation of the spins is up ($M = m$) or down ($M = -m$) should not affect the related physics since that is merely a question of coordinate choices. Therefore, all terms in eq. (2.3.2) with odd powers of $M$ should vanish, since the choice of $M$ may not alter the free energy. Approximating to the 4th order and assuming constant pressure leaves us with [22]

$$F = F_0 + a(T)M^2 + b(T)M^4 \tag{2.3.3}$$

If the above equation governs a system undergoing a transition from a disordered to an ordered state at some critical temperature $T_C$, a $M_0 \neq 0$ must exist such that $F(M_0) < F_0$ when $T < T_C$ and $F(M) \geq F_0$ for all $M$ if $T > T_C$. These criteria implies that $b > 0$, and that $a$ must change sign at $T_c$, thus $a = a_0(T - T_C)$. Inserting this into eq. (2.3.2) and minimizing with respect to $M$ yields:

$$\frac{\partial F}{\partial M} = 2a_0(T - T_C)M + 4bM^3 = 0 \qquad \Rightarrow \tag{2.3.4}$$

$$M = 0 \vee M = \pm\sqrt{\frac{-a_0(T - T_C)}{2b}} \qquad \Rightarrow$$

$$F = \begin{cases} F_0 - \frac{a_0^2}{4b}(T_C - T)^2 & \text{if } T < T_C \\ F_0 & \text{if } T > T_C \end{cases} \tag{2.3.5}$$

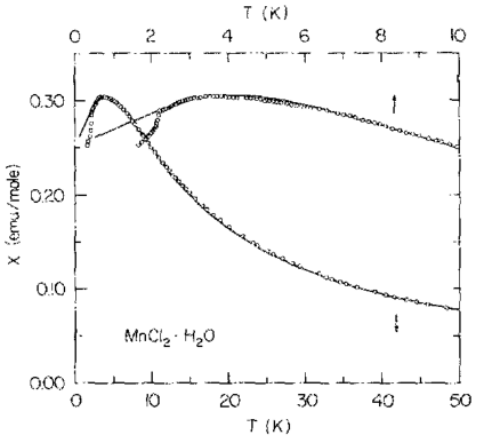


Figure 2.2: Magnetic susceptibility of polycrystalline $MnCl_2 \cdot H_2O$ measured by DeFotis et al[23] with a fit to Fisher's expression for the susceptibilty of a classical spin chain[24], scaled to the specific spin value by [25]. A clear sign of transition to 3D order from 1D behaviour is seen just above $T = 2$ K.

From this expression one can derive the behaviour of the heat capacity, $C$, through the standard thermodynamic relation $C = -T\partial^2 F/\partial T^2$, which gives

$$C = \begin{cases} \frac{a_0^2 T}{2b} + C_0 & \text{if } T < T_C \\ C_0 & \text{if } T > T_C \end{cases} \tag{2.3.6}$$

where $C_0 \equiv -T\partial^2 F_0/\partial T^2$ is the zero-point heat capacity. We now arrived at an expression for a measurable quantity. We did not derive any exact values, but we found that $C$ has a discontinuity at the transition temperature. The same procedure can be used to derive an expression for the susceptibility, $\chi$, although that requires adding the term $-MH$ to eq. (2.3.3) since $\chi = \partial M/\partial H$. In this case, minimization yields

$$\frac{\partial F}{\partial M} = 2a(T)M + 4bM^3 - H = 0 \Rightarrow \tag{2.3.7}$$

$$\chi = \left(2a(T) + 12bM^2\right)^{-1} \Rightarrow \tag{2.3.8}$$

$$\chi = \begin{cases} (4a_0(T_C - T))^{-1} & \text{if } T < T_C \\ (2a_0(T - T_C))^{-1} & \text{if } T > T_C \end{cases} \tag{2.3.9}$$

which again diverges at $T_C$. Later, we will see that the expression for $T > T_C$ is equivalent to eq. (2.4.18) (the Curie-Weiss law) derived from mean field theory with $2a_0 = C^{-1}$.

I have now shown that this framework can shed light on the behaviour of thermodynamic quantities of a compound in the viscinity of a phase transitions. The above framework could also be used for an AFM by substituting $M$ with $M_s$. These two OPs obey the same symmetries, meaning the derivation would be equivalent. However, for an

AFM one would derive the thermal dependence on the staggered susceptibility, which is not directly measurable in bulk measurements.

A great example of a transition behaving like above is the transition to AFM order in $MnF_2$ which clearly shows discontinuities in both $C$[26] and $\chi$[27]. Additionally, discontinuities like the those can be used to determine transitions from quasi-1D behaviour to 3D long range order, exemplified by the transition in $MnCl_2$[23] (see Figure 2.2). All in all, this means that one should look for divergences in thermodynamic quantities when looking for phase transitions.

## 2.4 Magnetism in Materials

In this section, I will build on the theory from the previous section and dig deeper into how magnetism is realised in materials. This includes the physical mechanisms responsible for the exchange interaction, the effect from the ion's position in a crystal lattice and models for determining the exchange constant from bulk measurements of the magnetic susceptibility and heat capacity.

### 2.4.1 Superexchange

In section 2.2.3 I described the theory behind the exchange interaction. Overlap between orbitals of neighbouring magnetic ions lead to the exchange interaction parametrized by the exchange constant. However, what happens in real materials is not that simple. Most often, the orbitals do not extend far enough away from the nucleus to justify that direct overlap should be the governing mechanism, even for the far-reaching $3d-$orbitals, and for the $4f$-ions the orbitals often only reach about one tenth of the interatomic distance[17].

Instead, a kind of indirect exchange named *superexchange* is often the responsible mechanism behind exchange in ionic solids like the LDHs. The mechanism is named "super" simply because it reaches further than direct ("normal") exchange. Antiferromagnetic interactions is the most common consequence of superexchange but it can also result in a ferromagnetic interaction[17].

In the AFM case, imagine two magnetic ions with a non-magnetic ion in-between, as is the case in e.g. MnO. The Mn-ions have an unpaired electron in the outermost $d$-shell, while the O-ion has two $p$-electrons with opposite spin in it's filled outermost shell. If the unpaired electrons in the Mn-ions also have opposite spin, they can easily delocalize by residing completely on either Mn-ion, or by placing one electron from the oxygen in each unfilled Mn-orbtibal. Such delocalization reduces electrostatic repulsion between electrons, and reduces their individual kinetic energy and would not be possible if the Mn-ions had the same spin, e.g. spin-up, as the spin-up electron on the O-ion would have nowhere to go.

In reality the mechanism can be even more complicated than this. In LDHs, the shortest path between magnetic ions are M(II)–O–Al–O–M(II), thus the mechanism is not simple, but exchange is still present. In fact, exchange can also give rise to ferromagnetic interactions[17]. I will not go into more detail here, but I refer to the original papers of Goodenough[28] and Kanamori[29] for further insight.

### 2.4.2 Crystal Field Effects

Crystal field (CF) effects originate from an ion's position in a crystal lattice. In some cases the presence of a lattice favours some electron orbitals to others due to the lattice geometry. This effect is often more pronounced for the 3d metal ions, since the d-orbitals have significant angular distribution far away from the nucleus.

To understand these phenomenons on a deeper level, start by considering an octahedral environment (see Figure 2.3) which is the local environment of the magnetic ions in LDHs. They are located at the centre of the octahedra with six ligands placed at equal distances along all three axes in both directions. In the LDHs, the ligands are oxygen with p-orbitals which are distributed along the axes.

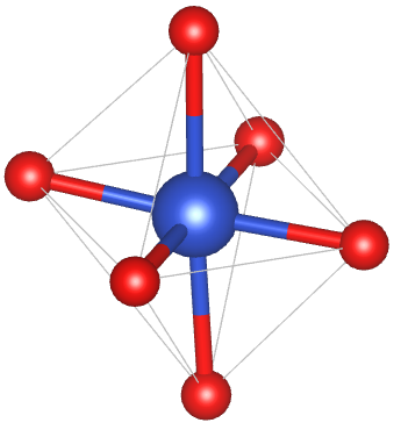

Figure 2.3: Divalent 3d metal ion (blue) in an octahedral environment surrounded by oxygen (red)[15].

The magnetic ion's outermost electrons reside in the 3d orbitals; their angular dependence is shown in Figure 2.4 (left). They can be categorized in two groups: The $t_{2g}$-orbitals ($d_{xy}$, $d_{xz}$ and $d_{yz}$), which have angular distribution between the axes, and the $e_g$-orbitals ($d_{z^2}$ & $d_{x^2-y^2}$), which have angular distribution along the local axes. Since the ligand orbitals also lie along the axes, the $e_g$-orbitals must have a larger overlap with them compared to the $t_{2g}$ ones as shown i Figure 2.4 (right), which increases electrostatic repulsion in the $e_g$ case. The result is that the orbital degeneracy from the free-ion case breaks: The three $t_{2g}$-orbitals will be lowered by an energy of $2\Delta/5$ compared to the free-ion case, while the two $e_g$-orbitals will have their energy increased by $3\Delta/5$, where $\Delta$ is the energy gap defined by the exact geometry[17].

The magnitude of the CF's effect can vary greatly. When using Hund's Rules (see Section 2.1.1), they are considered insignificant compared to the SO-interaction. However, for CF effects are immensely important for explaining orbital quenching. The really interesting case is when the CF is present and comparable to the SO-interaction. In that case the ground state still has $L = 0$, but states with $L \neq 0$ interfere with the system as a second-order perturbation[30]. The strength of such a perturbation is, among other things, determined by the energy gap between the excited states (with $L \neq 0$) and the

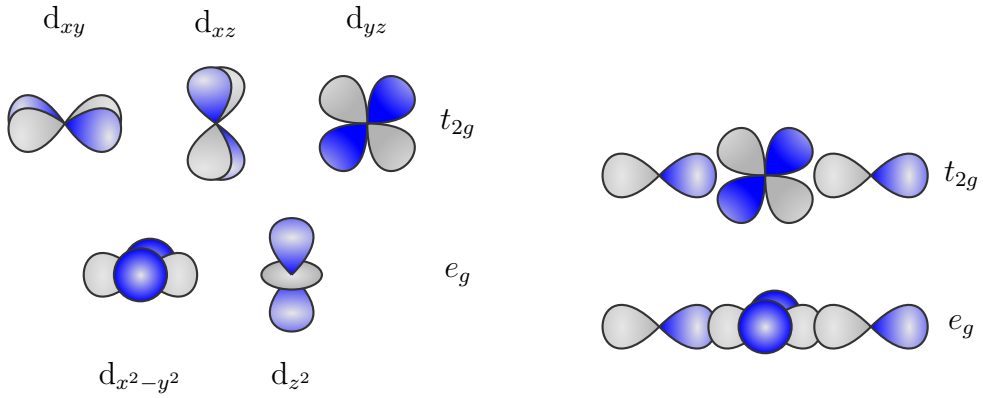


Figure 2.4: Left: Angular distribution of the 5 different d-orbitals. Right: Overlap of $t_{2g}$-orbital (top) and $e_g$-orbital (bottom) with ligand $p$-orbitals

GS[18], which is determined by the crystal field.

A case like this requires one to use an effective $B_{\text{eff}}$ in the Zeeman Hamiltonian (eq. (2.2.2)) which reflects the symmetry of the CF. In that case one gets[31]

$$\mathcal{H} = g\mu_B \mathbf{S} \cdot \mathbf{B}_{\text{eff}} = \mu_B \mathbf{S}\underline{\mathbf{g}}\mathbf{B} \tag{2.4.1}$$

where any possible anisotropy of $B_{\text{eff}}$ originating from an anisotropy of the CF is "hidden" in $\underline{\mathbf{g}}$ (the $g$-tensor). Qualitatively, this can be understood as the Zeeman effect being enhanced or suppressed when the CF "helps" or "counteracts" the external field, which may be a directional effect is the CF is anisotropic.

Sometimes, the CF can make it energetically favourable for the spin to lie along a specific crystal axis, which for each ion will add the following term to the Hamiltonian[17]:

$$\mathcal{H}_i = D\left(S_i^z\right)^2 \tag{2.4.2}$$

where $D$ is the zero-field splitting (ZFS) constant. The equation holds for an uniaxial environment, which can certainly be realised an octahedron. In that case, having $D < 0$ makes the spin prefer lying along the $z$-axis, while $D > 0$ makes it prefer the $xy$-plane. In reality, the effects of $D$ and an anisotropic $\underline{\mathbf{g}}$ can be difficult to distinguish, as they can give rise to similar phenomena. In fact, in simple perturbation theory they are interdependable as $D = \lambda(g_z - g_x)/2$, thus large SO coupling mimics the effect of the situation $g_z \gg g_x$[30].

### The Jahn-Teller Effect

The Jahn-Teller effect is in a way an the "opposite" effect compared to the ones described above: Instead of the magnetic ion being influenced by the local environment, it can itself influence the symmetry of it's local environment, *if* the ion has partially filled orbitals. Here, I sketch the basics of this effect since it has been found in Cu-LDH[11].

Consider a vibrational eigenmode, with angular frequency $\omega$, of an anion with mass $m$. A distortion, described by the parameter $Q$, of such oscillator will the have an elastic energy cost $E(Q) = \frac{1}{2}m\omega^2Q^2$ similar to a quantum harmonic oscillator[17]. In addition, the distortion $Q$ may alter the electronic energy of certain orbitals. This alteration may depend on $Q$ in a complicated manner, but if the distortion is small it can simply be approximated as Taylor series to the first order, yielding[17]:

$$E(Q) \approx \frac{1}{2}m\omega^2Q^2 \pm AQ \tag{2.4.3}$$

assuming $A > 0$. This will introduce a minimum of $E(Q)$ at a value $Q_0$ at which $E(Q_0) < 0$, thus making it energetically favourable to distort the local environment along a normal mode axis, e.g. by altering the length of an axis in the octahedron.

### 2.4.3 Susceptibility

A common way to determine the nearest neighbour exchange constant $J$ in a material is by measuring the magnetic susceptibility, which is a measure of a material's response to an applied magnetic and defined as[19]

$$\chi(T) = \frac{\partial M(H,T)}{\partial H} \approx \frac{M(H,T)}{H} \tag{2.4.4}$$

where $M$ is the magnetic moment per unit volume, $H$ is the applied field and the last approximation holds for so-called linear media; an assumption often made when dealing with experimental data measured at sufficient low $H$, as measuring $M(T)$ at a given $H$ is relatively simple (see Section 3.2). Our goal now is to derive an analytical expression for $M(H,T)$, and from that $\chi(T)$, for a paramagnet without NN interaction and then add the interaction afterwards, ultimately making $J$ obtainable from measurements of $\chi(T)$.

Consider first that the magnetization for one mole is given by $M = g\mu_B N_A m$, where $m$ is the average spin per site ($N_A$ is Avogadro's number). This means that obtaining an expression for $m$ is sufficient to obtain one for $M$. The Hamiltonian for a paramagnet in a magnetic field is simply the Zeeman Hamiltonian (eq. (2.2.2)) and thus we can use statistical physics to determine the thermal average of $m$. For reasons that become clear later, we choose to look for $m$ normalised by the total spin $S$[16]:

$$\frac{m}{S} = \frac{\sum_{m=-S}^{S} \frac{m}{S} \exp\left[-\beta\mathcal{H}\right]}{\sum_{m=-S}^{S} \exp\left[-\beta\mathcal{H}\right]} = \frac{\sum_{m=-S}^{S} \frac{m}{S} \exp\left[\beta g\mu_B mB\right]}{\sum_{m=-S}^{S} \exp\left[\beta g\mu_B mB\right]} = B_s(x) \tag{2.4.5}$$

where $\beta = (k_BT)^{-1}$, $k_B$ is Boltzmann's constant and $x = \beta g\mu_B SB$. $B_s(x)$ is the *Brillouin function* given by

$$B_s(x) = \frac{2S+1}{2S}\coth\left[\frac{2S+1}{2S}x\right] - \frac{1}{2S}\coth\left[\frac{x}{2S}\right] \tag{2.4.6}$$

which for small $x$ (thus for large T) approximates to $B_s = \frac{S+1}{3S}x + \mathcal{O}(x^3)$. Using this approximation and inserting $x$

$$\frac{m}{S} = \frac{S+1}{3S}\beta g\mu_B BS \qquad \Rightarrow \tag{2.4.7}$$

$$m = \frac{g\mu_B BS(S+1)}{3k_B T} \qquad \Rightarrow \tag{2.4.8}$$

$$\chi(T) = \frac{\partial M}{\partial H} \approx g\mu_B N_a \frac{\partial m}{\partial B} = \frac{g^2\mu_B^2 N_a S(S+1)}{3k_B T} = \frac{C}{T} \tag{2.4.9}$$

which is Curie's Law, named after the Nobel Laureate Pierre Curie who discovered it [17]. The law states that in systems where the temperature is high enough for the approximate expression for the Brillouin function to be used, and for which the thermal average is meaningful, one would expect $\chi(T)$ to be inversely proportional to $T$. However, what we are really interested in is the susceptibility of an interacting system, which I will now derive.

### Molecular Field Theory

The Heisenberg Hamiltonian can rarely be solved analytically for many-body systems, thus one has to make due with approximations. Molecular Field (MF) theory is a powerful and widely used method for dealing with such systems, and here I will use it to derive the susceptibility of the NN Heisenberg model. MF's basic assumption is that one can regard each magnetic moment as only slight deviations from some average value $\langle \mathbf{S}_i \rangle$, hence one writes $\mathbf{S}_i = \langle \mathbf{S}_i \rangle + (\mathbf{S}_i - \langle \mathbf{S}_i \rangle)$. The key here is that the fluctuations, $\mathbf{S}_i - \langle \mathbf{S}_i \rangle \equiv \delta \mathbf{S}_i$, are assumed to be small such that terms with squared fluctuations vanish. Inserting this into eq. (2.2.8) and discarding squared fluctuation terms yields

$$\mathcal{H} = -\sum_{i,j} J_{i,j}[\langle \mathbf{S}_i \rangle + \overbrace{(\mathbf{S}_i - \langle \mathbf{S}_i \rangle)}^{\delta \mathbf{S}_i}] \cdot [\langle \mathbf{S}_j \rangle + \overbrace{(\mathbf{S}_j - \langle \mathbf{S}_j \rangle)}^{\delta \mathbf{S}_j}] \qquad \Rightarrow \tag{2.4.10}$$

$$\mathcal{H} = -\sum_{i,j} J_{i,j} \left[\langle \mathbf{S}_i \rangle \langle \mathbf{S}_j \rangle + \delta \mathbf{S}_i \langle \mathbf{S}_j \rangle + \langle \mathbf{S}_i \rangle \delta \mathbf{S}_j + \cancel{\delta \mathbf{S}_i \delta \mathbf{S}_j}\right] \qquad \Rightarrow \tag{2.4.11}$$

$$\mathcal{H} = -\sum_{i,j} J_{i,j} \left[\langle \mathbf{S}_i \rangle \langle \mathbf{S}_j \rangle + \mathbf{S}_i \langle \mathbf{S}_j \rangle - \langle \mathbf{S}_i \rangle \langle \mathbf{S}_j \rangle + \langle \mathbf{S}_i \rangle \mathbf{S}_j - \langle \mathbf{S}_i \rangle \langle \mathbf{S}_j \rangle\right] \qquad \Rightarrow \tag{2.4.12}$$

$$\mathcal{H} = -\sum_{i,j} J_{i,j} \left[\mathbf{S}_i \langle \mathbf{S}_j \rangle + \langle \mathbf{S}_i \rangle \mathbf{S}_j - \langle \mathbf{S}_i \rangle \langle \mathbf{S}_j \rangle\right] \tag{2.4.13}$$

where the last term is constant and is ignored going forward. By symmetry, all $\langle \mathbf{S}_j \rangle$ have to be equivalent. Therefore the Hamiltonian splits up into a sum of single-spin Hamiltonians, $\mathcal{H} = \sum_i \mathcal{H}_i$. I now consider just the i'th spin, which will have the single-spin Hamiltonian:

$$\mathcal{H}_i = -2\mathbf{S}_i \sum_j J_{i,j} \langle \mathbf{S}_j \rangle \equiv g\mu_B \mathbf{S}_i \cdot \mathbf{B}_{MF}, \quad B_{MF} = \frac{-2}{g\mu_B} \sum_j J_{ij} \langle \mathbf{S}_j \rangle \tag{2.4.14}$$

where $\mathbf{B}_{MF}$ is the molecular field experienced by the i'th spin originating from all other spins. The factor of 2 is re-established since we still need to count each bond twice and the summation is now running over nearest neighbours. If exchange is assumed to be isotropic and with NNs only one gets $B_{MF} = \frac{-2zJm}{g\mu_B}$ where $z$ is the number of NNs and $m$ is the average spin magnitude per site. Summing this new Hamiltonian over all sites will then give the final MF Hamiltonian:

$$\mathcal{H} = -g\mu_B \sum_i \mathbf{S}_i \cdot (\mathbf{B} - \mathbf{B}_{MF}) \tag{2.4.15}$$

The observant reader will find that eq.(2.4.15) has the exact same form as the Zeeman interaction, only with a slight difference in the magnetic field. Thus, we can obtain the susceptibility by replacing the B-field in the derivation of Curie's law by a slightly more complicated one. Doing so will lead to the equations:

$$\frac{m}{S} = \frac{S+1}{3S}\beta(g\mu_B BS + 2zJSm) \qquad \Rightarrow \tag{2.4.16}$$

$$m = \frac{g\mu_B BS(S+1)}{3k_B}\frac{1}{T-\theta_{CW}} \qquad \Rightarrow \tag{2.4.17}$$

$$\chi(T) = \frac{\partial M}{\partial H} \approx g\mu_B N_a \frac{\partial m}{\partial B} = \frac{C}{T-\theta_{CW}} \tag{2.4.18}$$

which is the a modified version of Curie's law named the Curie-Weiss law. The Curie constant $C$ and the Curie-Weiss (CW) temperature $\theta_{CW}$ are given by

$$C = \frac{N_a}{3k_B}\mu_B^2 g^2 S(S+1), \quad \theta_{CW} = \frac{2zJS(S+1)}{3k_B} \tag{2.4.19}$$

Thus in interacting systems, where the MF approximation is valid, we still expect an inverse proportionality between $\chi$ and $T$, only slightly shifted. Recall that it is still required that the temperature is high enough that the approximate expression for the Brillouin function can be used. What this means is that extrapolating the high-T behaviour of the measurable $\chi(T)$ to low T will then allow one to determine $\theta_{CW}$ and ultimately $J$ if the spin configuration of the magnetic ions is known.

### Non-Critical Scaling Theory

In reality, simple approaches like the CW-law is not always sufficient to describe real systems. In this section, I present a framework, based on noncritical scaling theory, for modelling $\chi$ of spin-S FM chains based on the work by J. Souletie et al[32]. The approach is similar to "traditional" critical scaling theory often used for describing phase transitions, where some power law scaling of the thermodynamic quantities with a divergence at the critical temperature $T_c$ is found. However, instead of disregarding nonsingular cases ($T_c < 0$) we can use these cases to describe correlated systems without phase transitions.

Consider a system of $N_0$ units of size $\xi_0$ and magnetic moment $\mu = \sqrt{S(S+1)}$ (where I have set $g^2\mu_B^2/k_b = 1$) governed by the isotropic, ferromagnetic Heisenberg Hamiltonian (eq. (2.2.9), $J > 0$). Due to the interaction, at an appropriate temperature, the moments will begin to align and form new units of size $\xi(T)$. If the dimensionality is $d$, the volume of these units will be $\xi^d$. For a FM, $\mu$ will scale as the volume and $\chi$ will scale as $\mu$, resulting in $\chi T \propto \xi(T)^d$. The *static scaling hypothesis* then assumes that as $T$ gets lower, $\xi$ gets larger and eventually diverges as a power law [32]:

$$\frac{\xi}{\xi_0} = (1 - T_c/T)^{-\nu} = (1 - T_c/T)^{-\Theta/T_c} \tag{2.4.20}$$

with $\Theta = \nu T_c > 0$. Now $T_c$ being positive, null or negative yields different cases with equivalent thermodynamic legitimacy. Considering e.g. the $T_c < 0$ case, defining $T_k = -T_c$ and using $\chi T \propto \xi(T)^d$ together with the above one gets

$$\chi T = C(1 - T_c/T)^{-d\Theta/T_c} = C(1 + T_k/T)^{d\Theta/T_k} = C(1 + T_k/T)^{-\gamma} \tag{2.4.21}$$

with $\gamma = -d\Theta/T_k$ and where the first expression is general and the following expressions assume $T_C < 0$, which would describe a correlated system without phase transition.

In order to decide in which $T$-range the model is valid, and what sign of $T_c$ one should use, the above equation is modified:

$$\log_{10}\chi T = \log_{10} C + \log_{10}\left[(1 - T_c/T)^{-\gamma}\right] \quad \Rightarrow \tag{2.4.22}$$

$$\frac{\partial \log_{10}\chi T}{\partial T} = \frac{-\gamma}{1 - T_c/T}\frac{\partial}{\partial T}(1 - T_c/T) = \frac{\gamma T_c}{T_c - T}\frac{1}{T} \quad \Rightarrow \tag{2.4.23}$$

$$\frac{\partial \log_{10}\chi T}{\partial T}\left(\frac{1}{T}\right)^{-1} = \left(\frac{\partial T}{\partial \log_{10}\chi T}\frac{\partial \log_{10} T}{\partial T}\right)^{-1} = \left(\frac{\partial \log_{10} T}{\partial \log_{10}\chi T}\right)^{-1} \quad \Rightarrow \tag{2.4.24}$$

$$\frac{\partial \log_{10} T}{\partial \log_{10}\chi T} = -\frac{T - T_c}{\gamma T_c} \tag{2.4.25}$$

which predicts a linear relationship between $\partial \log_{10}(T)/\partial \log_{10}(\chi T)$ and $T$ as long as the model is valid (note that the sign in eq. (2.4.25) is different from [32], correcting a typo in the article). The authors of [32] then numerically calculated $\chi(T)$ for a series of finite rings of FM spins using an adapted variant of the Bonner-Fisher method [33]. They found that $\partial \log_{10}(T)/\partial \log_{10}(\chi T)$ is linear down to some temperature $T_s$ which depends on the ring size, from that extrapolating the model limit to $k_b T > 0.1J$. Regardless of ring size, extrapolation of the linear regime always intersected the $T$-axis at $T < 0$, telling that $T_c < 0$ is the correct approach. This allows $T_k$ to be parametrized as $T_k = \Theta JS(S+1)$ ($J$ is the exchange constant and $g^2\mu_B^2/k_b = 1$) which gives

$$\chi T = C\left(1 + \Theta JS(S+1)/T\right)^{-\gamma} \tag{2.4.26}$$

They obtained the values $\Theta = 0.6$ and $\gamma = -1.25S$ from the fitting the numerical data, which yields the expression

$$\chi(T) = \frac{g^2 S(S+1)}{8T}\left(1 + 0.6J(S+1)/T\right)^{1.25S} \tag{2.4.27}$$

in emu/(mol Oe). Since this model, if $J$ is small, is valid to low temperatures compared to the CW model, one can use mean-field theory to model an AFM interchain interaction emerging at low T, treating it as a pertubation (again in emu/(mol Oe)[34]:

$$\chi' = \chi \left(1 - \frac{16zj}{3g^2}\chi\right)^{-1} \tag{2.4.28}$$

where $j \leq 0$ is the interchain exchange constant and $z$ is the number of neighbouring chains. Such interchain interactions can possibly be caused by dipolar interaction[35].

The non-critical scaling model has two main benefits compared to the traditional CW approach: It is less restrictive when it comes to the viable temperature range, and it allows the addition of an AFM interchain interaction. As will be shown in Section 4.1 the scaling model in fact proved to be a better fit to data than the Curie-Weiss model.

#### Zero-Field Splitting

In some cases, the single-ion environment can single-handedly determine the susceptibility, parametrised by the ZFS-parameter $D$ (see eq. (2.4.2)). The model I present here assumes an axial ZFS, and is derived by Boča[30] using second order perturbation theory under the assumptions that the first-order correction due to the spin-orbit coupling is zero, and that $D \gg g\mu_B B$, where $B$ is an applied field. Adapting Boča's results to isotropic expressions for $S = 1$ and $S = 3/2$ for use with polycrystalline data yields:

$$\chi_{S=1} = \frac{2N_A\mu_0\mu_B^2}{3k_BT(1+2d)}\left[g_\perp^2\frac{2k_BT}{D}(1-d) + g_\parallel^2 d\right] \tag{2.4.29}$$

$$\chi_{S=3/2} = \frac{N_A\mu_0\mu_B^2}{3k_BT(1+d^2)}\left[g_\perp^2\left(2 + \frac{3k_BT}{2D}(1-d^2)\right) + g_\parallel^2\frac{1+9d^2}{4}\right] \tag{2.4.30}$$

where $d = \exp\left[-D/k_bT\right]$ and the $g$'s are defined in relation to the uniaxial environment. I give no expression for $S = 1/2$, as such systems cannot have a ZFS.

### 2.4.4 Heat Capacity

Now, we turn to another thermodynamic quantity, namely the heat capacity, $C$. Note that, contrary to the susceptibility, heat capacity is not a purely magnetic phenomenon; in real compounds, things like lattice vibrations may also contribute to $C$. This is important, since I will only deal with magnetic heat capacity $C_m$ in this section. In experiments, one can extract $C_m$ from the measured heat capacity $C_1$ by also measuring the heat capacity $C_2$ of a non-magnetic isomorph and use $C_m \approx C_1 - C_2$.

No general solution for $C_m$ of Heisenberg systems have been found, but both low- and high-T approximations have been successful. In the low-T limit, spin wave theory (see Section 2.5) provides good insight into the thermal dependence of the thermodynamic

quantities. While SWT is derived for an ordered system, it is still often used to approximate disordered systems. A general SWT result is that $C \propto T^{d/n}$, where $d$ is the system dimensionality and $n$ is the exponent of the wave number in the SW dispersion relation $\omega \propto q^n$, which leads to $C \propto T$ for the AFM QSC and $C \propto T^{1/2}$ for the FM QSC[36].

In the high-$T$ limit, series expansions in $\beta = (k_b T)^{-1}$ of the partition function, $Z$, has proved to successfully provide expressions for $C_m$ (from now simply $C$) analogous to the CW law. Recall that at constant pressure one has $C = \partial U/\partial T = -\partial/\partial T(\partial/\partial\beta(\ln Z))$, thus with the proper Hamiltonian one can calculate $C$ using $Z = tr\{\exp(-\beta\mathcal{H})\}$. As an example, I will now sketch the derivation of $C$ of the $S = 1$ QSC to 2nd order in $\beta$. The same procedure can be employed for other spin values, and I will present the results for $S = 1/2$ and $S = 3/2$ in the end of this section.

Let us first approximate $Z$ with $\mathcal{H}$ being the sum of the Heisenberg ($\mathcal{H}_H$, eq. (2.2.8)) and Zeeman ($\mathcal{H}_Z$, eq. (2.2.2)) Hamiltonians:

$$
\begin{aligned}
Z &= tr\{\exp(-\beta\mathcal{H})\} = tr\{\exp(-\beta(\mathcal{H}_z + \mathcal{H}_H)\} && (2.4.31)\\
&= tr\{\big(1 - \beta\mathcal{H} + \beta^2\mathcal{H}^2/2! - \beta^3\mathcal{H}^3/3! + \cdots\big)\} && (2.4.32)\\
&\approx tr\{\big(1 - \beta\mathcal{H} + \beta^2\mathcal{H}^2/2!\big)\} && (2.4.33)\\
&= (2S+1)^N - \beta\left(tr\{\mathcal{H}_H\} + tr\{\mathcal{H}_Z\}\right) + \frac{\beta^2}{2}\left(tr\{\mathcal{H}_H^2\} + tr\{\mathcal{H}_Z^2\} + 2tr\{\mathcal{H}_H\mathcal{H}_Z\}\right) && (2.4.34)
\end{aligned}
$$

where I have used the series expansion of the exponential function. Now, we need to use the raising and lowering operator form of the Heisenberg Hamiltonian, $\mathcal{H}_H = -\sum_{i,j} J_{i,j}\left(S_i^z S_j^z + 1/2(S_i^+ S_j^- + S_i^- S_j^+)\right)$, and recall that one can trace out subspaces as $tr\{\mathbf{S}_i \cdot \mathbf{S}_j\} = (2S+1)^{N-2} tr_{ij}\{\mathbf{S}_i \cdot \mathbf{S}_j\}$ and $tr\{S_i^z\} = (2S+1)^{N-1} tr_i\{S_i^z\}$.

First, I will show that the first-order term does not contribute to the trace. Assuming that the B-field is in the $z$-direction we have $H_Z = -g\mu_B B\sum_i S_i^z$. For a spin-1 system, $S^z$ has eigenvalues $-1$, 0 and 1, which means that $H_Z$ does not contribute to the first order term since $tr\{\sum_i S_i^z\} = N tr\{S_i^z\} = 0$. Also, a term can only contribute to the trace if it contains the same amount of raising and lowering operators on the same site, which is not the case for the $x$-$y$ part of $H_H$. Furthermore, the $S^z$-part of $\mathcal{H}_H$ can be factorized as $tr_{ij}\{S_i^z S_j^z\} = tr_i\{S_i^z\} tr_j\{S_j^z\}$, which does not contribute for the same reasons as $\mathcal{H}_Z$.

Now to the 2nd order terms. Again, any term with odd powers of any of the operators must vanish, why the $\mathcal{H}_Z\mathcal{H}_H$-term is discarded. Simplifying the $\mathcal{H}_Z^2$ and $\mathcal{H}_H^2$ terms yields

$$
tr\left\{\mathcal{H}_Z^2\right\} = (g\mu_B B)^2 tr\left\{\left(\sum_j S_j^z\right)^2\right\} = (g\mu_B B)^2 (2S+1)^{N-1} N tr_j\{(S_j^z)^2\} \qquad (2.4.35)
$$

$$tr\left\{\mathcal{H}_H^2\right\} = tr\left\{\left(-\sum_{i,j} J_{ij}\mathbf{S}_i\cdot\mathbf{S}_j\right)^2\right\} = (2S+1)^{N-2}\sum_{i,j} J_{ij}^2 tr\left\{\left(\mathbf{S}_i\cdot\mathbf{S}_j\right)^2\right\} \quad (2.4.36)$$

$$= 3(2S+1)^{N-2}Ntr_{ij}\left\{\left(S_i^z S_j^z\right)^2\right\}\sum_j J_{0j}^2 \quad (2.4.37)$$

where for $\mathcal{H}_H$ I have used that all cross terms like $S_i^z S_j^z S_i^y S_j^y$ vanish due to an uneven amount of raising and lowering operators on the same site and that trace is basis independent such that $tr\{(S_i^z)^2\} = tr\{(S_i^y)^2\} = tr\{(S_i^x)^2\}$. The traces are given by $tr_i\{(S_i^z)^2\} = 1^2+0^2+(-1)^2 = 2$ and $tr_{ij}\{(S_i^z S_j^z)^2\} = (1^2+0^2+(-1)^2)(1^2+0^2+(-1)^2) = 4$, which when inserting $S = 1$ results in (to 2nd order in $\beta$)

$$Z = 3^N\left[1+\frac{\beta^2}{3}N\left((g\mu_B B)^2 + 2\sum_j J_{0j}^2\right)\right] \Rightarrow \quad (2.4.38)$$

$$\ln(Z) = N\ln(3) + \frac{\beta^2 N}{3}\left((g\mu_B B)^2 + 2zJ^2\right) \quad (2.4.39)$$

where I have assumed NN interaction only ($\sum_j J_{0j}^2 = zJ^2$, $z$ is the number of NNs), used $\ln(1+x) \approx x - x^2/2$ and discarded terms with $\beta^4$. The thermodynamic quantities are then given by

$$C = \frac{\partial U}{\partial T} = -\frac{\partial}{\partial T}\left(\frac{\partial}{\partial\beta}\ln(Z)\right) = \frac{2N}{3k_b T^2}\left[(g\mu_B B)^2 + 2zJ^2\right] \quad (2.4.40)$$

$$\chi = \frac{\partial M}{\partial B} = \frac{\partial}{\partial B}\left(\frac{1}{\beta}\frac{\partial}{\partial B}\ln(Z)\right) = \frac{2N(g\mu_B)^2}{3k_b T} \quad (2.4.41)$$

where the second equation re-establishes Curie's Law for $S = 1$ (eq. (2.4.9)) when $B = 0$. For $S = 1/2$ and $S = 3/2$ the heat capacity becomes

$$C_{1/2} = \frac{N}{8k_b T^2}\left[2(g\mu_B B)^2 + 3zJ^2\right], \quad C_{3/2} = \frac{5N}{4k_B T^2}\left[(g\mu_B B)^2 + \frac{15}{4}zJ^2\right] \quad (2.4.42)$$

The general result is that regardless of spin magnitude $C \propto T^{-2}$ in zero field. Additionally, $C \propto J^2$ which means that the FM and AFM cases are equivalent.

### Zero-field Splitting

Like for the susceptibility, the heat capacity can be completely governed by single-ion effects. The crystal environment, in combination with the SO-coupling, can induce an energy gap between the singlet ($m_S = 0$) and triplet states ($m_S = \pm 1$) of a $S = 1$-ion like $Ni^{2+}$, or between the Kramer's doublets of a half-integer ion like $Co^{2+}$, which has $S = 3/2$, thus doublets with $m_S = \pm 1/2$ and $m_S = \pm 3/2$ are split.

The ground state depends on the sign of $D$ (see eq. (2.4.2)). However, as these energy levels are the only ones in consideration, it is simple to calculate their heat capacity

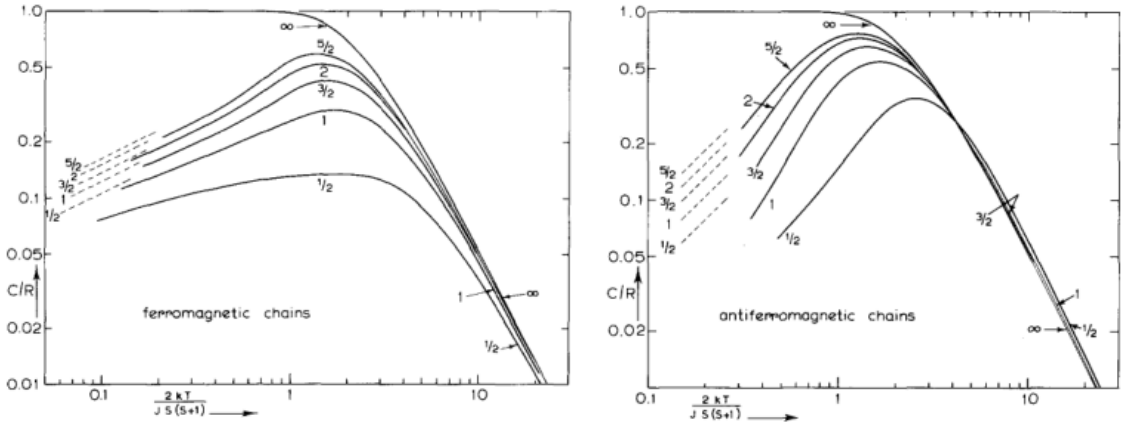


Figure 2.5: Heat capacity for FM (left) and AFM (right) Heisenberg QSCs with various spin values, extrapolated from exact diagonalization of finite chain, compared to the classical case ($S = \infty$). Dashes lines are the low-T spin wave estimate.

from the partition function like in the section above, except now approximations are not needed. The partition functions are $Z_{S=1} = 1 + 2\exp(-D/k_BT)$ and $Z_{S=3/2} = 2 + 2\exp(-2D/k_BT)$, which leads to[30]

$$C_{S=1} = 2\left(\frac{D}{k_BTZ_{S=1}}\right)^2 \exp\left(\frac{-D}{k_BT}\right) \tag{2.4.43}$$

$$C_{S=3/2} = 8\left(\frac{D}{k_BTZ_{S=3/2}}\right)^2 \left[\exp\left(\frac{-2D}{k_BT}\right) Z_{S=3/2} - 2\exp\left(\frac{-4D}{k_BT}\right)\right] \tag{2.4.44}$$

which for $D > 0$ creates sharp maxima at $T \approx 0.37D/k_B$ with amplitude $C_{max} \approx 6.3$ J/(mol K), while $D < 0$ leads to sharp maxima at $T \approx 0.45D/k_B$ with amplitude $C_{max} \approx 2$ J/(mol K). In both cases, the maxima becomes broader when $|D|$ gets larger, but $C$ always goes to zeros at $T = 0$.

### Exact Diagonalization

In intermediate temperature regions, heat capacity of QSCs has been studied through exact diagonalization (ED) of finite chains governed by the Heisenberg Hamiltonian, e.g. by Bonner & Fisher[33] for $S = 1/2$ and by Blöthe[37,38] for a variety of spin values (see Figure 2.5). From these works, two things become clear: $C$ is significantly affected by the quantum nature of these systems, and the effect becomes larger for low spin values. In all cases, $C$ shows a maximum (see Figure 2.5) at finite $T$, although the exact position and shape depends on $S$ and $J$. From Figure 2.5 it is also clear that the low-T behaviour is different from that of the classical case ($S = \infty$), thus measurements of the $C_m(T)$ can provide significant insight into the quantum nature of a compound. In the high-$T$ limit, ED re-establishes the $T^{-2}$-behaviour predicted by HTE.

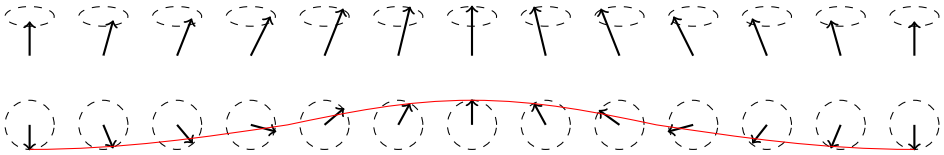

Figure 2.6: Classical picture of a spin wave excitation of a ferromagnetic chain in 3D view (top) and viewed along the quantization axis (bottom).

## 2.5 Spin Wave Theory

Spin wave theory (SWT) is the go-to framework for dealing with excitations of quantum systems on a lattice at low temperatures. SWT is derived on the basis of small deviations from the ordered classical ground state (as will be elaborated below) and therefore requires that the ground state is known for it to be exact. However, it can provide good results even if an approximate ground state is used, as exemplified by Anderson[14]. In this section, I will derive the general dispersion for FM SWs, where the ground state is the fully magnetised state, and simply state the approximate result for the AFM QSC.

The main results from SWT is that for a collection of spins, the Fourier components of the spin raising and lowering operators perform periodic motion with frequencies (and therefore energies) that are directly related to the wave vectors of the Fourier components. From the classical perspective, SW excitations can be understood as collective precession of spins in real space, exemplified for the $S = 1/2$ FM QSC in Figure 2.6, with frequencies equal to those of the periodic motion of the Fourier components. From a quantum perspective, one can think of the SW excitations as a number of flipped spins de-localised over the whole chain. Each flipped spin carries $S = 1$ an can thus be treated as a boson and follow bosonian statistics[16]. In the quasiparticle image, they are named *magnons*. As long as the number of magnons are small, they can be treated as non-interacting[16].

As will be elaborated later, it turns out that the wave vectors related to the aforementioned Fourier components are equal to the scattering vector in inelastic neutron scattering experiments. Thus, SW frequencies are directly obtainable from experiments, which is a big reason they are important.

### 2.5.1 Ferromagnetic Spin Waves

Here I will derive the dispersion of FM SWs inspired by Yosida[16]. Consider the Heisenberg Hamiltonian with a Zeeman term where the applied field $\mathbf{B}$ is along the z-axis

$$\mathcal{H} = -\sum_{i,j} J_{ij}\mathbf{S}_i \cdot \mathbf{S}_j - g\mu_B B \sum_i S_i^z \tag{2.5.1}$$

From this, one can calculate the time evolution of $\mathbf{S}_j$ through Ehrenfest's theorem as[16]

$$\hbar\frac{\mathrm{d}\mathbf{S}_j}{\mathrm{d}t} = i[\mathcal{H}, \mathbf{S}_j] = -\mathbf{B}_{\text{eff},j} \times \mathbf{S}_j \tag{2.5.2}$$

$$\mathbf{B}_{\text{eff},j} = \sum_i J_{ij}(S_i^x\hat{x} + S_i^y\hat{y} + S_i^z\hat{z}) + g\mu_B B\hat{z} \tag{2.5.3}$$

Instead of considering $\mathrm{d}\mathbf{S}_j/\mathrm{d}t$, it is more convenient to look at the time evolution of each component individually. For the three components one gets

$$\hbar\frac{\mathrm{d}S_j^x}{\mathrm{d}t} = -\hat{x}\cdot(\mathbf{B}_{\text{eff},j} \times \mathbf{S}_j) = -\sum_i J_{ij}\left(S_i^y S_j^z - S_i^z S_j^y\right) + g\mu_B B S_j^y \tag{2.5.4}$$

$$\hbar\frac{\mathrm{d}S_j^y}{\mathrm{d}t} = -\hat{y}\cdot(\mathbf{B}_{\text{eff},j} \times \mathbf{S}_j) = -\sum_i J_{ij}\left(S_i^z S_j^x - S_i^x S_j^z\right) - g\mu_B B S_j^x \tag{2.5.5}$$

$$\hbar\frac{\mathrm{d}S_j^z}{\mathrm{d}t} = -\hat{z}\cdot(\mathbf{B}_{\text{eff},j} \times \mathbf{S}_j) = -\sum_i J_{ij}\left(S_i^x S_j^y - S_i^y S_j^x\right) \approx 0 \tag{2.5.6}$$

where the approximation $\mathrm{d}S_j^z/\mathrm{d}t \approx 0$ relies on the assumption that deviations from the ordered ground state are small. That results in both $\langle S_j^x\rangle$ and $\langle S_j^y\rangle$ being small as well, why they approximately vanish to second order. In fact, they can be shown to have a time average of exactly zero[20]. Thus, $\langle S_j^z\rangle$ is a constant of motion.

It turns out that it is more illustrative to look at the derivative of the raising and lowering form of the spin operators, $S_j^\pm = S_j^x \pm iS_j^y$. Here, I derive the expression for $S_j^+$, but it can be done in a similar manner for $S_j^-$.

$$\hbar\frac{\mathrm{d}S_j^+}{\mathrm{d}t} = \hbar\frac{\mathrm{d}S_j^x}{\mathrm{d}t} + i\hbar\frac{\mathrm{d}S_j^y}{\mathrm{d}t} \tag{2.5.7}$$

$$= g\mu_B B\left(S_j^y - iS_j^x\right) - \sum_i J_{ij}\left(S_i^y S_j^z - S_i^z S_j^y + i(S_i^z S_j^x - S_i^x S_j^z)\right) \tag{2.5.8}$$

$$= -i\left[g\mu_B B S_j^+ + \sum_i J_{ij}\left(S_i^z S_j^+ - S_i^+ S_j^z\right)\right] \tag{2.5.9}$$

$$= -i\left[g\mu_B B S_j^+ + S\sum_i J_{ij}\left(S_j^+ - S_i^+\right)\right] \tag{2.5.10}$$

where in the last step I have approximated the $S_k^z$-operators by their eigenvalue $S$. This is motivated by $\langle S_j^z\rangle$ being a constant of motion and that the $B$-field secures that the quantization is along the $z$-axis. Also, the assumption of small deviations from the ground state secures that the thermal average $\langle S^z\rangle$ is close to $S$.

Now I introduce the Fourier transform of the spin raising operator

$$S_{\mathbf{q}'}^+ = \frac{1}{\sqrt{N}}\sum_j e^{i\mathbf{q}'\cdot\mathbf{r}_j} S_j^+ \tag{2.5.11}$$

which is the magnon annihilation operator and together with eq. (2.5.10) gives

$$i\hbar\frac{\mathrm{d}S^+_{\mathbf{q}'}}{\mathrm{d}t} = \frac{i\hbar}{\sqrt{N}}\sum_j e^{i\mathbf{q}'\cdot\mathbf{r}_j}\frac{\mathrm{d}S^+_j}{\mathrm{d}t} \tag{2.5.12}$$

$$= \frac{g\mu_B B}{\sqrt{N}}\sum_j e^{i\mathbf{q}'\cdot\mathbf{r}_j}S^+_j + \frac{S}{\sqrt{N}}\sum_{ij} e^{i\mathbf{q}'\cdot\mathbf{r}_j}J_{ij}\left(S^+_j - S^+_i\right) \tag{2.5.13}$$

$$= \left(g\mu_B B + S[J(0) - J(\mathbf{q}')]\right)S^+_{\mathbf{q}'} \tag{2.5.14}$$

where the last step introduces the Fourier transform of $J_{ij}$ as

$$J(\mathbf{q}') = \frac{1}{\sqrt{N}}\sum_j e^{i\mathbf{q}'\cdot(\mathbf{r}_i-\mathbf{r}_j)}J_{ij} \tag{2.5.15}$$

$$J(0) = \frac{1}{\sqrt{N}}\sum_j e^{i\mathbf{0}\cdot(\mathbf{r}_i-\mathbf{r}_j)}J_{ij} \tag{2.5.16}$$

where $J(0)$ is simply the normalised sum of all exchange parameters related to each site. The above derivation can also be performed for $S^-_j$. The last expression, eq. (2.5.14), is the differential equation for a parameter performing periodic motion with a frequency $\omega_{\mathbf{q}'}$ given by

$$\hbar\omega_{\mathbf{q}'} = g\mu_B B + S[J(0) - J(\mathbf{q}')] \tag{2.5.17}$$

and thus $S^\pm_j$ perform periodic motion. The equation right above is the spin wave dispersion relation for a ferromagnet and thus relates the frequency and energy of FM spin waves.

For a chain with nearest neighbour interactions only, one has $J(q') = J(0)\cos(q'a)$ and $J(0) = 2J$[20], where $a$ is the lattice spacing. In that case, the dispersion reduces to

$$\hbar\omega_{\mathbf{q}'} = g\mu_B B + 2JS\left(1 - \cos(q'a)\right) \tag{2.5.18}$$

which scales as $q^2$ for low $q$ and is plotted in Figure 2.7. A finite amount of energy is needed to excite the lowest-lying excitation in the presence of an external field; a phenomenon called a spin gap. Recall now from Section 2.4.2 that the presence of an uniaxial ZFS can be modelled as an addition to the external field. Thus, a spin gap can exist even in zero external field, and the gap will be given by the anisotropy field, which has a size of $B_{\text{anis}} = D(2S-1)/(g\mu_B)$[16]. Thus the gap size for e.g. a $S = 1$ FM QSC will be $D$.

### 2.5.2 Antiferromagnetic Spin Waves

AFM spin waves are generally more difficult to deal with, since the classical AFM ground state is not an eigenstate of the Hamiltonian. As mentioned above, Anderson derived an approximate dispersion relation for an antiferromagnet on the linear, square or cubic lattice using the Néel state as an approximate ground state[14]

$$\hbar\omega_{\mathbf{q}'} = g\mu_B B + dJS\sqrt{1-\gamma^2_{\mathbf{q}'}} \tag{2.5.19}$$

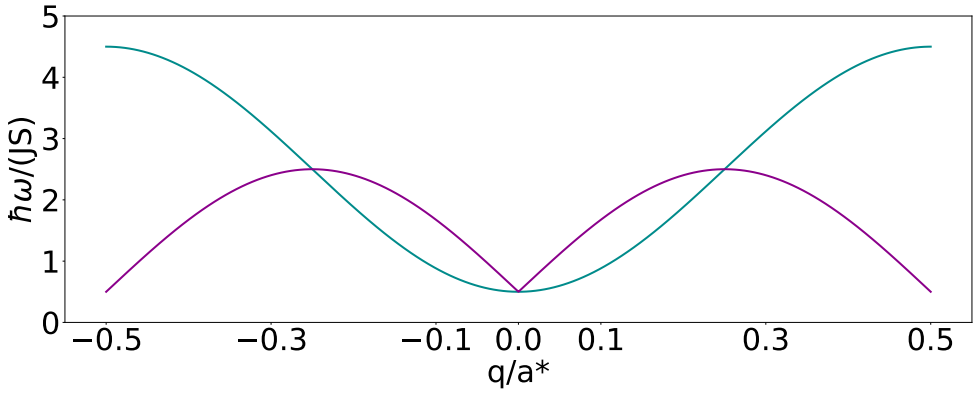


Figure 2.7: Spin wave dispersion for a FM (cyan) and an AFM (magenta) chain.

where $d$ is the dimensionality of the system and $\gamma_{\mathbf{q}'} = \sum_i^d \cos q_i'/d$, where $q_i'$ are the components of $\mathbf{q}'$. For a chain, $d = 1$ and the expression reduces to $\hbar\omega = JS\sin(q'a)$, which is plotted in Figure 2.7. For low $q$ one has that $\sin q \approx |q|$, thus AFM SWs are fundamentally different than their FM counterparts. An exact quantum mechanical solution for $d = 1$ and $S = 1/2$ was found by des Cloizeaux and Pearson [39], and for $S = 1$ by Haldane [40,41], which will be discussed briefly in the following section.

## 2.6 Quantum Spin Chain Deep Dive

Now the time has come to a take deep dive into established results on QSCs. As mentioned in the Introduction, the crystal structure of the M(II)-LDHs gives reason to believe that they could be realisations of QSCs, why familiarising oneself with previous results on the matter is useful. However, despite my best efforts, this is not close to a full overview of QSCs; emphasis has been put on the most fundamental situations relevant for the present work. For more in-depth reviews, the interested reader is referred to the papers by A. Vasiliev et al [42] or by D.S. Inosov [43].

In a way, the Heisenberg model (eq. (2.2.8)) is the most simple magnetic model; it contains no anisotropies or other fancy interactions, only spins interacting isotropically. Even so, it can still produce complicated phenomena, and a theoretical treatment most often requires approximations or numerical calculations. It turns out that for a QSC, the exact spin value and the sign of $J$ fundamentally decides it's quantum nature, which will be elaborated in this section for $S = 1/2$, $S = 1$ and $S = 3/2$ individually, which illustratively corresponds to Cu-, Ni- and Co-LDH respectively.

Despite the different spin values, some results are general. Expressions for the susceptibility ($\chi$, in the case $J > 0$) and the staggered susceptibility ($\chi_{st}$, in the case $J < 0$), both for arbitrary spin, have been derived with approximate Green's function theory [44]. It was found that both $\chi$ and $\chi_{st}$ diverge as $T^{-2}$ when $T \to 0$, and that they re-establish CW-behaviour at high $T$. Additionally, general results on the heat capacity has already

been discussed in Section 2.4.4. Another general result is that the ground state (GS) of FM chains is the saturated state as depicted in Figure 2.1 (left) regardless of spin [17], and the fundamental excitations are spin waves as discussed in the previous section.

### 2.6.1 The S=1/2 chain

Quite remarkably, the exact wave function of the isotropic $S = 1/2$ Heisenberg spin chain was found by Bethe already in 1931 [45]. This allowed Hulthén to derive the exact quantum GS of the AFM chain [46], which paved the road for des Cloizeaux and Pearson to calculate it's exact excitation dispersion $\hbar\omega = |J|\pi \sin q$ [39], complimentary to the already know dispersion of the FM chain. Again it was found that the excitations carried $S = 1$. In 1981, it was found that they *fractionalize* [47], forming pairs of $S = 1/2$ excitations. Subsequently these excitations have been named spinons.

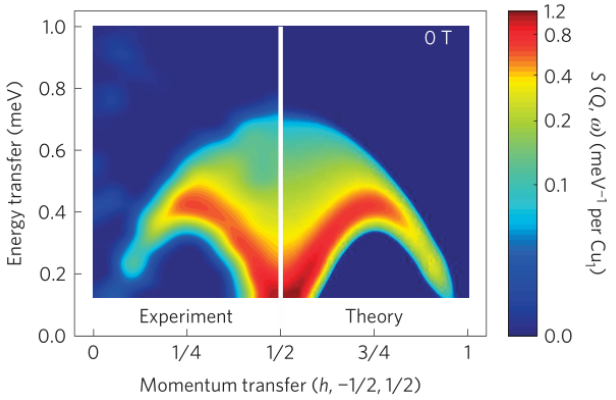


Figure 2.8: Experimental dynamical structure factor of the $S = 1/2$ AFM chain compound $CuSO_4 \cdot 5\,D_2O$ (left) measured by Mourigal et al [12], compared with theoretical two- and four-spinon dynamical structure factor (right). Figure adapted from [12].

It turns out that the excitations spectrum of the AFM chain is dominated by a two-spinon continuum, and not a single dispersion curve, thus SWT is not exact for the AFM chain [48]. The exact two-spinon excitation spectrum was derived in 1996 [49], and a four-spinon contribution was theorised in 2006 [50]. In 2013 it was verified that both two- and four-spinon excitations were needed to account for the full spectral weight of the isotropic $S = 1/2$ AFM chain compound $CuSO_4 \cdot 5\,D_2O$ [12] (see Figure 2.8). These findings rely on a quantum mechanical treatment of the $S = 1/2$ chain, thus they emphasize it's fundamental quantum nature. However, quantum effects are not present in the AFM chain only. Bethe's framework furthermore made it possible to deal with interactions among FM spin waves, and it was found that magnons can lower their energy by creating bound states [16], which has e.g. been measured in the $S = 1/2$ FM chain compound $CoCl_2 \cdot 2\,H_2O$ with infrared transmission spectroscopy [51].

Parallel to the above findings, the thermodynamics of the $S = 1/2$ chain were studied. Bonner & Fisher used exact diagonalization to study it's heat capacity ($C$) and susceptibility ($\chi$) way back in 1964 [33] for different exchange and Ising anisotropies, and Blöthe continued the work on the heat capacity ten years later [37,38] (see Section 2.4.4). Bonner & Fisher found that the susceptibility of the AFM chain shows distinct quantum behaviour: The susceptibility is finite at $T = 0$, and a local maximum emerges at low $T$. They also

found that $\chi$ diverged as $T^{-9/5}$ as $T \to 0$, similarly to the more recent findings discussed above. In summary, the review of the Heisenberg $S = 1/2$ chain boils down to:

- The FM and AFM chains are fundamentally different. The excitations of the FM chain are magnons, while the exciations of the AFM chain are spinons.
- AFM Spinons are the fractionalization of a spin-1 excitations into two $S = 1/2$ quasiparticles, and they create an excitation continuum.
- Distinct quantum features are found in the heat capacity at low $T$, and the exact behaviour depends on the sign of the exchange interaction.
- $\chi$ of the FM chain behaves qualitatively like the $S = \infty$ at high $T$ case and diverges as $T^{-2}$ at low T.
- $\chi$ of the AFM chain has a local maximum at low T and is finite at $T = 0$.

### 2.6.2 The S=1 chain

QSCs with integer spin values turn out to be fundamentally different from their half-integer counterparts, thus they are also fundamental quantum systems. A main difference is that magnons are the fundamental excitations of both the FM and AFM chains, again with dispersions $\hbar\omega \propto cos(q)$ and $\hbar\omega \propto sin(q)$ respectively. However, the two cases are still different. The AFM chain exhibits topological order in the ground state, and has a finite energy gap of size $\Delta \approx 0.4\ |J|$ at $k = \pi$, as first predicted by Haldane in the 1980's[40,41] and later proven by Affleck et al[52]. Additionally, a single dispersion curve is not sufficient to describe the excitations of the AFM chain. A two-magnon continuum of excitations around $k = 0$ was predicted by Affleck and Weston[53] and a three-magnon contribution at $k = \pi$, above the single-magnon dispersion curve, was predicted by Horton and Affleck[54]. Evidence of these continua was found with neutron spectroscopy, the two-magnon continuum by Zaliznyak et al[55] (see Figure 2.10 (left)) and the three-magnon continuum by Kenzelmann et al[56] (see Figure 2.10 (right)).

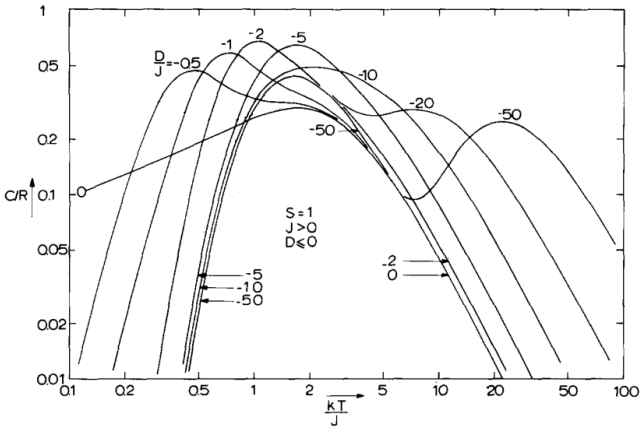


Figure 2.9: Heat capacity for FM Heisenberg QSCs with various single-ion anisotropies ($D$) causing an easy axis, extrapolated from finite chains. Figure adapted from [38].

To complement the studies already presented in Section 2.4.4, Blöthe also studied the effect of a zero-field splitting as described by eq. (2.4.2) on the heat

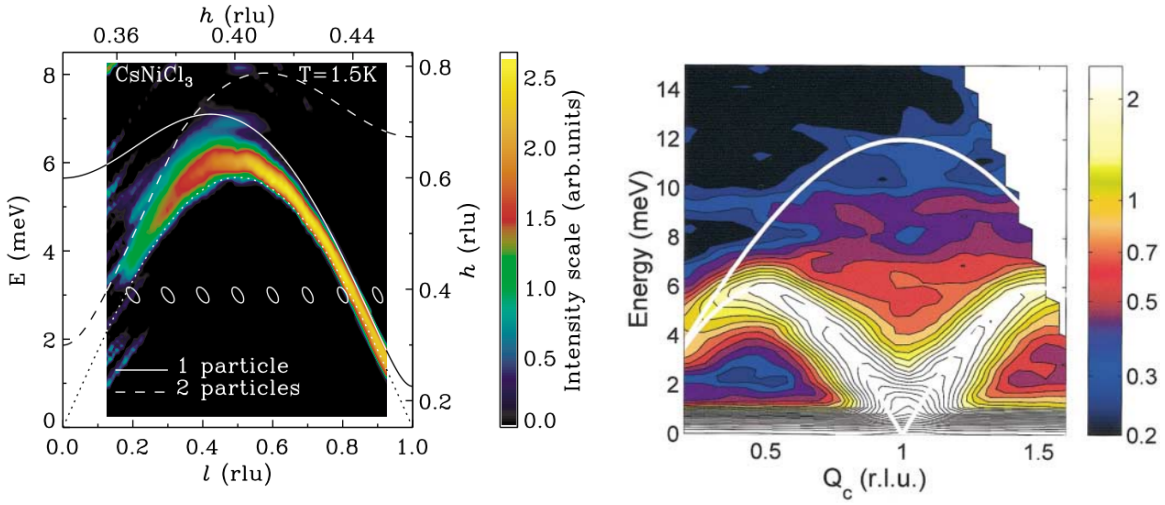


Figure 2.10: Inelastic neutron scattering intensity of the $S = 1$ AFM chain compound $CsNiCl_3$. **Left**: Two-magnon continuum at $l < 0.5$ around $E \approx 5$ meV measured by Zaliznyak et al[55]. Figure adapted from [55]. **Right**: Three-magnon continuum at $0.6 < Q_c < 1.4$ up to $E \approx 12$ meV measured by Kenzelmann et al[56]. Figure adapted from [56]

capacity[37,38] (see Figure 2.9). He found that the anisotropy causes a slight shift in position and intensity of the low-$T$ maximum, and that an additional maximum is created if the anisotropy is sufficiently large.

Approximate Green's Function theory on $\chi$ of the FM chain with a ZFS-parameter $D < 0$ has also been calculated[57]. The theory predicts suppression of the critical fluctuations, which normally prevents LRO at finite $T$, manifested as a finite critical temperature. The effect of an AFM interchain interaction between FM chains on the susceptibility have also been treated[32] (see Section 2.4.3), and was predicted to result in a local maximum in $\chi T$ before it diverges to negative values, contrary the Curie-Weiss case where $\chi T \to \infty$ as $T \to 0$ without a local maximum.
In summary, the selected results on the Heisenberg $S = 1$ chain boils down to:

- Magnons are the fundamental excitations regardless of exhange interaction.
- The AFM chain exhibits topological order in the ground state, and two- and three-magnon contributions are important to account for the whole excitation spectrum.
- The AFM spectrum is gapped at $k = \pi$ with a magnitude $\Delta \approx 0.4|J|$.
- The heat capacity shows distinct quantum features at low $T$, and the exact behaviour depends on the sign of the exchange interaction and size of single-ion anisotropy.
- $\chi$ of the FM chain diverges as $T^{-2}$ as $T \to 0$ and shows CW-behaviour as $T \to \infty$.
- For the FM chain, an AFM interchain interaction can produce a local maximum in $\chi T$ at low T and make $\chi T$ trend negative as $T \to 0$.

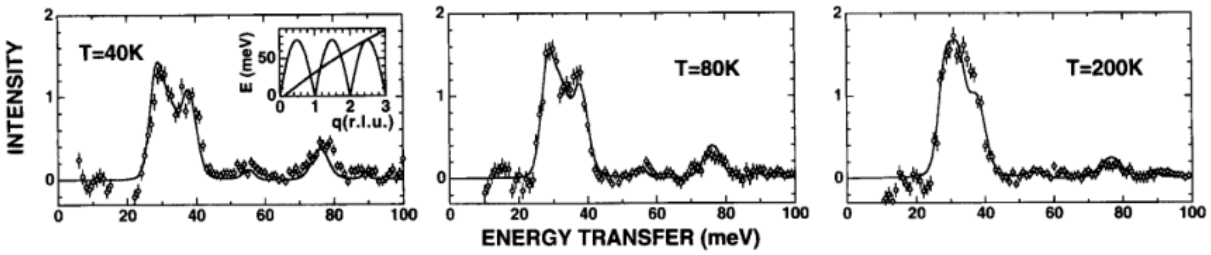


Figure 2.11: Magnetic excitation spectrum of $CsVCl_3$ at different temperatures, measured by Itoh et al[59]. The insert on the leftmost panel shows the $q$-direction of the energy scan (along the $c^*$-axis). Figure adapted from [59].

### 2.6.3 The S=3/2 chain

Since the $S = 3/2$-chain is also a half-integer chain, it behaves similarly to the $S = 1/2$-chain. However, the larger spin makes the quantum effects less pronounced, why the $S = 3/2$-chain is sometimes disregarded as a quantum system and is less studied.

Despite that, some results are present for the $S = 3/2$-chain. An excitation continuum of the AFM chain at $q = \pi$ similar to, but weaker than, the one of the $S = 1/2$-chain has been predicted by quantum Monte Carlo (QMC) methods[58]. At other $q$-values, the QMC method had insufficient accuracy to detect deviations from classical theory, which underlines that $S = 3/2$ is in fact at the quantum/classical boundary. Extrapolation of neutron spectroscopy data of the $S = 3/2$ chain compound $CsVCl_3$, performed by Itoh et al[59] (see Figure 2.11), indeed finds a finite energy width as $T \to 0$, possibly explained by the existence of an excitation continuum.

The relevant findings on the susceptibility and heat capacity have already been discussed in the beginning of this section and in Section 2.4.4 respectively. In summary it seems that the main difference between the $S = 3/2$- and the $S = 1/2$-chains is that the larger spin weakens the quantum effects.

# Chapter 3

# Experimental Methods

In this section, I present the experimental methods used for collecting data for the present work. This covers the inner workings of a vibrating sample magnetometer, some background on neutron powder diffraction and spectroscopy and an introduction to the neutron instruments used. In addition, I will briefly describe the particular samples studied for this work, which were synthesized by our collaborators at the Univ. of Southern Denmark.

## 3.1 Samples

Our M(II)-LDH samples were synthesized by Anders Bruhn Arndal Andersen at Univ. of Southern Denmark through an optimization of the procedures reported in [60]. 0.25 g bayerite, $Al(OH)_3$(s), was mixed with 20 mL of the respective $MSO_4$(aq) solutions and pH-adjusted to approx. 2 by addition of 1.8 M $H_2SO_4$(aq), whereafter they were treated hydrothermally at 120 °C in 40 ml Teflon-lined autoclaves. Two synthesis parameters were varied: The reaction time (between 3 and 14 days) and the $MSO_4$(aq) concentrations (between 0.04 and 2.8 M). The optimal conditions were found to be 14 days and 2.8 M for Co-LDH, 9 days and 0.7 M for Ni-LDH, and 14 days and 0.08 M for Cu-LDH, which resulted in phase pure Co- and Ni-LDH, and Cu-LDH containing approx. 13 %(w/w) unreacted bayerite.

A.B.A Andersen assessed the quality of the samples using the same protocol as earlier reported[60], e.g. by powder X-ray diffraction (XRPD, to examine crystalline phases), $^{27}$Al magic-angle spinning nuclear magnetic resonance (to examine the content of unreacted bayerite) and inductively coupled plasma-optical emission spectrometry (to examine bulk M:Al ratio). For the samples from the optimized synthesis, he performed Rietveld refinement of XRPD data to confirm their isostructurality with nickelalumite[61]. He used thermal gravimetric analysis to determine the interlayer water content, which were 3.3, 3.2 and 3.1 for Co-, Ni- and Cu-LDH respectively. The reader is referred to [62] for more detail on the synthesis and structural characterization.

## 3.2 Vibrating Sample Magnetometer

A vibrating sample magnetometer (VSM) measures the magnetisation induced in a sample from applying an external magnetic field. A simplified setup schematic is shown in Figure 3.1. Measurements are performed by vibrating a sample, (1), with constant frequency between two stationary sample coils, (2), in a direction perpendicular to the uniform magnetic field produced by the magnets, (3). Since the sample is magnetised by the external field, and the effective area-turns of the coils are non-symmetrically distributed about the axis of vibration, this will induce a voltage in the sample coils, which is used to deduce the magnetisation. A lock-in amplifier, locked to the frequency of vibration, extracts the induced voltage from the noisy environment.

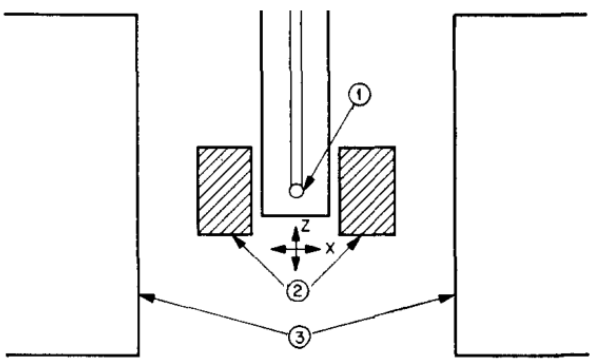

Figure 3.1: Schematic of a vibrating sample magnetometer adapted from [63]. (1) sample, (2) sample coils, (3) magnets.

To make the setup insensitive to the exact positioning of the sample, one has to carefully calibrate the setup. This is done by first rotating the sample coils around the z-axis until maximum voltage output is achieved. Then, the sample's position on the x-axis relative to the coils is adjusted to achieve minimum output, whereafter the relative y- and z-positions, one at a time, are altered to achieve maximum output. This way, a saddle point is reached, and the output should be insensitive to sample displacements.

The specific VSM used for this work is a Quantum Design VSM for the Dynacool™ physical properties measurement system (PPMS®), which performs above-mentioned the spatial calibration automatically. The full information on the equipment can be found of the data sheets[64,65], but the main features are:

- T-range 1.8 K to 400 K, ±0.1 % for $T < 20$ K and ±0.02 % for $T > 20$ K
- Field strength up to 9 T with a resolution of 0.016 mT with a field uniformity of ±0.01 % over 3 cm along the field axis
- Measurement accuracy of ±0.5 % with additional relative noise ratio of 0.5 %
- Vibration frequency of 40 Hz with an amplitude of 2 mm
- Sample centering accuracy within ±0.04 mm

## 3.3 Neutron Scattering

In this section, I will briefly describe the theory behind neutron scattering. At a general level, there are two ways to distinguish the different kinds of neutron scattering used for

studying materials: Inelastic vs. elastic scattering, distinguished by whether or not the neutron changes energy when scattered, and magnetic vs. nuclear scattering, distinguished by whether the scattering is caused by the Zeeman interaction between the sample's magnetic ions and the neutron's magnetic moment, or caused by the strong nuclear forces between the neutrons and the atomic nuclei in the sample. These distinctions create a total of 4 types of scattering. In principle, only the magnetic scattering signals are important for the investigation of magnetism, but they are measured simultaneously and often knowledge of nuclear scattering is crucial for the extraction of magnetic data.

In general terms, elastic scattering, often referred to as *diffraction*, is used to probe order (structural or magnetic), while inelastic scattering, often referred to as *spectroscopy*, is used to probe excitations (structural or magnetic). Regardless of technique, the *scattering vector*, defined as the difference between the initial and final wave vectors of the scattered neutron, $\mathbf{q} = \mathbf{k}_i - \mathbf{k}_f$, is an important quantity. The scattering intensity generally depends on both the direction and magnitude of $\mathbf{q}$, as will be elaborated below, and these quantities are directly obtainable from neutron scattering experiments. Exactly how that is will be described in Section 3.3.3, where I describe the instruments HRPT and FOCUS which were used for the neutron scattering measurements on Ni-LDH.

### 3.3.1 Diffraction

In neutron diffraction, the quantity one measures is the *differential cross section*, $\mathrm{d}\sigma/\mathrm{d}\Omega$, regardless of whether the scattering is magnetic or not. It describes the amount of neutrons, with constant energy, that are scattered into an infinitesimal solid angle $\mathrm{d}\Omega$, normalised to the neutron flux. It is generally given by[20]:

$$\frac{\mathrm{d}\sigma}{\mathrm{d}\Omega} = \left(\frac{m_N}{2\pi\hbar}\right)^2 \left|\langle\psi_i| \hat{V} |\psi_f\rangle\right|^2 \tag{3.3.1}$$

where $\psi_i$ and $\psi_f$ are the initial and final quantum states of the neutrons, $m_n$ is the neutron mass and $\hat{V}$ is the scattering potential. The choice of $\hat{V}$ is what differentiates between nuclear and magnetic scattering, and they are given by[20]:

$$\hat{V}_{nuc} = \frac{2\pi\hbar}{m_N} b_j \delta(\mathbf{r} - \mathbf{r}_j) \tag{3.3.2}$$

$$\hat{V}_{mag} = \frac{\mu_0}{4\pi} g\mu_b\gamma\mu_N \sum_j \hat{\sigma} \cdot \nabla \times \left(\frac{\mathbf{S}_j \times (\mathbf{r} - \mathbf{r}_j)}{|\mathbf{r} - \mathbf{r}_j|^3}\right) \tag{3.3.3}$$

$\hat{V}_{nuc}$ is know as the Fermi pseudo-potential, and $\hat{V}_{mag}$ comes from inserting the field of a dipole, placed at $\mathbf{r}_j$, into the Zeeman Hamiltonian (eq. (2.2.2)) and using the definition of the magnetic moment of a spin (eq. (2.1.1) (right)). $b_j$ is the *scattering length*, an isotope property which describes how much an isotope scatters neutrons. $\hat{\boldsymbol{\sigma}}$ is the Pauli spin matrices, while $\gamma$ and $\mu_N$ are the neutron "$g$-factor" and nuclear magneton respectively.

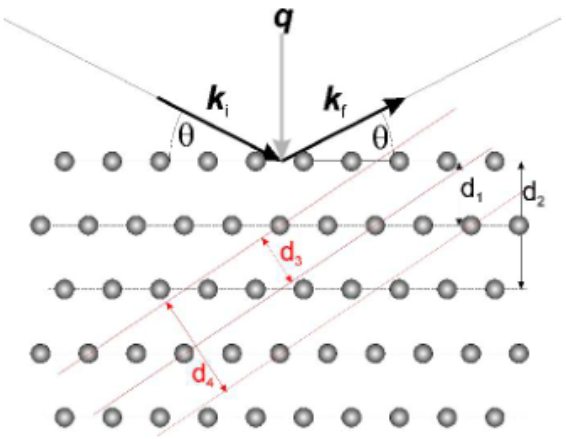


Figure 3.2: Sketch of the symmetry of crystal diffraction. $\mathbf{k}_i$ and $\mathbf{k}_f$ are the incident and outgoing wave vectors respectively, and $\mathbf{q}$ is the scattering vector. $d_n$ is the distance between different lattice planes. In this case, the planes $d_2$ and $d_4$ will not result in Bragg peaks since their nuclear structure factor is zero. Figure adapted from [20].

### Nuclear Diffraction

By inserting $\hat{V}_{nuc}$ (eq. (3.3.2)) into the general differential cross section (eq. (3.3.1)) one ultimately obtains[20]

$$\frac{\mathrm{d}\sigma}{\mathrm{d}\Omega} = N\frac{(2\pi)^3}{V_0}\exp\left(-2W\right)|F_N(\mathbf{q})|^2\sum_{\boldsymbol{\tau}}\delta(\mathbf{q}-\boldsymbol{\tau}) \tag{3.3.4}$$

which is the general nuclear differential cross section for crystalline materials. A lot of new quantities are introduced here. $V_0$ is the volume of the atomic unit cell and $N$ is the number of lattice sites. The factor $\exp\left(-2W\right)$ is known as the *Debye-Waller factor*; it originates from the nuclei vibrating at the lattice equilibrium position. It is often comparable to unity, but always smaller. It becomes smaller for larger $|\mathbf{q}|$, which can be understood as the deviations from equilibrium becoming relatively more important since large $|\mathbf{q}|$ is equivalent to small real-space distances. On the contrary, the Debye-Waller factor becomes larger for lower $T$, since the vibrations have smaller amplitudes at low $T$ and thus interferes less with the scattering. Ultimately, this means that cooling the sample may be necessary when studying phenomena at large $|\mathbf{q}|$[20].

Maybe the most important factor is the *nuclear structure factor*, $F_N(\mathbf{q})$, given by[20]

$$F_N(\mathbf{q}) = \sum_i b_i \exp\left(i\mathbf{q}\cdot\Delta_i\right) \tag{3.3.5}$$

where the sum runs over one unit cell, $\Delta_i$ is the position of the i'th nucleus in the unit cell and $b_i$ is the scattering length of those nuclei. In other words, the nuclear structure factor is what actually contains information about the structure of the sample.

The sum in the end of eq. (3.3.4) tells that scattering only occurs when $\mathbf{q}$ is equal to a reciprocal lattice vector, $\mathbf{q} = \boldsymbol{\tau}$, which is also known as the *Laue condition* [20]. This can be understood in more detail by examining the scattering geometry as displayed in Figure 3.2. The wave vector of the incident and outgoing neutrons both make an angle $\theta$ with the crystal plane in question due to momentum conservation. This totals an angle of $2\theta$ between the incident and diffracted beams, which is referred to as the *scattering angle* and is what is actually measured in experiments. Furthermore, the incident and outgoing wave vectors must have the same magnitude, $|\mathbf{k}_i| = |\mathbf{k}_f| \equiv k$, due to energy conservation in the elastic case. This means that to have constructive interference between scattering from subsequent lattice planes, the wavelength must in some way match to distance $d$ between crystal planes. Per definition one has $|\boldsymbol{\tau}| = \tau = 2n\pi/d$, which together with the Laue condition and the definition of $\mathbf{q}$ gives $|\mathbf{k}_i - \mathbf{k}_f| = 2n\pi/d$. Manipulation of these relations ultimately yields

$$|\mathbf{q}|^2 = |\mathbf{k}_i - \mathbf{k}_f|^2 = |\mathbf{k}_i|^2 + |\mathbf{k}_f|^2 - 2|\mathbf{k}_i||\mathbf{k}_f| \cos 2\theta \tag{3.3.6}$$

$$= 2k^2(1 - \cos 2\theta) = 2^2 k^2 \sin^2 \theta \qquad \Rightarrow \tag{3.3.7}$$

$$q = \frac{4\pi \sin\theta}{\lambda} = \frac{2n\pi}{d} \qquad \Rightarrow \tag{3.3.8}$$

$$n\lambda = 2d \sin\theta \tag{3.3.9}$$

which is known as *Bragg's law*. It relates the observable $\theta$ and the incident wavelength of the neutron, $\lambda$, to the lattice geometry through $d$. It is a reformulation of the Laue condition and thus must be fulfilled for scattering to occur. However, the opposite does not need to be true. Bragg's law sometimes allows scattering from lattice planes with a spacing $d = 2n\pi/q$ corresponding to $q$-values where the nuclear structure factor is zero and no scattering actually occurs [20]. Scattering from conditions fulfilling Bragg's law are normally referred to as *Bragg peaks*.

It is important to note that the nuclear differential cross section (eq. (3.3.4)) does not describe a physical observable - the infinite amplitude of the $\delta$-function is unphysical. However, the integral of such a function can have meaning. Integration over all neutrons scattered from a particular Bragg peak (thus a particular fulfilment of the Laue condition) yields the total cross section of that peak [20]

$$\sigma_{\boldsymbol{\tau}} = N \frac{(2\pi)^3}{V_0} \frac{2}{|\mathbf{k}_i|} \exp(-2W) \, |F_N(\boldsymbol{\tau})|^2 \delta(|\boldsymbol{\tau}|^2 - 2|\mathbf{k}_i||\boldsymbol{\tau}| \cos\omega) \tag{3.3.10}$$

where $\omega$ is a quantity which determines the crystal orientation, defined as the angle between $\mathbf{k}_i$ and the particular $\boldsymbol{\tau}$ corresponding to the Bragg peak in question. This equation still contains a $\delta$-function, thus it needs another integration to become a physical observable, this time either over the crystal orientation $\omega$ or the initial wave vector $\mathbf{k}_i$.

In many cases, one of them being this work, diffraction experiments are performed on powder samples. Powders, which in principle are collections of tiny single crystals, do not

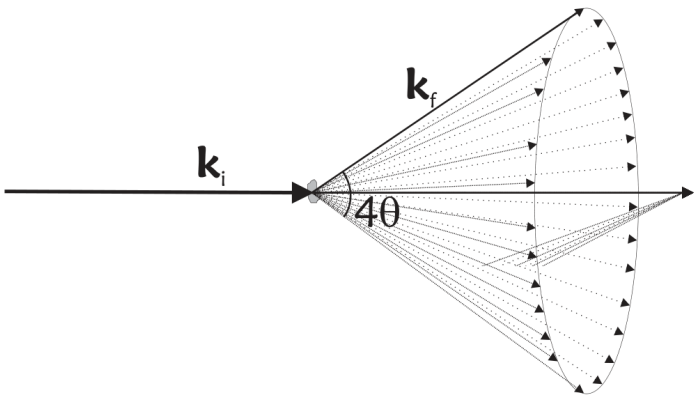


Figure 3.3: A so-called Debye-Scherrer cone, which shows the multitude of scattering of a monochromatic beam happening from a polycrystalline sample. Figure from [20].

have a well-defined crystal orientation. Rather, one can assume that all lattice orientations are equally represented, and Bragg's law is fulfilled in every way possible. This leads to scattering happening in all directions making the same angle with respect to the incoming beam (see Figure 3.3). Thus an integration over $\omega$ (and thereby the crystal orientation) gives the cross section of a Bragg peak with particular $|\boldsymbol{\tau}| = \tau$ observed in a powder diffraction experiment for a given $\mathbf{k}_i$. Such an integration yields[20]

$$\sigma_\tau = N \exp(-2W) \frac{\lambda^3}{4V_0 \sin\theta} j_\tau |F_N(\boldsymbol{\tau})|^2 \tag{3.3.11}$$

where $j_\tau$ is the number of equivalent lattice planes that contribute to the scattering. However, the integration removes information about the direction of $\boldsymbol{\tau}$, thus contributions from different $\boldsymbol{\tau}$'s with the same magnitude cannot be distinguished. This is important, since non-equivalent lattice planes may have the same $\tau$, as is e.g. the case for the (221) and (300) lattice planes of the cubic lattice[20]. Therefore, the result of the integration needs to be summed over all $\boldsymbol{\tau}$ with the same magnitude, resulting in $\sigma_q = \sum_{\tau=q} \sigma_\tau$, which is the actual observable.

In a way, this means that the Bragg peaks one finds from a powder diffraction experiment are different from those found in a single-crystal experiment. In the powder case, a Bragg peak collects all scattering with a particular $q$ regardless of origin, and there is no direct way to distinguish individual contributions. Also, it is worth noticing that the cross section of a particular Bragg peak is proportional $\lambda^3$, which means that one is severely punished for using low-wavelength neutrons. However, using long-wavelength neutrons puts an upper boundary on the available $q$-range since eq. (3.3.8) leads to $q_{max} = 4\pi/\lambda$.

### Magnetic Diffraction

Magnetic diffraction is in many ways analogous to the nuclear case. The few differences are the choice of scattering potential (see eqs. (3.3.2) and (3.3.3)), and that the magnetic

unit cell might be different from the atomic unit cell, which is eq. the case for the 2D AFM lattice displayed in Figure 2.1 (middle), for which the magnetic unit cell is twice the size of the atomic in both directions[20]. Inserting $\hat{V}_{mag}$ into eq. (3.3.1), while assuming that the incident neutrons are unpolarized, will after some manipulation yield[20]

$$\frac{\mathrm{d}\sigma}{\mathrm{d}\Omega} = (\gamma r_0)^2 \left[\frac{g}{2}F(q)\right] \exp\left(-2W\right) \sum_{\alpha,\beta} \left(\delta_{\alpha\beta} - \hat{q}_\alpha \hat{q}_\beta\right) \sum_{j,j'} \exp\left(i\mathbf{q}\cdot\left(\mathbf{r}_{j'} - \mathbf{r}_j\right)\right) \left\langle S_j^\alpha S_{j'}^\beta \right\rangle \tag{3.3.12}$$

Again, a lot of new quantities are introduced. The classical electron radius, $r_0 = 2.82$ fm, is introduced as a prefactor. $F(q)$ is the *magnetic form factor*, which varies smoothly from unity at $q = 0$ and goes to zero with increasing $q$. It is defined as[20]

$$F(\mathbf{q}) = \int \exp(i\mathbf{q}\cdot\mathbf{r}) s(\mathbf{r}) d^3\mathbf{r} \tag{3.3.13}$$

where $\mathbf{r}$ is a small displacement of the electron coordinate from the lattice position $\mathbf{r}_j$, which comes from the electrons not being located at exactly the nuclear position but in the electronic orbitals.

The first sum, where $\alpha$ and $\beta$ runs over the cartesian coordinates, makes sure that only the part of the spins perpendicular to the scattering vector contributes to the cross section. This is a defining concept for magnetic scattering which directly pops out when calculating the magnetic matrix element, $\langle\psi_f|\,\hat{V}_{mag}\,|\psi_i\rangle$. The factor $\langle S_j^\alpha S_{j'}^\beta\rangle$ is the spatial correlation function between the coordinate $\alpha$ of spin $j$ and the coordinate $\beta$ og spin $j'$. In essence, eq. (3.3.12) is the space Fourier transform of this correlation function.

If one assumes that scattering happens from an ordered magnetic structure, the magnetic differential cross section becomes

$$\frac{\mathrm{d}\sigma}{\mathrm{d}\Omega} = (\gamma r_0)^2 \left[\frac{g}{2}F(q)\right] \exp\left(-2W\right) N \frac{(2\pi)^3}{V_{0,mag}} |F_M(\mathbf{q})|^2 \sum_{\boldsymbol{\tau}} \delta(\mathbf{q} - \boldsymbol{\tau} - \mathbf{Q}) \tag{3.3.14}$$

where $\mathbf{Q}$ is the magnetic ordering vector as introduced in Section 2.3. The above equation is analogous to eq. (3.3.4) for nuclear diffraction. Here, $F_M(\mathbf{q})$ is the *magnetic structure factor*, which is defined as

$$F_M(\mathbf{q}) = \sum_i \exp(-i\mathbf{q}\cdot\Delta_i) \left\langle \mathbf{S}_{i,\perp} \right\rangle \tag{3.3.15}$$

where the sum runs over one magnetic unit cell analogous to eq. (3.3.5). $\langle \mathbf{S}_{i,\perp} \rangle$ is the thermal average of the part of the i'th spin perpendicular to $\mathbf{q}$. In fact, eq. 3.3.14 becomes eq. 3.3.4 with the substitution

$$b_j \rightarrow \gamma r_0 \frac{g}{2} F(q) \mathbf{S}_{i,\perp} \tag{3.3.16}$$

why the right-hand side is denoted the *magnetic scattering length*, which in most cases is of the same order of magnitude as $b_j$.

The only qualitative difference between eq. 3.3.4 and eq. 3.3.14 is the presence of the magnetic ordering vector $\mathbf{Q}$ (see Section 2.3) in the $\delta$-function. It is introduced because summing over the magnetic unit cell may allow for more $\boldsymbol{\tau}$'s than summing over the nuclear unit cell, since the magnetic cell can differ in size. The essence of this is that the $\delta$-function allows magnetic Bragg peaks when $\mathbf{q} = \mathbf{Q}$, give or take a reciprocal lattice vector, which means that one can directly measure $\mathbf{Q}$ in a diffraction experiment.

However, scattering does not solely come from magnetic order. From eq. (3.3.12), one has that the cross section depends on the spin-spin correlation function. A system does not need to be ordered for correlations to exist, thus one can have diffraction signals from disordered, but correlated, magnetic systems. This kind of scattering is known as *critical scattering* and appears at the same $\mathbf{q}$-values as the magnetic Bragg scattering but is less intense and has a Lorentzian line shape[66]. Such a line shape corresponds to exponentially decaying correlations since the Fourier transform of an exponential gives a Lorentzian, which is also why the line width is directly related to the correlation length.

### 3.3.2 Spectroscopy

In neutron spectroscopy, the quantity in question is the *partial differential cross section*, $\mathrm{d}^2\sigma/\mathrm{d}\Omega\mathrm{d}E_f$. Compared to the differential cross section, it now deals with neutrons with a final energy in the infinitesimal range $[E_f; E_f + \mathrm{d}E_f]$ scattered into the infinitesimal solid angle $\mathrm{d}\Omega$. It is in general given by[20]

$$\frac{\mathrm{d}^2\sigma}{\mathrm{d}\Omega\mathrm{d}E_f} = \frac{k_f}{k_i}\left(\frac{m_n}{2\pi\hbar}\right)^2 \left|\langle\lambda_i\psi_i|\,\hat{V}\,|\psi_f\lambda_f\rangle\right|^2 \delta(E_i - E_f + \hbar\omega) \tag{3.3.17}$$

where $\lambda_i$ and $\lambda_f$ are the initial and final sample states, $k_i$ and $k_f$ are the wave numbers of the incoming and outgoing neutrons respectively, and the other quantities are the same as those given in eq. (3.3.1). The main difference is the $\delta$-function, which states that the energy change of the sample, $\hbar\omega = \Delta E$, is equal to the energy difference of the scattered neutron, $E_i - E_f$. Note the unconventional choice of sign: Neutron energy loss is defined to yield $\hbar\omega > 0$. As for diffraction, the choice of scattering potential determines what kind of spectroscopy the equation describes.

Eventually, inserting $\hat{V}_{mag}$ (eq. (3.3.3)) into eq. (3.3.17) and assuming that scattering happens from a lattice with unpolarised neutronsonly will yield

$$\begin{aligned}\frac{\mathrm{d}^2\sigma}{\mathrm{d}\Omega\mathrm{d}E_f} = &(\gamma r_0)^2 \frac{k_f}{k_i}\left[\frac{g}{2}F(q)\right]^2 \exp(-2W)\sum_{\alpha,\beta}(\delta_{\alpha\beta} - \hat{q}_\alpha\hat{q}_\beta) \\ &\frac{N}{2\pi\hbar}\int_{-\infty}^{\infty}\sum_{j'}\exp(i\mathbf{q}\cdot\mathbf{r}_{j'})\,\langle S_0^\alpha(0)S_{j'}^\beta(t)\rangle\exp(i\omega t)\mathrm{d}t\end{aligned} \tag{3.3.18}$$

where $\langle S_0^\alpha(0)S_{j'}^\beta(t)\rangle$ is the spin pair correlation function and the other factors are the same as given in eq. (3.3.12). The spin pair correlation function should be interpreted as the

correlation between component $\alpha$ of $\mathbf{S}_0$ at a fixed point in time and component $\beta$ of $\mathbf{S}_{j'}$ as time goes by, and the above equation is essentially the space and time Fourier transform of that function. Again, the factor $\sum_{\alpha,\beta}(\delta_{\alpha\beta} - \hat{q}_\alpha \hat{q}_\beta)$ is present, which secures that only the spin parts perpendicular to the scattering vector contributes to the cross section, as is always the case for magnetic scattering.

The above frameworks shows that calculating $\langle S_0^\alpha(0) S_{j'}^\beta(t)\rangle$ can give an expression for $\mathrm{d}^2\sigma/\mathrm{d}\Omega\mathrm{d}E_f$. That can be a daunting task, but making some assumptions about the dynamics of the scattering system can greatly simplify it. A common approach is to assume that the system is in an ordered magnetic state and that it's excitations are well described by spin wave theory (see Section 2.5).

In Section 2.5, I showed that $\langle S^z\rangle$ is a constant of motion in SWT. In order to not change $\langle S^z\rangle$, one must keep the quantum number $m_s$ constant and therefore only consider terms with an equal amount of $S^+$ and $S^-$ operators, why only $\langle S_j^+(0) S_{j'}^-(t)\rangle$ $\langle S_j^-(0) S_{j'}^+(t)\rangle$ and $\langle S_j^z(0) S_{j'}^z(t)\rangle$ can contribute to the cross section. The $zz$-term has no time dependence, since $\langle S_z\rangle$ is a constant of motion in SWT, thus it only contributes to elastic scattering. The $-+$-term is by definition given by

$$\langle S_j^-(0) S_{j'}^+(t)\rangle = \left\langle \frac{1}{\sqrt{N}} \sum_{\mathbf{q}'} \exp\left[-i\mathbf{q}\cdot\mathbf{r}_j\right] S_{\mathbf{q}'}^- \frac{1}{\sqrt{N}} \sum_{\mathbf{q}'} \exp\left[i\mathbf{q}'\cdot\mathbf{r}_{j'}\right] S_{\mathbf{q}'}^+ \exp[-i\omega_{\mathbf{q}'}t] \right\rangle \tag{3.3.19}$$

$$= \frac{1}{N} \sum_{\mathbf{q}'} \exp\left[-i\mathbf{q}'\cdot(\mathbf{r}_j - \mathbf{r}_{j'})\right] \exp\left[-i\omega_{\mathbf{q}'}t\right] \langle S_{\mathbf{q}'}^- S_{\mathbf{q}'}^+\rangle \tag{3.3.20}$$

As described in Section 2.5, $S_{\mathbf{q}'}^-$ and $S_{\mathbf{q}'}^+$ are the creation and annihilation operators of magnons in a ferromagnet, thus $S_{\mathbf{q}'}^- S_{\mathbf{q}'}^+$ is related to the number operator. The thermal average of it's eigenvalue is given by $2\langle S^z\rangle n_B(\hbar\omega_{\mathbf{q}'}/k_BT)$, where $n_B$ is the Bose factor[67]

$$n_B\left(\frac{\hbar\omega_{\mathbf{q}'}}{k_BT}\right) = \left(\exp\left(\frac{\hbar\omega}{k_BT}\right) - 1\right)^{-1} \tag{3.3.21}$$

With this the above pair correlation reduces to

$$\langle S_j^-(0) S_{j'}^+(t)\rangle = \frac{2\langle S^z\rangle}{N} \sum_{\mathbf{q}'} \exp\left[-i\mathbf{q}'\cdot(\mathbf{r}_j - \mathbf{r}_{j'})\right] \exp\left[-i\omega_{\mathbf{q}'}t\right] n_B\left(\frac{\hbar\omega_{\mathbf{q}'}}{k_BT}\right) \tag{3.3.22}$$

$\langle S_j^+(0) S_{j'}^-(t)\rangle$ can be found from this equation by utilising that $[S_j^-, S_{j'}^+] = 2S^z$, yielding

$$\langle S_j^+(0) S_{j'}^-(t)\rangle = \frac{2\langle S^z\rangle}{N} \sum_{\mathbf{q}'} \exp\left[-i\mathbf{q}'\cdot(\mathbf{r}_j - \mathbf{r}_{j'})\right] \exp\left[-i\omega_{\mathbf{q}'}t\right] \left(n_B\left(\frac{\hbar\omega_{\mathbf{q}'}}{k_BT}\right) + 1\right) \tag{3.3.23}$$

Now, recognizing that the $x$- and $y$-axes are equivalent one realises that $\langle S_j^x(0) S_{j'}^x(t)\rangle = \langle S_j^y(0) S_{j'}^y(t)\rangle$. From there, one can use the definition of the $S^\pm$-operators to obtain an

expression for $\langle S_j^x(0)S_{j'}^x(t)\rangle$ as

$$\langle S_j^-(0)S_{j'}^+(t)\rangle = \left\langle S_j^x(0)S_{j'}^x(t) + iS_j^x(0)S_{j'}^y(t) - iS_j^y(0)S_{j'}^x(t) + S_j^y(0)S_{j'}^y(t)\right\rangle \tag{3.3.24}$$

$$\langle S_j^-(0)S_{j'}^+(t)\rangle = \left\langle S_j^x(0)S_{j'}^x(t) - iS_j^x(0)S_{j'}^y(t) + iS_j^y(0)S_{j'}^x(t) + S_j^y(0)S_{j'}^y(t)\right\rangle \tag{3.3.25}$$

$$\Downarrow$$

$$\langle S_j^x(0)S_{j'}^x(t)\rangle = \frac{1}{4}\left\langle S_j^-(0)S_{j'}^+(t) + S_j^+(0)S_{j'}^-(t)\right\rangle \tag{3.3.26}$$

Inserting the above into eq. (3.3.18) yields the partial differential cross section for ferromagnetic spin waves[20]

$$\begin{aligned}\frac{\mathrm{d}^2\sigma}{\mathrm{d}\Omega\mathrm{d}E_f} = (\gamma r_0)^2\frac{k_f}{k_i}\left[\frac{g}{2}F(q)\right]^2\exp(-2W)(1+\hat{q}_z^2)\frac{\langle S_z\rangle}{2} \\ \frac{(2\pi)^3}{V_{0,mag}}\sum_{\mathbf{q},\boldsymbol{\tau}}\Bigg[\left(n_B\left(\frac{\hbar\omega_{\mathbf{q}'}}{k_BT}\right)+1\right)\delta(\hbar\omega_{\mathbf{q}'}-\hbar\omega)\delta(\mathbf{q}'-\mathbf{q}-\boldsymbol{\tau}) \\ n_B\left(\frac{\hbar\omega_{\mathbf{q}'}}{k_BT}\right)\delta(\hbar\omega_{\mathbf{q}'}+\hbar\omega)\delta(\mathbf{q}'+\mathbf{q}-\boldsymbol{\tau})\Bigg]\end{aligned} \tag{3.3.27}$$

where the $\hbar\omega$ $\delta$-functions come from the integral of the time-dependent exponentials in eq. (3.3.22) and the $\mathbf{q}$ $\delta$-functions comes from the $j'$ sum of the $(\mathbf{r}_j - \mathbf{r}_{j'})$-exponentials in the same equation ($\boldsymbol{\tau}$ is added to the $\delta$-function since $\boldsymbol{\tau}\cdot\mathbf{r}_j = 2n\pi$). Since only the $xx$- and $yy$-correlations ended up contributing, the perpendicular factor becomes $(1-\hat{q}_x^2)+(1-\hat{q}_y^2) = 1+\hat{q_x^2}$.

The main result here is hidden in the $\hbar\omega$ $\delta$-functions. They secure that the energy change of the neutrons, $\hbar\omega$, is equal to the energy of the related magnons, $\hbar\omega_{\mathbf{q}'}$. Remember that the sign convention makes $\hbar\omega > 0$ for neutron energy loss, thus a positive value of $\hbar\omega$ corresponds to creating a magnon. Also, the $\mathbf{q}$ $\delta$-functions secure that the scattering vector and the magnon wave vector are equal, give or take a reciprocal lattice vector. Thus, FM SW excitations are directly measurable in a neutron spectroscopy experiment. For AFMs the calculations are more cumbersome, but the main results are still true[20].

Like discussed in the diffraction section, magnetic order is not a necessity for scattering to occur - correlations can still exist in the disordered phase, which is also true for time-dependent correlations. A prime example of this is the $S = 1/2$ AFM QSC. Scattering data measured above the transition to long range order was showed in Figure 2.8 and from that it is immediately clear that rich dynamics are still present. In fact, the lower boundary of the continuum is given by the spin wave dispersion renormalised by $\pi/2$[12].

### 3.3.3 HRPT - Powder Diffractometer

HRPT is a high-resolution powder diffractometer for thermal neutrons (hence the name) at the Swiss neutron facility SINQ at the Paul Scherrer Institute; it's geometry can be seen in Figure 3.4[68]. When the neutrons enter the instrument, they first pass through

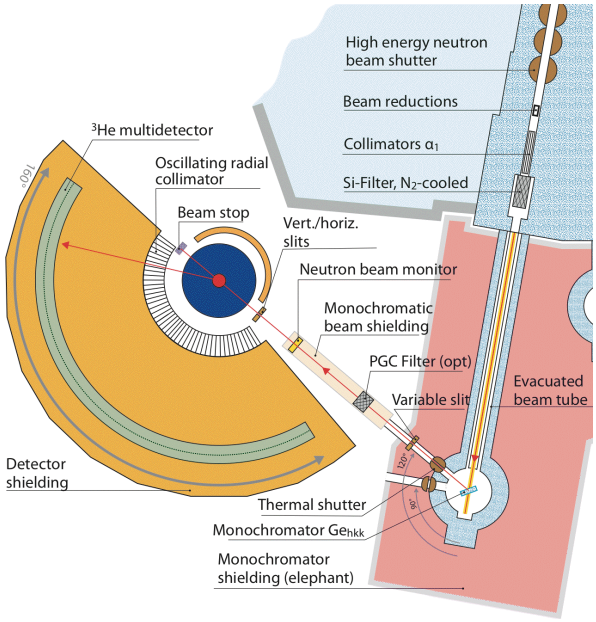


Figure 3.4: Schematic of the powder neutron diffractometer HRPT at SINQ, PSI. The neutron beam enters from the top. Figure adapted from [68]

an optional Gd-O Soller collimator, which is the primary collimator and can set the maximum beam divergence to 6′, 12′ or 24′. Any of these choices are referred to as HRPT's high-resolution mode. If no collimator is used, the beam passes through an opening which effectively sets the divergence maximum to $\sim 40'$; this is referred to as it's high-intensity mode. Thereafter, the neutrons pass through a Si-filter, which removes neutrons with very high energy. Their low wavelength would make them ignore the Bragg condition since the wavelength is small enough that they would scatter as particles and therefore scatter from each nucleus, why they would not be discarded by the wafer-type Ge-monochromator placed after the Si-filter. After the monochromator, the neutrons pass through a secondary slit system before reaching the sample position. An optional pyrolytic graphite (PG) filter can be placed between the slits and the sample to remove higher order scattering from the monochromator, but it was not used for our experiment.

After hitting the sample, a radial collimator suppresses scattering from the sample environment by only letting neutrons scattered in directions radially out from the sample hit the detector. The collimator oscillates to not prevent neutrons from hitting the part of the detector right behind the collimator walls. The detector is a large multi-detector with 1600 measurement wires, each separated by an angle of 0.1°. These wires vary in efficiency by ±10 %, which needs to be taken into account when normalising data. The detector can measure $2\theta$ in a 160° range, and the angular step can be as small as 0.05° since the detector is placed on air cushions and can be continuously displaced.

There is no device which secures that $k_i = k_f$, thus HRPT actually measures the energy integrated partial differential cross section, and the available energy scale is that of the

incoming neutrons. For nuclear signals, it is not important since the elastic part is anyway dominant compared to the inelastics. However, if the neutron energy is comparable to the energy scale of the magnetic interactions it can have an effect on the measurements. The energy integration happens in the detector wires, thus along constant $2\theta$ and not along straight lines in $q$. Therefore, eventual features from the energy integration will have an asymmetrical line shape. For HRPT however, $E_N \sim 25\,\text{meV} \sim 290\,\text{K}$, while the magnetic interactions are in our LDHS are of the order 1 K (as will be shown in Results), why any eventual magnetic signals can be treated as properly energy integrated in our case.

### 3.3.4 FOCUS - TOF Spectrometer

FOCUS is a direct geometry (DG) time-of-flight (TOF) neutron spectrometer at the Swiss neutron facility SINQ located at the Paul Scherrer Institute. In broad terms, it works by letting monochromatic neutrons, selected by a pair of choppers, scatter from a sample whereafter it measures the flight time, $\tau_f$, to the detector and the scattering angle, $2\theta$. From these, one can obtain the final energy $E_f$ and the magnitude of $q$ as[69]

$$E_f = \frac{\hbar^2 k_f^2}{2m_n}, \qquad k_f = \frac{m_n L_2}{\hbar \tau_f} \tag{3.3.28}$$

$$\frac{\hbar^2 q^2}{2m_n} = E_i + \frac{\hbar m_n L_2^2}{2\tau_f} - L_2 cos(2\theta)\sqrt{E_i \frac{\hbar m_n}{2\tau_f}} \tag{3.3.29}$$

where $L_2$ is the (known) distance from the sample to the detector.

The exact geometry of FOCUS is shown in Figure 3.5[70]. When the neutrons enter the instrument, a disk chopper creates the initial neutron pulses. It's rotation speed is synchronised with the Fermi chopper, which secures that only neutrons in a narrow energy band can hit the sample. After the disk chopper, a Be-filter is used to suppress contamination from neutrons with $\lambda_i < 4$ Å. Then the neutrons are focused on the Fermi chopper with a monochromator, which also removes any neutrons taking an undesired path through the choppers. The neutrons are then scattered from the sample and passes through a collimator to minimize divergence. At last they pass a well-known distance through an Ar-filled flight box before being detected in one of 375 rectangular shaped $^3$He counter tubes[70]. Then, energy and momentum changes can be determined from the equations above since $L_2$ and $E_i$ are know and $\tau_f$ and $2\theta$ are measured.

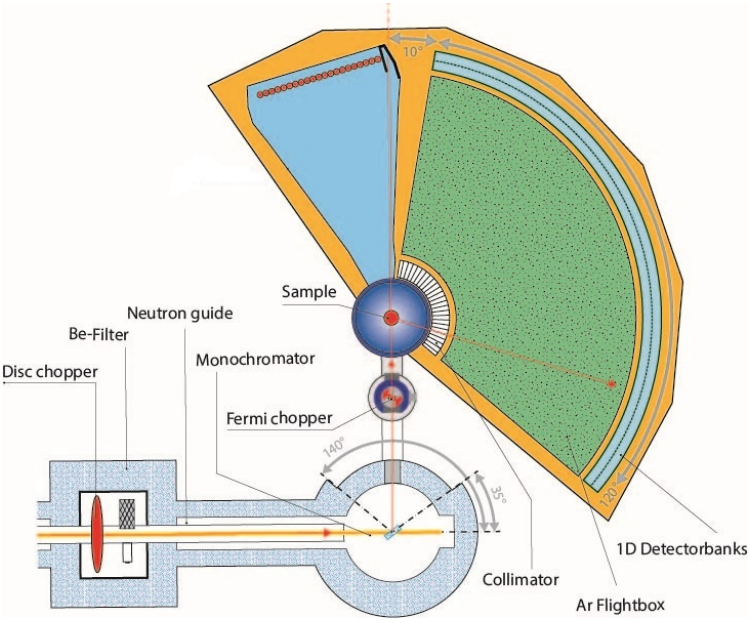


Figure 3.5: Schematic of the TOF neutron spectrometer FOCUS at SINQ, PSI. The neutron beam enters from the left Figure adapted from [70].

# Chapter 4

# Results

In this section, I will present the results I have collected on each type of LDH (Cu, Ni and Co). For all three samples, I have analysed heat capacity (vs. temperature) and measured and analysed magnetisation (vs. temperature and applied field). I also analysed neutron powder diffraction and spectroscopy data measured on Ni-LDH and partook in the remote experiments, since doing them in-person was impossible to the covid-19 pandemic. For details on the experimental methods, see Section 3. I will present the different types of data one by one, each time presenting general experimental methodology before presenting the results on each compound individually.

## 4.1 Magnetisation

All measurements presented here were measured on mg-sized M(II)-LDH powder samples (M(II)=$Cu^{2+}$, $Ni^{2+}$, $Co^{2+}$, described in Section 3.1) synthesised by Anders Bruhn Arndahl Andersen at Univ. of Southern Denmark. The measurements were performed at the Technical University of Denmark with the assistance of Ass. Prof. Kasper Steen Pedersen using a Quantum Design Dynacool™ PPMS®, equipped with a vibrating sample magnetometer, with the powder in a polypropylene sample holder. Details about the setup can be found in Section 3.2.

For all samples, we measured magnetization ($M$) as a function of both applied field ($H$) and temperature ($T$). When measuring $M(H)$, the samples were zero-field cooled to the desired temperature before tuning the field. We measured in the $H$-range $-9 - 9$ T at temperatures $T = 2\,\mathrm{K}$ and $T = 50\,\mathrm{K}$ (for Ni- and Co-LDH, only from 0 to 9 T in the 50 K case). The measurements are shown in Figure 4.1. No signs of hysteresis were found in any sample, except for a tiny recurring effect ($\sim$ 10 mT) which I assume originates from the magnets in the setup.

For all measurements of $M(T)$, we zero-field cooled the sample rapidly to 10 K and afterwards cooled it slowly to 1.9 K. The applied field was then set to desired value (0.01

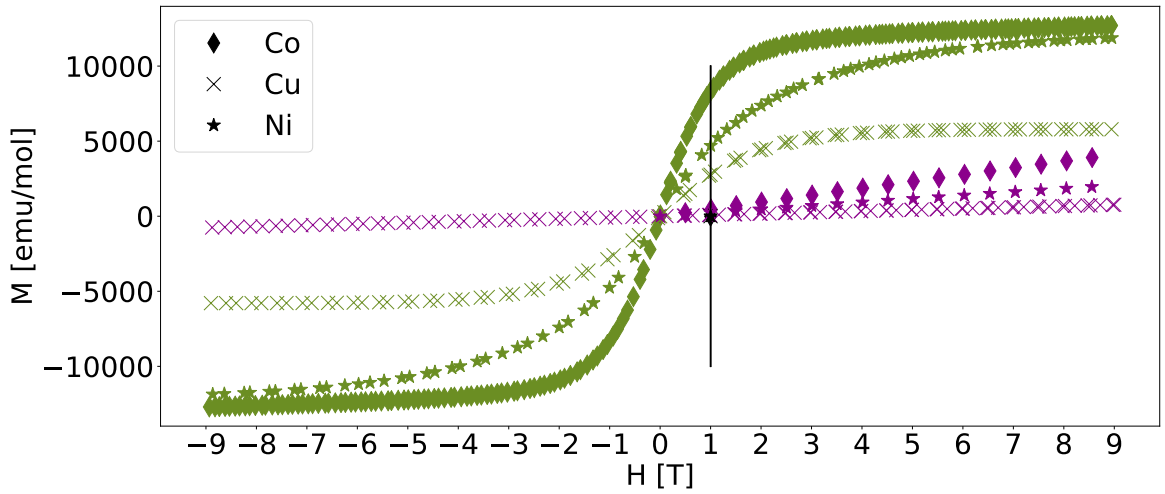


Figure 4.1: $M$ vs. $H$ for Cu-LDH (×'s), Ni-LDH (stars) and Co-LDH (diamonds) at $T = 2\,\mathrm{K}$ (green) and $T = 50\,\mathrm{K}$ (magenta). The black vertical line is situated at $H = 1\,\mathrm{T}$ and is added to guide the eye. For clarity only every 100th data point is shown.

T, 0.1 T or 1 T), and the sample was heated at 1 K/min. These measurements were used to calculate the susceptibility under the assumption that our samples are linear media obeying the equation

$$\chi_{meas} = \frac{M}{H} = \chi_{sample} + \chi_0 \tag{4.1.1}$$

where $\chi_{meas}$ is the measured (raw) susceptibility data, $\chi_{sample}$ is the true susceptibility of the sample and $\chi_0$ is a temperature-independent term designed to account for constant susceptibility contributions, e.g. from the setup or from van Vleck paramagnetism [17].

A field strength of $H = 1$ T, marked by a vertical black line on Figure 4.1, is clearly right at the edge of the linear regime for all samples at $T = 2$ K. For that reason, I only consider measurements of M(T) performed at $H \leq 1$ T, even though we also measured $M(T)$ at higher fields. I determine $\chi_0$ by fitting the appropriate model (see Section 2.4.3) to data by minimizing the $\chi^2$. Before fitting I subtracted the samples' temperature-independent intrinsic diamagnetic susceptibilities from $\chi_{meas}$. They originate from their non-magnetic parts and are tabulated [71], why they are easy to subtract.

### 4.1.1 Ni-LDH

The raw susceptibility of Ni-LDH, measured at 0.01 T (orange), 0.1 T (green) and 1 T (blue) is shown in Figure 4.2. Immediately, it is clear that data measured at $H = 0.01$ T has a significantly worse signal-to-noise ratio. Also, the $H = 0.01$ T inverse susceptibility is about 50 % larger at high $T$ compared data measured at larger applied fields, which means $\chi_0$ must be smaller when $H = 0.01$ T, since the signal should not depend on the

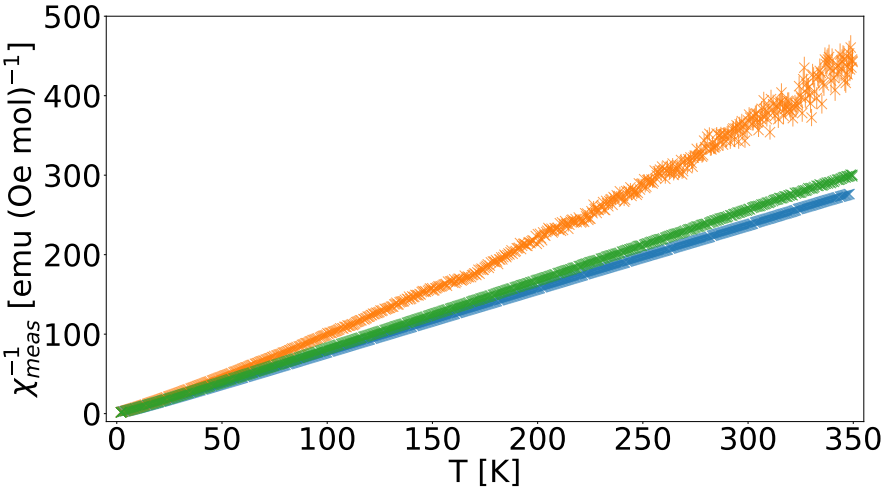


Figure 4.2: $\chi^{-1}_{meas}(T)$ for Ni-LDH at $H = 0.01$ T (orange), $H = 0.1$ T (green) and $H = 1$ T (blue). Only every 10th data point is shown for clarity. For data measured at $H \geq 0.1$ T, errorbars are generally smaller than the markers.

strength of the applied field as long as we are inside the linear regime. Then again, $\chi_0$ is difficult to estimate correctly due to the bad S/N-ratio, why I focus on the 0.1 and 1 T data only. For both of these, the raw data reveals no signs at all down of a transition to long range magnetic order down to $T = 2$ K, as no discontinuities or dents, like that shown on Figure 2.2, are seen in the data.

The $H = 1$ T data is shown in Figure 4.3a, plotted as both $\chi^{-1}(T)$ and $\chi(T)T$. I unorthodoxly chose to also plot $\chi T$ since it reveals features hidden when plotting $\chi^{-1}$, exemplified by the broad peak in $\chi T$ at $T \approx 8$ K. From the $M(H)$-data shown in the beginning of this section, it is clear that parts of this data set is not within the linear regime at $T = 2$ K, thus $\chi \approx M/H$ is not applicable for all data. To determine the lowest useful temperature, I use the crude approximation $M \approx B/T$ (ignoring units). This way, I can use the largest measured value of $M$ inside the linear regime to estimate the lowest useful $T$. I observe that for measurements at $T = 50$ K, $M(H)$ is always inside the linear regime and the largest measured $M$-value is $M(9\,\mathrm{T}) \approx 2000$ emu/(mol Oe), meaning $T \approx B/M = 10^4\,\mathrm{Oe}/2000\,\mathrm{emu/(mol\ Oe)} \approx 5$ K is the lowest temperature for which $M(T)$ can be used to determine $\chi$ for the 1 T data.

I fitted both the CW (eq. (2.4.18)) and non-critical scaling models (eq. (2.4.27)) to the 1 T data. For the scaling model, I included an AFM interchain interaction to account for the local maximum in $\chi T$ at $T \approx 8$ K, assuming that each chain only interacts with it's two nearest neighbours within a layer. The scaling model easily fit the data in the whole temperature range (5 K to 350 K) and yielded $J = 3.84(14)$ K and $j = -1.02(2)$ K with $g = 2.250^{+0.004}_{-0.005}$ assuming $S = 1$. The fit is shown as a black line on Figure 4.3a. The errors on the parameters are estimated by observing their change induced by altering $\chi_0$ by $\pm 33$ %. I chose to estimate the errors in this manner since the statistical errors from

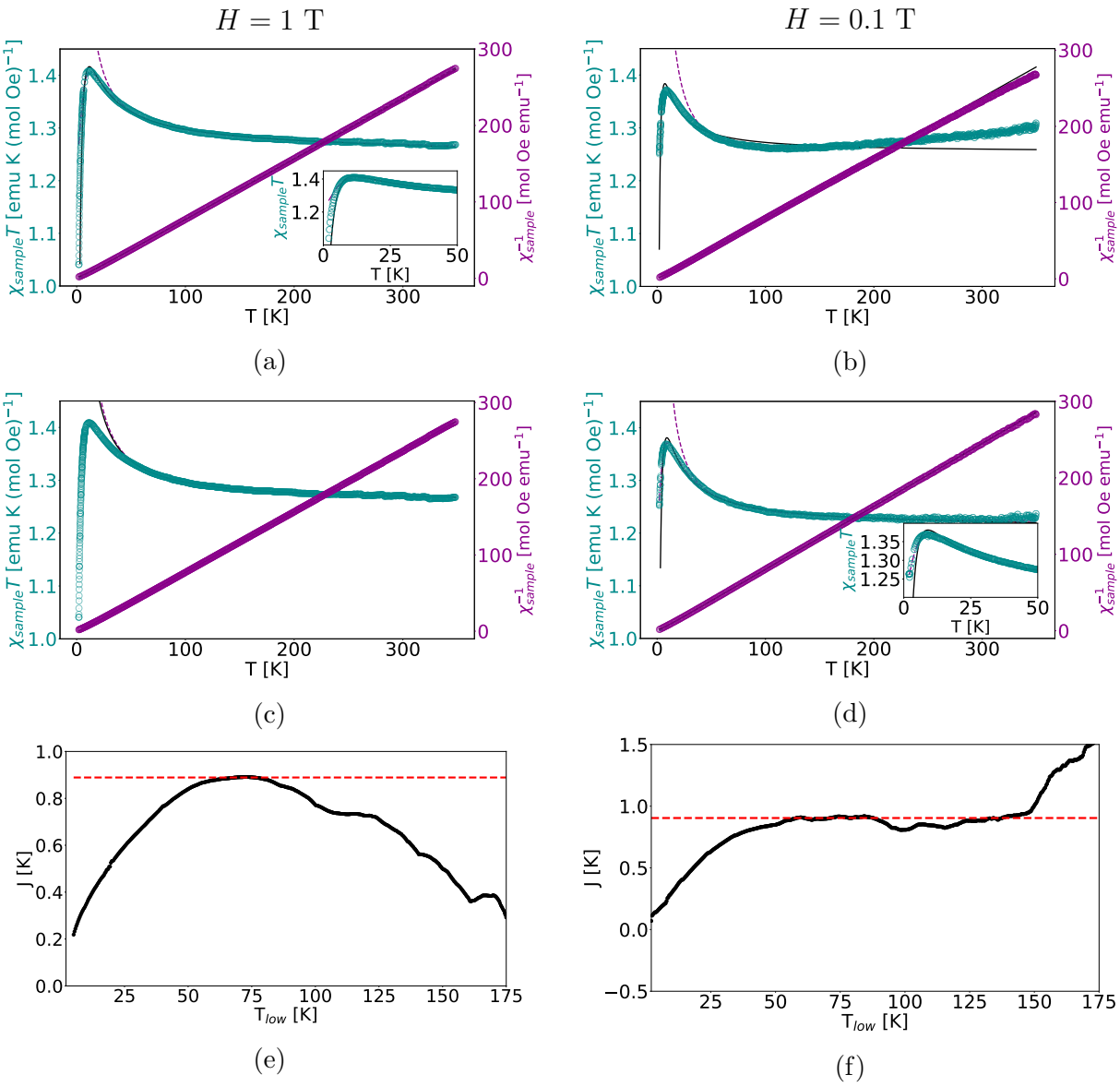


Figure 4.3: Susceptibility data for Ni-LDH measured at $H = 1$ T (left column) and $H = 0.1$ T (right column). On graphs (a)-(d), only every 10th data point is shown for clarity, and errorbars are smaller than the markers. $\chi T$-data is cyan and uses the left y-axis; $\chi^{-1}$-data is magenta and uses the right y-axis. CW-fits are magenta and dashed, non-critical scaling fits are full, black lines and ZFS-fits are magenta and dash-dotted. All fits are best viewed on the electronic document. Fit parameters are given in the text. The dashed lines on graphs (e) and (f) show the estimated $J$-value. **(a)**: Susceptibility data with fits. The inset is zoom on the low-$T$ region. **(b)**: Susceptibility data with wrongly estimated background. **(c)**: Susceptibility data with CW and scaling fits fitted to high-$T$ data ($T = 73$ K - 350 K). **(d)**: Susceptibility data with properly estimated background. The uncertainties are scaled by $c/\sqrt{T}$ for the scaling fit. The inset is zoomed on the low-$T$ region. **(e)**: $J$ from CW-fit vs. lower cut-off $T_{low}$. A plateau is found in the range $T = 67$ K - 79 K. **(f)**: $J$ from CW-fit vs. lower cut-off $T_{low}$. A plateau is found in the range $T = 54$ K - 88 K.

the fit estimated the error to be on the fifth significant figure; a level of accuracy much too large. I chose to vary exactly $\chi_0$ since the measured signal is weak, thus correctly determining $\chi_0$ is important to correctly determine $J$ and $j$. I chose $\pm 33$ % since it was the largest change where I visually assessed the fits qualitatively similar.

I had more difficulties fitting the CW-model. It is clear that the behaviour at the lowest $T$ is not CW-like. If so, one would expect the trend of $\chi T$ (with background contributions subtracted) to be constant and not have a broad peak like at $T \approx 8$ K (see Figure 4.3a). Thus, I need to determine a lower boundary, $T_{low}$, for the fit in order to only fit the region that actually behaves in a CW-like manner. Only fitting the high-$T$ regime is further motivated by the fact that I used a high-$T$ expansion of the Brillouin function when deriving the CW law. I never put an upper limit on the fitting range, as small changes in the upper limit had no effect on the parameters, and large changes clearly made the fits worse. Also, I have no reason for data at high $T$ not being useful.

The goal for the chosen $T_{low}$ is that my choice has as little influence as possible on the obtained parameter. To find the best choice, I performed CW fits with different values of $T_{low}$, plotted $J$ vs. $T_{low}$ (see Figure 4.3e) and looked for a region(s) where $J(T_{low})$ was flat, which meant that changing $T_{low}$ would not impact $J$ significantly. I found a plateau in the range 67 K - 79 K. To further distance my choice of $T_{low}$ from the final parameter, I computed the arithmetic mean of $J(T_{low})$'s with integer values (in K) of $T_{low}$ inside the plateau instead of choosing an arbitrary $T_{low}$ within the plateau. This approach yielded $J = 1.12(2)$ K with $g = 2.24311(9)$ assuming $S = 1$, which corresponds to $\theta_{CW} = 2.981(6)$ K. The error is the uncertainty on the arithmetic mean. The CW model with these parameters is shown as a dashed line on Figure 4.3a.

The above CW result is significantly different from the scaling approach, which is to be expected, since the CW-approach does not consider the low-T behaviour nor the interchain interaction. To compare the two models, I fitted the scaling model in the same high-T regime as the CW-fit (73 K - 350 K) and obtained $J = 3.36^{+0.06}_{-0.08}$ K, where the errors again are estimated by altering $\chi_0$ by $\pm 33$ %. Since the feature caused by the interchain interaction lie outside this $T$-regime, I locked $j$ to the previous value before fitting. The resulting fit is shown in Figure 4.3c (black line) together with the CW-fit, which shows that the two models behave similarly despite yielding different parameters.

Consider now the data measured at $H = 0.1$ T (Figure 4.3b). This time, all data down to 2 K could be used since $T \approx B/M = 10^3\,\mathrm{Oe}/2000\,\mathrm{emu/(mol\ Oe)} \approx 0.5$ K. It is clear that the scaling approach did not fit easily contrary to the 1 T case; the model does not follow data at high $T$. At high $T$, the sample should be firmly in the paramagnetic state and therefore behave in a completely CW-like manner, meaning that $\chi T$ should not have no slope at the highest $T$, which is not the case for the data in Figure 4.3b.

By manually lowering $\chi_0$ to about 35 % of the fitted value, I made the fit behave in the expected manner, which told that correct determination of $\chi_0$ might be the issue. Such

behaviour can be explained by the fact that the statistical errors on the low-$T$ data are one order of magnitude smaller than those on the high-$T$ data, thus the $\chi^2$-fit neglects the high-$T$ data in favour of fitting the low-$T$ data more accurately. This caused the fit to wrongly determine $\chi_0$, which is of great importance due to the weak signal, since $\chi_0$ is only determined by high-$T$ data.

To make the fit behave correctly, I chose to scale the uncertainties by a factor $c/\sqrt{T}$ before fitting, with $c$ chosen such that the error on the data measured at the highest $T$ is not changed. The resulting fit is shown in Figure 4.3d and yielded $J = 3.2(4)$ K and $j = -0.81^{+0.06}_{-0.07}$ K with $g = 2.204(12)$ while assuming $S = 1$. The errors are again estimated by the change in parameters induced by changing $\chi_0$ by $\pm 33$ %. These results are slightly different from those from 1 T data, which is not unexpected, since I used data at $T < 5$ K this time; a $T$-region where $\chi(T)$ changes rapidly.

Like for the 1 T data, I also fitted the CW model to data. Again, the obtained parameters depended strongly on the lower fit boundary $T_{low}$. I used the same procedure as above to find $T_{low}$; the $J$ vs $T_{low}$-plot is shown in Figure 4.3f, where I found a plateau in the range 54 - 88 K. I again computed the arithmetic mean with integer values of $T_{low}$ (in K) within the plateau and obtained $J = 1.086(10)$ K with $g = 2.1924(4)$ assuming $S = 1$, which corresponds to $\theta_{CW} = 2.90(3)$ K. The CW model with these parameters is shown on Figures 4.3b and 4.3d. These results are again different from the scaling model for the same reason as above, but are in agreement with the CW fit to 1 T data.

Inspired by our findings from neutron spectroscopy, which I present later, I also fitted a ZFS-model (eq. (2.4.29)) to both data sets; these fits are shown as dash-dotted magenta lines on Figures 4.3a and d. They are only visible on the $\chi T$-axis, since the CW-, scaling and ZFS-fits are indistinguishable on the $\chi^{-1}$-axis. The 1 T fit yielded $D = -24.0(4)$ K, $g_{\parallel} = 3.115(2)$ and $g_{\perp} = 1.634(5)$, which corresponds to $g_{iso} = 2.13(5)$, while the 0.1 T fit yielded $D = -19.3^{+1.3}_{-1.4}$ K, $g_{\parallel} = 3.094^{+0.013}_{-0.014}$ and $g_{\perp} = 1.57(3)$, which corresponds to $g_{iso} = 2.08(12)$. No treatment of experimental uncertainties were necessary when fitting the ZFS-model. The parameter uncertainties are again estimated as the parameter changes induced by changing $\chi_0$ by $\pm 33$ % in both cases.

Clearly, both models are excellent fits to data, even though the obtained $D$'s are different from the excitation found with neutron spectroscopy (see Section 4.4). Also, differences between 0.1 T and 1 T results is not surprising, as it is clear from the insert on Figure 4.3a that not considering data at $T \leq 5$ K worsens the fit. However, the $g$-values are indeed surprising. According to Boča, $\underline{\mathbf{g}}$-components outside the range $1.99 - 2.40$ has not been reported[30]. Despite this oddity, the isotropic g-values matches other reports on Ni-compounds[30].

I tried adding a MF perturbation, as described by eq. (2.4.28), to the ZFS-model to account for weak NN exchange interactions. However, such perturbation did not visually improve the fit, and the fit parameters were almost identical, why I deemed the introduc-

tion of an extra parameter into this model redundant. I also tried to lock the $D$-parameter to the excitation energy found with neutron spectroscopy, but it yielded no meaningful result.

### 4.1.2 Cu-LDH

As mentioned in Section 3.1, our Cu-LDH sample contains a small amount of unreacted bayerite, which will, like the non-magnetic part of the actual LDH, give a constant diamagnetic contribution, $\chi_{dia}$, to the measured susceptibility. To correct for this, a contribution of $\chi_{dia} = -3.8{\cdot}10^{-5}$ emu/(mol·Oe)[71] was subtracted from $\chi_{meas}$ before fitting, in addition to the subtraction already performed. Even after the subtraction, the Cu-data showed the same problems as described for Ni-LDH: The 0.01 T data proved to be too noisy to accurately determine the background parameter $\chi_0$, in precisely the same manner as for Ni-LDH, why I again only focus on the 0.1 T and 1 T data. The raw data is shown in Figure 4.4a. As for Ni-LDH, the absence of dents and discontinuities clearly tells that no transition to long range magnetic order happens at $T > 2$ K.

The $H = 1$ T data is shown in Figure 4.4c. This time, the highest largest $M$-value in the linear regime is $M = 750$ emu/(mol Oe), thus $T \approx B/M = 10^4\,\text{Oe}/750\,\text{emu/(mol Oe)} \approx 13$ K is the lowest useful temperature. In addition, only data at $T < T_{cut} = 75$ K can be used in this case due to the bump in $\chi T$ at $T_{cut}$ (see the inset on Figure 4.4c). The bump is absent in all other measurements of Cu-LDH's susceptibility, why we assume it to be an artefact of the experimental setup, especially considering that $T_{cut}$ is similar to the temperature of liquid nitrogen, which is used for cooling in the PPMS.

With these considerations in mind, I again fitted the CW and scaling models to data. The scaling model, now without interchain interaction, easily fit the data in the whole range (13 K - 75 K) yielding $J = 1.293^{+0.005}_{-0.011}$ K with $g = 2.1551^{+0.0005}_{-0.0002}$ while assuming $S = 1/2$. The asymmetrical errors are estimated by considering the change in $J$ obtained by altering the upper fit boundary by 5 K in either direction. The scaling model with these parameters is plotted in Figure 4.4c as a black line.

In contrast, the CW-fit depended strongly on the fitting range. To find the appropriate range, I again iterated over $T_{low}$ as described in the above section and again kept $T_{cut} = 75$ K. The obtained $J(T_{low})$-plot is shown in Figure 4.4e, which revealed a small plateau is the range 32 K - 41 K. I again estimated $J$ with the arithmetic mean method, which resulted in $J = 0.796(8)$ K with $g = 2.1501(3)$ while assuming $S = 1/2$, corresponding to $\theta_{CW} = 0.796(8)$ K; a somewhat different result than from the scaling model. The CW model with these parameters is plotted on Figure 4.4c as a dashed line.

Consider now the $H = 0.1$ T data shown in Figure 4.4d. This time, all data down to 2 K can be used since $T \approx B/M = 10^3\,\text{Oe}/750\,\text{emu/(mol Oe)} \approx 1.3$ K. Again, the scaling model, still without interchain interaction, fit the data in the whole range (2 K - 350 K). However, like for the Ni-LDH data measured at $H = 0.1$ T, it was still necessary to scale

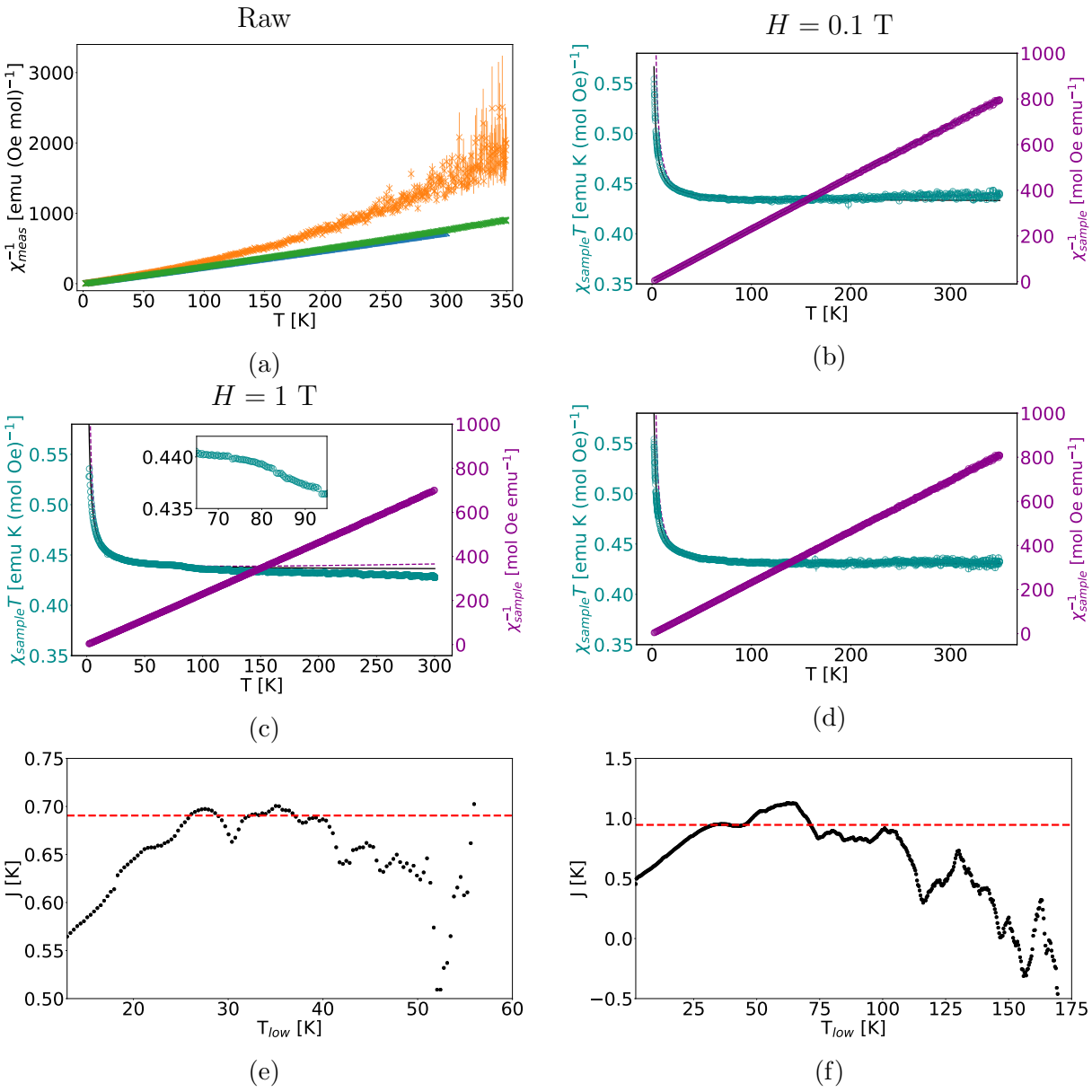


Figure 4.4: $\chi$-data for Cu-LDH. On graphs (a)-(d), only every 10th data point is shown for clarity, and errorbars are smaller than the markers. For (b)-(d), $\chi T$-data is cyan and uses the left y-axis; $\chi^{-1}$-data is magenta and uses the right y-axis. CW-fits are magenta and dashed while non-critical scaling fits are full, black lines. The dashed lines on graphs (e) and (f) show the estimated $J$-values. **(a)**: Raw data measured at $H = 0.01$ T (orange), $H = 0.1$ T (green) and $H = 1$ T (blue). **(b):** Susceptibility data with wrongly estimated background. **(c)**: Susceptibility data with fits fitted for $T < 80$ K. The insert is zoomed at the $\chi T$-bump around $T = 80$ K. **(d)**: Susceptibility data with fits fitted to $T = 350$ K. The uncertainties are scaled by $c/\sqrt{T}$ for the scaling fit. **(e)**: $J$ from CW-fit vs. lower cut-off, $T_{low}$, with a plateau in the range $T = 32$ K - 41 K. **(f)**: $J$ from CW-fit vs. lower cut-off, $T_{low}$, with a plateau in the range $T = 34$ K - 43 K.

the uncertainties by a factor $c/\sqrt{T}$ in order to make the model behave in a meaningful manner at high $T$. Otherwise, the model still has issues fitting the high-T region precisely as shown in Figure 4.4b. From the fit I obtained $J = 1.4(3)$ K with $g = 2.140(15)$ while assuming $S = 1/2$, in agreement with the $H = 1$ T data. The error is again estimated by the change in parameters obtained by changing the fitted $\chi_0$ by $\pm 33$ %.

For this data set, the CW model was even more susceptible to change with variation of $T_{low}$. I used the $T_{low}$-iteration method once more, which revealed plateaus in the ranges 34 K - 43 K and 75 K - 95 K (see Figure 4.4f). Since the plateau at 34 K to 43 K is firmly inside the high-T regime compared to $J$, as is required for the CW model, I chose to use the first plateau to use as much data as possible. I again employed the arithmetic mean method from above and got $J = 1.074(6)$ K with $g = 2.13086(12)$ while assuming $S = 1/2$, which corresponds to $\theta_{CW} = 1.074(18)$ K. This result is close to both scaling model results, but somewhat larger than the CW result for $H = 1$ T. The CW model with these parameters is shown in Figure 4.4d.

### 4.1.3 Co-LDH

The magnetization of Co-LDH, measured at respectively 0.01 T (orange), 0.1 T (green) and 1 T (blue), is shown in Figure 4.5a. Like for the other samples, one finds no dents or discontinuities, and therefore no transition to long range magnetic order, down to 2 K.

Rather peculiar is it however that the data measured at different applied fields are not similar at any temperatures but the very lowest. If Curie-Weiss-like mechanisms governed the susceptibility, the sample should be firmly in the paramagnetic state at high $T$ and therefore behave in the same manner regardless of $H$. Despite that I still tried to fit CW-models to data, since the inverse susceptibility seems to behave in a linear manner, and because it is the go-to method for treating susceptibility data.

As expected, estimating $J$ using CW methods proved difficult or even impossible depending of the applied field. For 0.01 T and 0.1 T data, I succeeded in fitting the CW model to the data, but was not able to estimate $J$ from the fits. Like for both Ni- and Cu-LDH, the obtained fit parameters depended strongly on the choice of lower fit boundary $T_{low}$, and I was not able to find a plateau in $J$ vs. $T_{low}$. However, I found that the CW-fit always yielded a negative $J$-value, which corresponds to AFM NN interactions. Therefore, the scaling model was not employed, as it is derived for FM interactions only.

Things were a bit more successful for the data measured at 1 T. The largest value of $M(H)$ measured inside the linear regime is $M = 4100$ emu/(mol Oe), thus $T = B/M = 2.44$ K is the lowest useful temperature. I again investigated $J$ vs. $T_{low}$ (plotted in Figure 4.5d) and found a plateau in the range 156 K to 198 K. By computing the arithmetic mean from integer values (in K) of $T_{low}$ in the plateau range I got $J = -6.26(2)$ K with $g = 3.0117(10)$ assuming $S = 3/2$, which corresponds to $\theta_{CW} = -31.30(10)$ K. This is a strikingly large $g$-value, but it matches preliminary results from a electron paramagnetic

resonance (EPR) experiment carried out with the assistance of Prof. Jesper Bendix (see Appendix A). From that data, we obtained $g = 2.9$ as the estimated isotropic value from the resonances at $g \approx 2$ and $g \approx 5$. The CW model with the obtained parameters is shown in Figure 4.5b as a dashed line.

I also fitted the low-T regime of the 1 T data with a CW model, since it seems that data shifts to a different slope in $\chi^{-1}$ around $\sim 30$ K. This can be caused by a switch of $\chi$-governing mechanism from single-ion effects at high $T$ to magnetic interactions at low $T$, as is the case for Ytterbium Gallium Garnet, where the high-$T$ susceptibility was accurately reproduced by crystal field calculations[72]. Also, if the $g$-tensor is anisotropic as our EPR result suggests, the single-ion effects are important to consider in regard to the susceptibility.

When fitting CW models to the low-$T$ data, I always fitted from the lower boundary $T = 2.44$ K, and iterated over the upper boundary $T_{upper}$, since the exact spot where the slope changes is not given. The result can be seen in Figure 4.5*e* and shows two plateaus, around 5.5 K and 7.5 K respectively, marked by red lines. A fit with $T_{upper} = 7.5$ K is shown in Figure 4.5b (see insert for details) as a dotted line. Assuming $g = 2.9$ I obtain $J \sim -0.16$ K with $S \sim 1.1$, while assuming $S = 3/2$ yields $J \sim -0.075$ K with $g \sim 2.28$, where the approximate $J$- and $S$-values are aggregates between the results for $T_{upper} = 5.5$ K and $T_{upper} = 7.5$ K.

The success of the low-$T$ CW fit reinforces the idea that different mechanisms govern the susceptibility at different temperatures. For that reason, I employed a model which describes the susceptibility of a compound by only considering the ZFS of the magnetic ions (eq. (2.4.30)). Since this model does not take NN interactions into account, I only fitted data at $T \geq 7.5$ K, which yielded $D = 125(2)$ K, $g_{\parallel} = 3.15^{+0.12}_{-0.14}$ and $g_{\perp} = 2.752^{+0.016}_{-0.014}$, corresponding to $g_{iso} = 2.88(4)$. The uncertainties are still estimated as the parameter changes induced by changing $\chi_0$ by $\pm 33$ %, as the statistical uncertainties from the $\chi^2$-fit were unbelievably small. The model is shown in Figure 4.5c as a black line. It fits the high-$T$ regime very precisely, but, unexpectedly, fails to capture the low-$T$ behaviour.

Therefore, I added a mean-field perturbation, as given by eq. (2.4.28), designed to account for NN exchange interactions at the lowest $T$. In this case, $j$ describes the NN exchange interaction $J$, and $g$ in eq. (2.4.28) is defined as $g \equiv (2g_{\perp} + g_{\parallel})/3$. With this perturbation, I fitted the whole experimental range and obtained $D = 138^{+5}_{-3}$ K, $J = -0.133^{+0.005}_{-0.004}$ K, $g_{\parallel} = 3.02^{+0.14}_{-0.17}$ and $g_{\perp} = 2.81(2)$, corresponding to $g_{iso} = 2.88(5)$. The uncertainties are estimated as above. The model is shown on Figure 4.5c as a red line, and it is clear that the perturbations helps fitting the low-$T$ regime, although not as precisely as the low-$T$ CW fit, which can explain the slight difference in the $J$-values obtained from the two approaches.

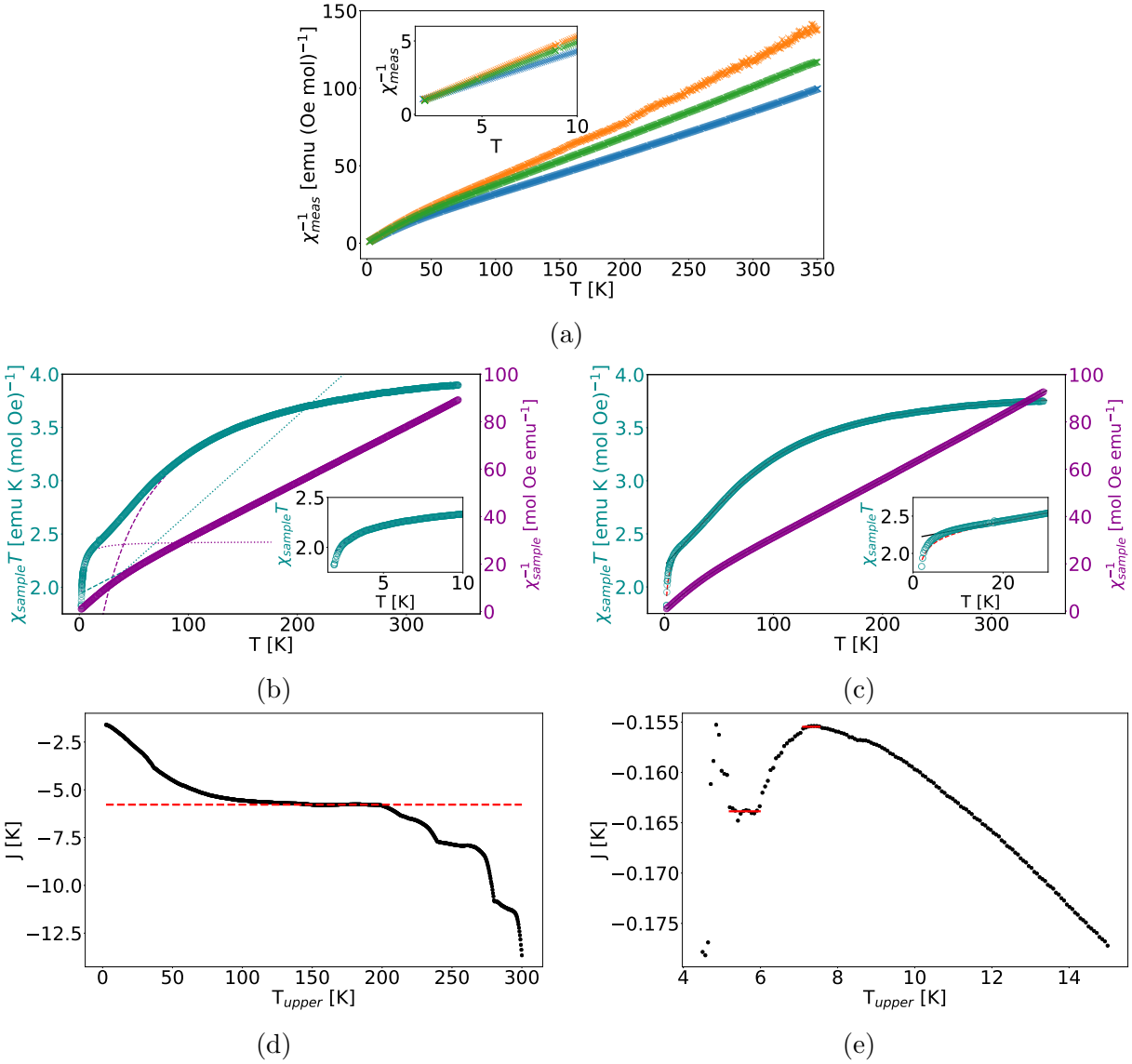


Figure 4.5: Susceptibility data for Co-LDH. On graphs (a)-(c), errorbars are generally smaller than the markers. **(a):** Raw data measured at $H = 0.01$ T (orange), $H = 0.1$ T (green) and $H = 1$ T (blue), plotted as $\chi^{-1}(T)$. **(b):** $\chi_{sample}T$ (cyan, left y-axis) and $\chi^{-1}_{sample}$ (magenta, right y-axis) measured at $H = 1$ T. CW-fits of the low-T (dotted, $T = 2.4$ K - 7.5 K) and high-T (dashed) regimes are shown on both axes. The insert is a zoom on the low-T regime and only shows $\chi T$ with the low-$T$ fit. **(c):** Same data as (b), now with ZFS-models, with and without MF NN interactions in red and black respectively. **(d):** $J$ from high-$T$ CW-fit vs. lower cut-off $T_{low}$ assuming $g = 2.9$. The estimated $J$-value is shown as a dashed line. **(e):** $J$ from low-$T$ CW-fit vs. upper cut-off $T_{upper}$ assuming $g = 2.9$. The plateaus used to give an approximate value of $J$ are shown as red lines.

## 4.2 Heat capacity

The heat capacity measurements I present here were measured on mg-sized M(II)-LDH powder samples with M(II)=$Cu^{2+}$, $Ni^{2+}$, $Co^{2+}$ and $Zn^{2+}$ by Edgar Dachs at Paris-Lodron University Salzburg by low-temperature calorimetry from 2-303 K using a PPMS. $C(T)$ were measured at 60 logarithmically spaced T-points three times, and arithmetic means were computed from that. The averaged data for all compounds is shown in Figure 4.6a.

For the purpose of my work, I am only interested in the magnetic heat capacity, $C_{mag}$ of the samples. Therefore, we measured $C(T)$ of Zn-LDH, a non-magnetic isomorph of the other LDHs, to complement the measurements of the magnetic compounds. Since all four compounds are isomorph, we can used the Zn-data, as described in Section 2.4.4, to estimate the lattice heat capacity. However, simply subtracting the Zn-LDH-signal yielded negative values of $C_{mag}$, which is unphysical. Therefore, the Zn-data ws scaled by a factor close to 1 to avoid negative $C_{mag}$'s. The factor was chosen such that the lowest value of $C_{mag}$ for each compound went to 0, since $C_{mag}$ goes to zero at high $T$. These data sets are what I will analyse in the coming sections.

### 4.2.1 Ni-LDH

Our measurement of Ni-LDH's $C_{mag}$ is shown in Figure 4.6b. To obtain $C_{mag}$, I subtracted $C_{\mathrm{Zn}}$, multiplied by 0.948, from $C_{\mathrm{Ni}}$ for the reasons explained above. The resulting $C_{mag}$ trends towards zero with increasing temperature until $T_{upper} \approx 56$ K, which means that the extraction of $C_{mag}$ works well until approximately that temperature. The heat capacity shows distinct quantum behaviour at low $T$, with a broad maximum at $T_{max} \approx 4$ K, and no signs of transition to long range order, in the form of $\lambda$-shaped peaks or other divergences, are found.

I fitted our data to a model built on Blöthe's exact diagonalization (ED) results on the isotropic $S = 1$ chain, which were described in Section 2.4.4. I did this by fitting a B-spline to the ED data with a least squares method under the constraint $C(0) = 0$. I used the method *minimize* from the scipy python library to optimize the spline coefficients, and the methods *splrep* and *splev* from the scipy sub-package *interpolate* to create and evaluate the B-spline. After creating the model it was fitted to data within the same $T$-range as the ED data, this time with a $\chi^2$-method. The fit yielded $J = 2.17(2)$ K, similarly to the values obtained from $\chi$-data. The error is the statistical error on the fit parameter, and the fit is shown in Figure 4.6b as a cyan line. The ED model fits well for $T \leq 10$ K, as is clear from the insert on Figure 4.6b, but it does not capture broad bump between $T = 10$ K and $T = 30$ K.

When comparing our data to Blöthe's results on anisotropic chains I consistently find that his results show a larger value of $C_{mag}$ at the local maximum compared to our data. For the lowest value of the anisotropy parameter, $|D/J| = 0.5$, Blöthe's data is a factor

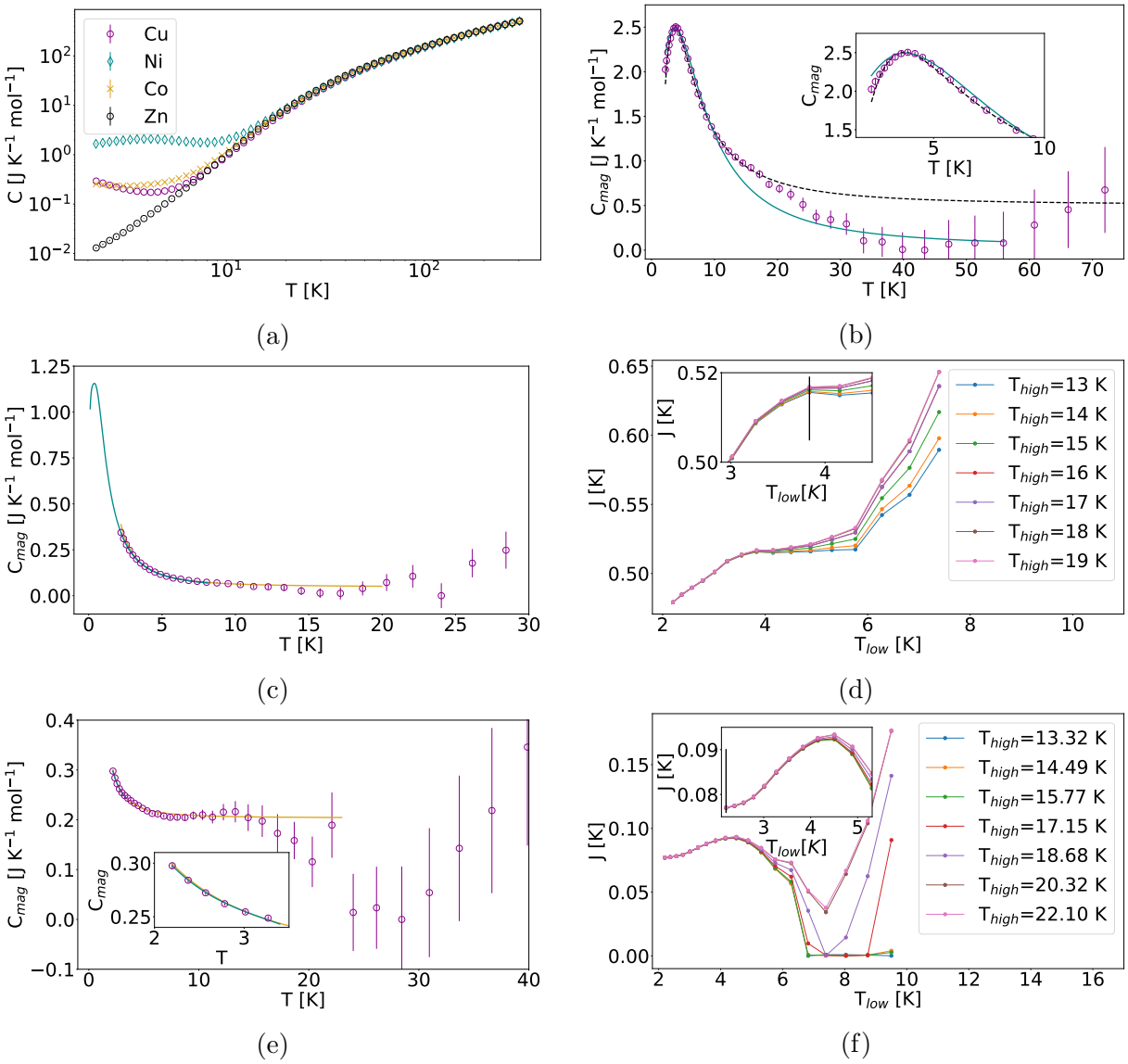


Figure 4.6: Heat capacity data for all LDHs. **(a):** Raw C(T) for all LDHs (see legend) on a double-logarithmic scale. **(b):** $C_{mag}(T)$ for Ni-LDH with ED (cyan) and ZFS (black) fits. **(c):** $C_{mag}(T)$ for Cu-LDH with ED (cyan) and HTE (golden) fits. The HTE model is fitted to data in the range $T$ = 3.83 K - 19 K. **(d):** $J$ from fit of a HTE model to Cu-LDH data as a function of lower fit boundary, $T_{low}$, for different upper fit boundaries $T_{high}$. The insert is zoomed on the chosen $T_{low}$-value, which is marked by a vertical black line. **(e):** $C_{mag}(T)$ for Co-LDH with ED (cyan) and HTE (golden) fits. The HTE model is fitted in the range $T$ = 2.3 K - 23 K. The insert is a zoom on the low-$T$ regime where the HTE and ED fits are nearly identical. **(f):** $J$ from fit of a HTE model to Co-LDH data as a function of lower fit boundary, $T_{low}$, for different upper fit boundaries $T_{high}$. The insert is zoomed on the low-$T$ regime, and the chosen $T_{low}$ is marked by the black line.

1.5 larger than our data at the maximum, and the difference only becomes larger for larger anisotropies, why the anisotropic ED data was not considered any further in regard to the heat capacity data.

However, a pure ZFS-model (eq. (2.4.43)) tells a completely different story. I fitted that model, with an added constant, to the whole available data range ($T \leq 56$ K) and obtained an excellent fit (dashed, black line of Figure 4.6b), which yielded $D = -8.19(5)\,\mathrm{K} = -0.706(4)\,\mathrm{meV}$, similarly to the neutron spectroscopy excitation (see Section 4.4). However, to fit the model, the added constant needed to be quite large; the fit yielded $C_0 = 0.503(8)$ J/(mol K), which corresponds to approximately one-fifth of the total signal. However, the large constant may be an artefact of the aforementioned issues with the extraction of the magnetic signal. The uncertainties are the statistical errors on the fit parameters.

### 4.2.2 Cu-LDH

Data from our measurement of Cu-LDH's $C_{mag}$ is shown in Figure 4.6c. To obtain $C_{mag}$, I subtracted $C_{\mathrm{Zn}}$, multiplied by 0.888, from $C_{\mathrm{Cu}}$ for the same reasons as explained in the beginning of this section. The resulting $C_{mag}$ trends towards zero with increasing temperature until $T_{upper} \approx 19$ K, which means that the subtraction of the lattice contribution works well until approximately that temperature. This is a significantly lower $T_{upper}$ than for Ni-LDH, which is presumably caused by the small amount of unreacted bayerite (see Section 3.1). A small anomaly is seen in the data as an upturn at the lowest T (below $T \approx 5$ K), reminiscent of Blöthe's quantum anomalies. Also, as for Ni-LDH, no signs of transition to long range order is seen.

I again built a model on Blöthe's ED data, this time using his results for $S = 1/2$, and fitted it to data in the same manner as described for Ni-LDH. The result, which yielded $J = 0.583(3)$ K, is shown as a cyan line on Figure 4.6c. From the fit behaviour below our experiment limit of $T = 2$ K, it is clear that the significant $C_{mag}$-features lie below our experimental limit, why it is safe to assume that we are in the high-$T$ regime.

For that reason, I also tried fitting a high-$T$ expansion model (eq. (2.4.42)) to the data. Like the CW model for susceptibility, the HTE model is only approximate, and a proper temperature range needs to be determined. To quantify my choices of the upper ($T_{high}$) and lower ($T_{low}$) fit boundaries, I studied their impact on the obtained $J$-value by iterating over different values. The result is shown in Figure 4.6d, which revealed that $T_{low} = 3.83$ K is the optimal value, since for that value, $J(T_{low})$ has reached a plateau and the choice of $T_{high}$ induces minimal change in $J$ (see the insert of Figure 4.6d for details). In fact, the changes induced by changing $T_{high}$ are lower than the statistical errors on the fit, why I choose $T_{high} = 19$ K to use as much data as possible. These choices of $T_{low}$ and $T_{high}$ yielded $J = 0.514(5)$ K, a little lower than the value obtained from the ED-fit. The fit is shown on Figure 4.6c as a golden line.

### 4.2.3 Co-LDH

As for the susceptibility measurements, the treatment of the Co-LDH $C$-data was more tricky compared to the others. The data, shown in Figure 4.6e, was obtained by subtracting $C_{\mathrm{Zn}}$, multiplied by 0.964, from $C_{\mathrm{Co}}$ for the same reasons as above. It is clear that the extraction of $C_{mag}$ is not perfect. In fact it only works reasonably well for $T \leq 22$ K; in particular, the drop around $T = 22$ K is strange. It is also odd that $C_{mag}$ flattens just above 0.2 J/(K mol) and not around 0. Still, no signs of a transition to long range order is seen.

Despite the oddities, I fitted both an ED and a HTE model, this time with an added constant $C_0$, to the data. For the HTE fit, I again examined the choices of temperature boundaries as for Cu-LDH, the result is shown in Figure 4.6f. I found that $J$ has local maximum at $T_{low} \approx 4.5$ K, and that a plateau is forming as $T$ approaches the lower experiment limit. However, most features in the data lie below $T = 4.5$ K, why I chose to use all data ($T_{low} = 2.20$ K), which is also reasonable since a plateau is forming as $T \to 2$ K. Like for Cu-LDH, the choice of $T_{upper}$ has no effect on the fitted parameter as long as it is large enough. Therefore, to use as much data as possible, I chose $T_{upper} = 22.1$ K. With these choices, the fit yielded $J = 0.0771(8)$ K and $C_0 = 0.2036(10)$ in compliance with the CW result from low-$T$ $\chi$-data when assuming $S = 3/2$. The fit is shown on Figure 4.6e as a golden line.

The ED data, fitted with the same method as for Ni-LDH, is shown as a cyan line on Figure 4.6e (most clearly on the insert). It is only plotted in the $T$-region where ED and experimental data overlap, which shows that the overlap is quite limited. This means that the ED model is only fitted to 6 data points, which limits the fit quality and makes it impossible to use it to estimate a background parameter. Therefore, I locked the background parameter to the value obtained from the HTE fit before fitting the ED model, which which yielded $J = 0.0550(4)$ K, slightly smaller than the HTE value, but still comparable with results from low-$T$ susceptibility data. All uncertainties on fit parameters are the statistical errors on the fitted values.

I was not able to fit a ZFS-model to the heat capacity data, despite the $\chi$-data suggesting an enormous $D$-parameter. When inserting the $D$'s estimated from the $\chi$-data into model presented in Section 2.4.4 (eq. (2.4.44)), the model has a maximum at $T \approx 50$ K and $C(T < 10\,\mathrm{K}) \approx 0$. Due to the issues with the extraction of the magnetic part of the heat capacity, it is impossible to fit such a model to the data, since only data at $T \leq 22.1$ K can be considered.

## 4.3 Neutron Diffraction

The neutron diffraction measurements on Ni-LDH I present here were collected on the thermal diffractometer HRPT at SINQ, PSI (see Section 3.3.3 for instrument details) in

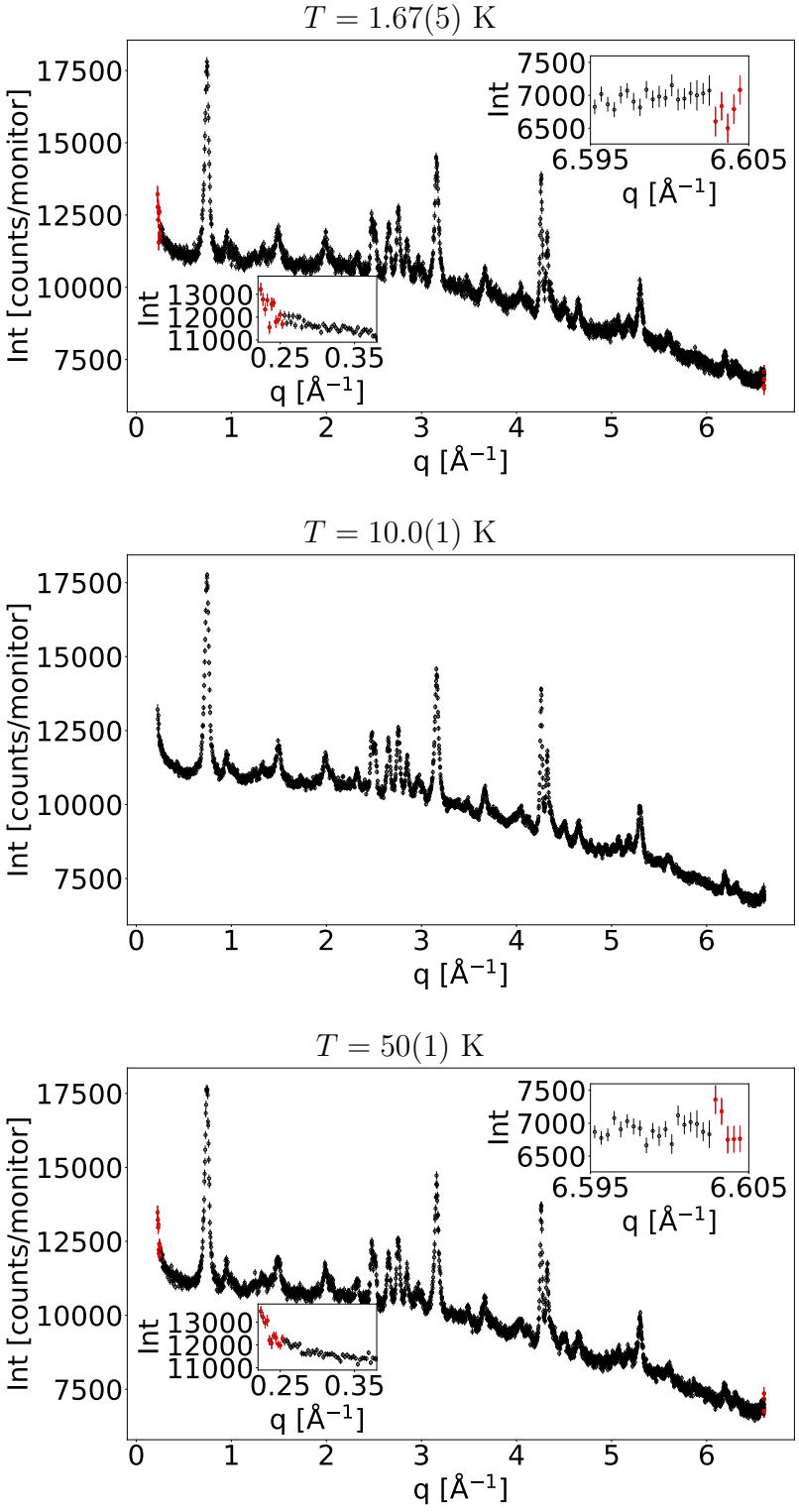


Figure 4.7: Neutron diffraction data of Ni-LDH at different temperatures measured at HRPT at SINQ, PSI in high-intensity mode with $\lambda_i = 1.886$ Å[68]. The red data points, on which the inserts are zoomed, corresponds to the $\Delta I$ data points which needs to be removed to pass the Anderson-Darling test[73] at a 5 % significance level.

November 2020 as a part of the student beam time for the course Neutron Scattering at the University of Copenhagen. Due to the covid-19 situation we were not able to perform the experiment on site. Instead, it was carried out by the instrument responsible Denis Cheptiakov with the assistance of postdoc Henrik Jacobsen. The instrument was operated in the high-intensity mode described in Section 3.3.3 since we were looking for broad magnetic signals, as will be elaborated below, why high flux was immensely more important than good resolution.

The measurements were performed on a 1.003 g partly deuterated powder sample. We used neutrons with $\lambda_i = 1.886$ Å coming from the (511) reflection of the Ge-monochromator, and we measured for 3 hours at $T = 1.67(5)$ K, $T = 10.0(1)$ K and $T = 50(1)$ K.

The data is shown in Figure 4.7 for each of the three temperatures, and it is clear upon first inspection that they are quite identical. The data was normalised to a standard monitor count by D. Cheptiakov, who also properly propagated the statistical errors while taking into account the relative efficiencies of the detector wires, which differ by ±10 %. Regardless of temperature, we find ca. 20 Bragg peaks, which presumably are the nuclear peaks. Also, a significant non-flat background is present at all temperatures, presumably due to incomplete deuteration of our Ni-LDH sample, which leaves $^1$H, which has a very large incoherent cross section[20].

From eq. (3.3.12), one has that the magnetic diffraction signal is essentially the space Fourier transform of the spin correlation function. In the case of a magnetically ordered sample, it means that one would observe magnetic Bragg peaks when $\mathbf{q}$ is equal to the magnetic ordering vector, give or take a reciprocal lattice vector as given by eq. (3.3.14). However, as mentioned in the above sections, magnetic ordering is absent in Ni-LDH down to $T = 2$ K and thus no magnetic Braggs peaks could emerge at $T = 10.0(1)$ K or $T = 50(1)$ K. Since the $T = 1.67(5)$ K diffractogram is more or less identical to these, we can confirm that no magnetic ordering is present at that temperature either.

Still, short-ranged magnetic correlations can exist in the disordered phase close to a transition and still scatter neutrons as described by eq. (3.3.12). This phenomenon is referred to as critical scattering, and manifests itself as broad peaks with Lorentzian line shapes at the same $\mathbf{q}$-values as where Bragg peaks will eventually develop in an ordered phase[66]. The signals can be weak and troublesome to distinguish from the nuclear signal since they are much less intense. Especially critical scattering signals at ferromagnetic $q$-values can be difficult, as they will coincide with the nuclear Bragg peaks, since $\mathbf{Q} = 0$ for ferromagnetic ordering, which, if any, is the kind of order we would expect to see given the $\chi$- and $C_m$-results. To magnify eventual magnetic features, I choose to look at the difference $\Delta I (= I_{1.6\,\mathrm{K}} - I_{50\,\mathrm{K}})$ between the $T = 1.67(5)$ K and $T = 50(1)$ K diffractograms. If spin correlations are present, we expect them to be stronger at low $T$ and thus emerge as positive peaks in $\Delta I$.

$\Delta I$ is shown in Figure 4.8a. To further magnify eventual features, I also plotted

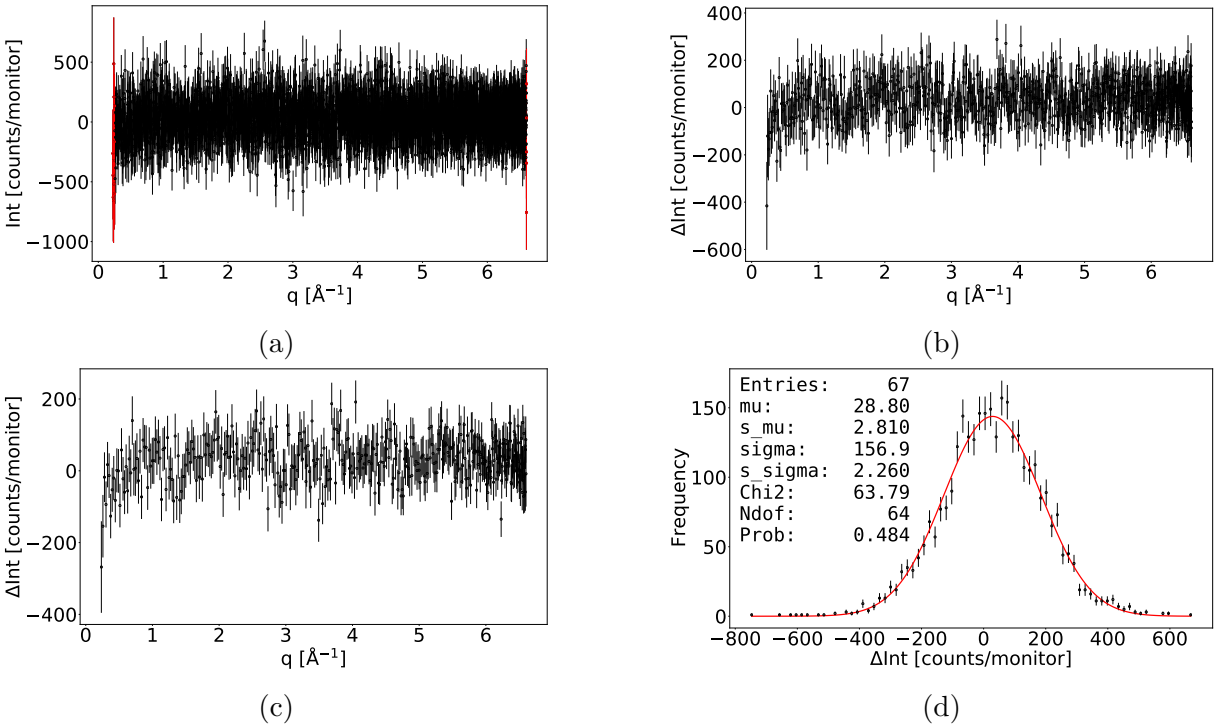


Figure 4.8: Difference ($\Delta I = I_{1.6\,\mathrm{K}} - I_{50\,\mathrm{K}}$) between diffractograms measured at $T = 50(1)$ K and $T = 1.67(5)$ K. **(a):** Unbinned data. The points coloured red needs to be removed for this data to pass the Anderson-Darling test[73] for normality. **(b):** Running average of 4 data points. **(c):** Running average of 8 data points. **(d):** Histogram of $\Delta I$ from (a) with a scaled Gaussian (red) fitted to data with a $\chi^2$-method. The parameters are written on the graph. Errors on each bin is the square root of the frequency.

running averages of 4 and 8 data points in respectively Figures 4.8b and 4.8c. It is clear that no features are seen except for a small decrease in $\Delta I$ at the lowest $q$. However, it is negative and therefore not of magnetic origin, since we expect $\Delta I > 0$ for any magnetic signal. One possible explanation for this decrease is that the part of the detector which measures the neutrons with lowest $q$ is close to the direct neutron beam. This means that even a tiny displacement of the detector bank between measurements could result in capturing a little more of the direct beam. Even though the decrease is around 750 counts/monitor, it only corresponds to $\sim 5$ % of the actual measurement and thus could easily be caused by the mentioned instrument error. The apparent absence of magnetic signals down to $T = 1.67(5)$ K suggests that little spatial spin correlations are present down to that temperature, which underlines that an eventual ordering temperature would be at significantly lower $T$.

Recall now that each data point is simply counts in a neutron detector and therefore independent measurements obeying Poisson statistics. However, the count numbers are large and the probability to hit a specific detector is small, why the distribution of counts

in each detector can easily be approximated to be Gaussian. If $I_{1.6\,\mathrm{K}}$ and $I_{50\,\mathrm{K}}$ are truly identical, and there is no magnetic signal, then each of the aforementioned independent Gaussian distributions will be identical. This ultimately means that the set $\Delta I$ should be Gaussianly distributed if there is no magnetic signal.

To investigate if that is the case, I plotted a histogram of the data in Figure 4.8a, which is displayed in Figure 4.8d. I used 80 bins, which lead to 67 actual entries since 13 bins were empty. The observed frequencies are assumed to follow count statistics, thus a Poisson distribution, why the errors on the frequencies are set to the square root of the bin counts. I used a $\chi^2$-method to fit a Gaussian distribution, scaled by a factor $N$, to the histogram. It fit nicely ($\chi^2_{red} = 0.997$) and yielded $\mu = 29(3)$ counts/monitor and $\sigma = 157(2)$ counts/monitor, thus the fit strongly suggests that $\Delta I$ is in fact normal distributed. Having $\mu > 0$ is to be expected, as the cross sections is proportional to the Debye-Waller factor, which is larger for lower temperatures.

To further strengthen the claim that $\Delta I$ is in fact normal distributed, I performed and Anderson-Darling (AD) test for normality[73] on both the unbinned and the two binned data sets. My null hypothesis was that the data is normal distributed, meaning that $\Delta I$ is merely statistical noise. For the two binned data sets, I obtained test statistics $A^2 = 0.463$ and $A^2 = 0.457$ for the running average of 4 and 8 data points respectively (see [73] for details on $A^2$), which means the null hypothesis could not be discarded even at a 15 % confidence limit. However, the unbinned data set did not pass the test immediately, as an AD test on the full, unbinned data set yielded $A^2 = 1.31$. My initial guess was that this was caused by the dip at lowest $q$ explained above, which would be smoothed out in the binned case. I found that removing the first 11 and the last 5 data points from the unbinned data, all coloured red in Figures 4.7 (top & bottom) and 4.8a, led to the unbinned data passing the AD test at a 5 % significance level with $A^2 = 0.763$. I have good reason to remove data points at the lowest $q$ as explained above, but no explanation for why removing an amount of data at the highest $q$ is required for passing the AD test.

## 4.4 Neutron Spectroscopy

The neutron spectroscopy measurements on Ni-LDH I present here were collected on the FOCUS time-of-flight spectrometer at SINQ, PSI (see Section 3.3.4 for instrument details) as a part of the student beam time for the course Neutron Scattering at the University of Copenhagen. Due to the covid-19 situation, we were not able to perform the experiment on site. Instead, it was carried out by Henrik Jacobsen and the instrument responsible Jan Peter Embs. The experiment ended on Dec. 16th, only a few days before this thesis was handed in, why the data treatment is not as thorough as one could have wished.

The measurements were performed on a 1.003 g deuterated powder sample with the incoming energy $E_i = 3.55$ meV at $T = 1.5$ K for 10 hours, and at $T = 100$ K for 3.5

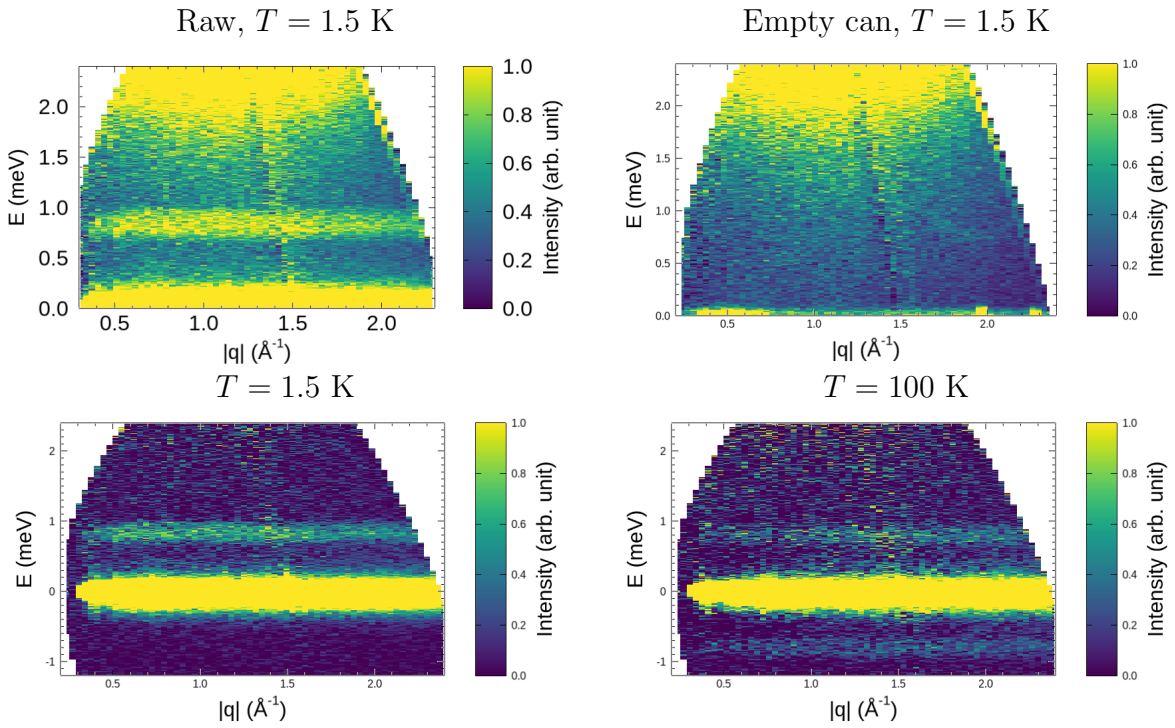


Figure 4.9: **Top:** Raw inelastic neutron scattering intensity of Ni-LDH at $T = 1.5$ K (left) and empty-can measurement (right) at $T = 1.5$ K. **Bottom:** Inelastic neutron scattering intensity of Ni-LDH at $T = 1.5$ K (left) and $T = 100$ K (right), with background subtracted. All measurements are performed on a 1.003 g deuterated powder sample at the TOF-spectrometer FOCUS at SINQ[70]. The plots are made with the MSlice software[74].

hours. I performed the reduction of the TOF-data with the DAVE software[75], and MSlice was used for making the 1D cuts shown later[74]. For background estimation, the empty sample can was measured for 9 and 5 hours at $T = 1.5$ K and $T = 100$ K respectively, whereafter the empty can signals were subtracted from the raw data. The raw data and empty can signal for $T = 1.5$ K can be seen in Figure 4.9 (top left and right respectively).

Colormaps of the two data sets, with background subtracted, can be seen in Figure 4.9 (bottom). A well-defined, $|q|$-independent peak is seen at $E \approx 0.8$ meV at both temperatures. The peak is presumably a crystal field excitation, as the presence of a ZFS can give rise to such a dispersion-less excitation as described in Section 2.5.1. This can explain the lower intensity at $T = 100$ K, as the excited ZFS level will also be populated at $T = 100$ K, seen as scattering at negative $E$, which is indeed the case (see Figure 4.9, bottom rigt). The total amount of scattering must be constant, thus the scattering at $E > 0$ must become less intense. This also confirms the two-level nature of the excitation, which certainly agrees with the idea of the it being caused by a ZFS. Alternatively, frustrated magnetic systems can give rise to similar scattering patterns named zero modes[76], but we have no reason to believe that that is the case here[77].

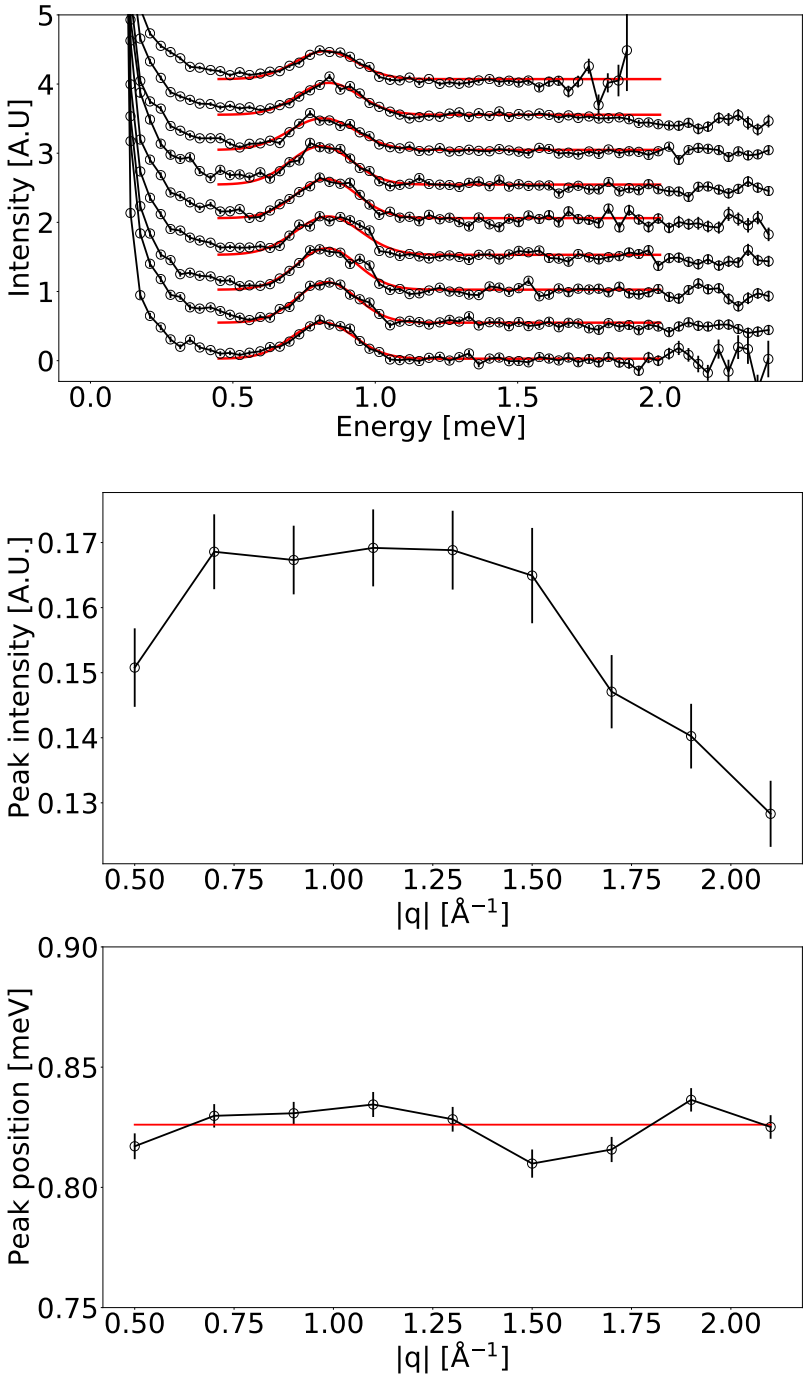


Figure 4.10: Investigation of $T = 1.5$ K crystal field data from Figure 4.9. **Top:** Cuts along $E$, integrated over 0.2 Å$^{-1}$ from $|q| = 0.4 - 2.2$ Å$^{-1}$. Each cut is shifted by 0.5 A.U. for increasing $|q|$. The red lines are Gaussians with constant background contributions, fitted to the range $E = 0.45 - 2.00$ meV using a $\chi^2$-method. **Middle:** Integrated peak intensity, defined as given in the text, vs. $|q|$, where the value at e.g. $|q| = 0.5$ corresponds to the result from the fit of the $E$-cut integrated from $|q| = 0.4 - 0.6$ Å$^{-1}$. **Bottom:** Peak position vs. $|q|$, with a constant $E = 0.8261(17)$ meV (red line) fitted to data with a $\chi^2$-method.

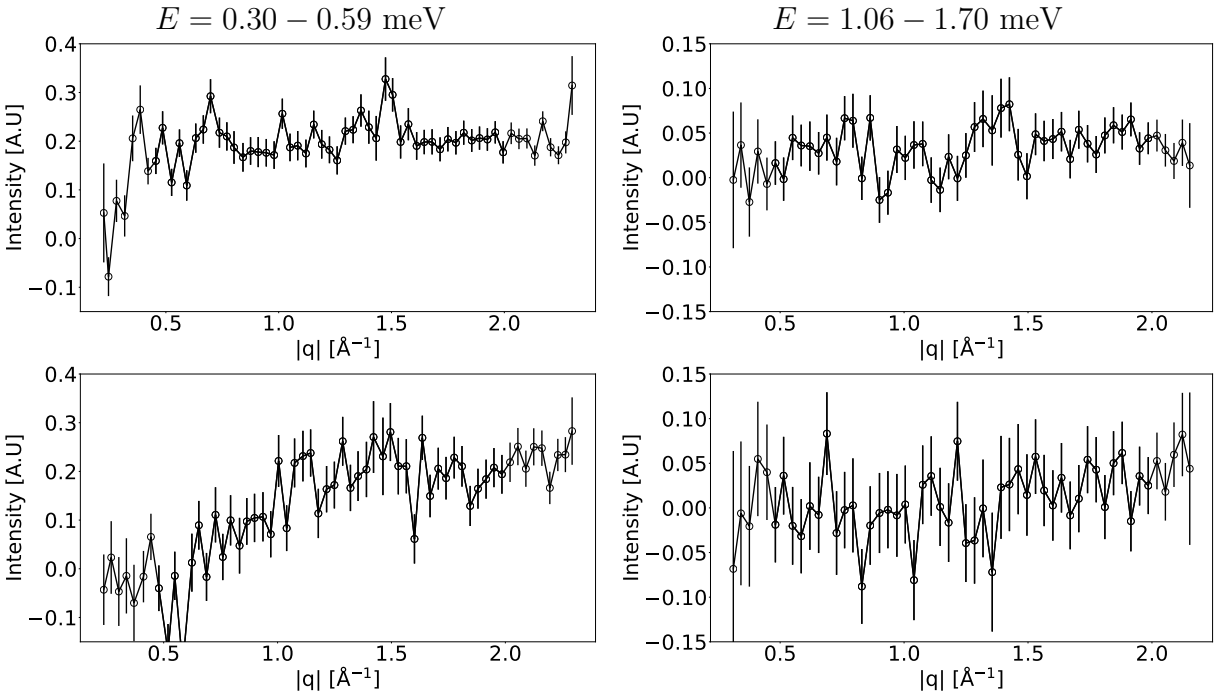


Figure 4.11: Inelastic neutron scattering intensity of Ni-LDH, integrated along respectively $E = 0.30 - 0.59$ meV (left) and $E = 1.06 - 1.70$ meV (right), as a function $|q|$ at $T = 1.5$ K (top) and $T = 100$ K (bottom).

To investigate the nature of the signal at $E \approx 0.8$ meV, I made cuts of the $T = 1.5$ K data along the $E$-axis, integrated over 0.2 Å$^{-1}$ in $|q|$. These cuts are shown in Figure 4.10 (top), where successive cuts have been shifted by +0.5 A.U. to be able to show all cuts in the same plot; the lowest-lying data, which have not been shifted, corresponds to the lowest $|q|$. I fitted a Gaussian peak shape, with a constant background contribution, to each cut in the range $E = 0.45 - 2.00$ meV; these are shown on Figure 4.10 (top) as red lines. First- and second-order polynomials were also considered for modelling the background, but they did not unambiguously make the fits better, and they ultimately made the estimates of the Gaussian parameters less precise, why they were abandoned. Also, they yielded negative intensities within the experimental range, which is unphysical.

Due to the magnetic form factor in eq. (3.3.18), the intensity of magnetic scattering signals decrease as $|q|$ increases, as described in Section 3.3.1. To investigate the magnetic nature of the signal at $E \approx 0.8$ meV, I computed the integrated intensity of the fitted Gaussian peaks as $I_{int} = \sqrt{2\pi}\sigma I_{max}$, where $I_{max}$ is the maximal intensity of the peak and $\sigma$ is the Gaussian line width. I show $I_{int}(|q|)$ in Figure 4.10 (middle), where $|q| = 0.5$ Å$^{-1}$ corresponds to an integration over the interval $|q| = 0.4 - 0.6$ Å$^{-1}$ , from which it is clear that from $|q| = 1.5$ Å$^{-1}$, the intensity decreases as $|q|$ increases.

For comparison, H.A. Mook found that nickel's form factor deviates very little from it's peak value for $|q| < 1$ Å$^{-1}$ [78], and R. Nathans et al found that it plummets for $|q| > 2$

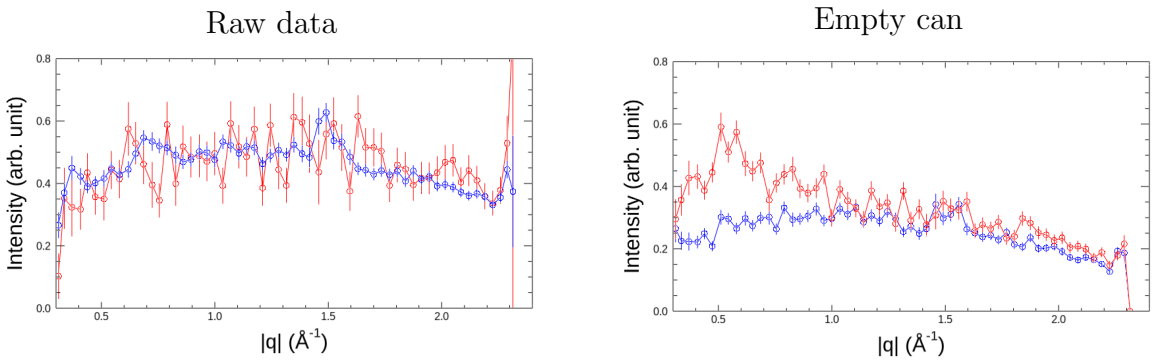


Figure 4.12: **Left:** Raw data measured at $T = 1.5$ K (blue) and $T = 100$ K (red), integrated over $E = 0.30 - 0.59$ meV, as a function of $|q|$. **Right:** Empty can data measured at $T = 1.5$ K (blue) and $T = 100$ K (red), integrated over $E = 0.30 - 0.59$ meV, as a function of $|q|$.

Å$^{-1}$ [79], which is also true for our excitation. Thus, the signal is indeed magnetic. During our experiment, the FOCUS detector was known to have low efficiency at low $|q|$, why a low $I_{int}$ at low $|q|$ is expected [80].

To give an estimate of the exact excitation energy, I investigated the peak position's dependence on $|q|$ as displayed in Figure 4.10 (bottom). It is clear that the peak position is effectively constant, and I obtained $E = 0.8261(17)$ meV $= 9.59(2)$ K by fitting a constant to the data with a $\chi^2$-method. Neutron spectroscopy is not able to estimate the sign of $D$, as it simply measures the energy gap between the crystal field levels. The obtained energy is similar to the estimate from the ZFS-fit to heat capacity data, but only about half of the estimate from the ZFS-fit to susceptibility data.

To look for any hidden magnetic signals, I investigated the seemingly empty areas of $I(E, |q|)$ away from the CF-excitation. I integrated the areas $E = 0.30 - 0.59$ meV and $E = 1.06 - 1.70$ meV and plotted their $|q|$-dependence as shown in Figure 4.11 (left and right respectively). The $E$-intervals were chosen to always be more than $2\sigma$ away from the excitation maximum. The intensity of the high-$E$ region is indistinguishable from zero within the errorbars regardless of temperature, thus no signal is hidden there.

The low-$E$ region is different however, as there definitely is a signal with strength $I \approx 0.2$ A.U. At low $T$, the signal seems to be constant in $|q|$; the dip at the lowest $|q|$ is presumably caused by the aforementioned issues with the detectors at small angles. At high $T$, the signal is constant for $|q| > 1$ Å$^{-1}$ , but decreases in intensity for low $|q|$. While surprising at first, it can be explained by the fact that the raw signal does not change with temperature (see Figure 4.12 (left)), while the 100 K empty-can data is more intense than the 1.5 K empty-can data at low $q$ (see Figure 4.12 (right)). Thus, the difference between the top-left and bottom-left panels on Figure 4.11 is presumably an artefact of the background subtraction.

# Chapter 5

# Discussion, Conclusion & Outlook

This is the final chapter of my thesis. Here, I will collect and discuss all my findings before I formulate my final conclusions and give my thoughts on possibilities for further work. At first, I will discuss a few features which are common for each sample, whereafter I consider them individually, as they all proved to require specific treatment.

## 5.1 Discussion

In this work, I have studied the magnetic properties of a series of layered double hydroxides based on bayerite, namely $M(II)Al_4(OH)_{12}SO_4 \cdot 3\,H_2O$ with M(II)=$Cu^{2+}$, $Ni^{2+}$ and $Co^{2+}$, mainly by measuring their heat capacity and magnetic susceptibility. An overview of the obtained parameters is found in Table 5.1.

Despite being isomorph compounds, I had to employ several different models to account for the individual intricacies of the bulk properties of our LDHs, as will be elaborated below, which bodes well for the possibility for synthesising compounds with different magnetic properties based on this LDH family. One thing they did have in common however: Their bulk magnetic properties behaved smoothly as functions of temperature down to $T = 2$ K, as seen in Figures 4.3 through 4.6. This clearly confirms the absence of long-range magnetic order in all samples, as described in Section 2.3, which is a first step in investigating if our LHDs are good realisations of 1D quantum systems, as true 1D isotropic Heisenberg systems do not order according to the Mermin-Wagner theorem [13].

In addition to the measurements mentioned above, we investigated the magnetic properties of Ni-LDH with both neutron diffraction and spectroscopy, as presented in Sections 4.3 and 4.4. These experiments were severely delayed due to the covid-19 pandemic, why the data treatment is not as thorough as one could have wished. Furthermore, preliminary results from electron paramagnetic resonance spectroscopy of Co-LDH (see Appendix A), measured in collaboration with Prof. Jesper Bendix (Department of Chemistry, Univ. Copenhagen), will be discussed in this section.

| | | Cu-LDH | Ni-LDH (0.1 T) | Ni-LDH (1 T) | Co-LDH (1 T) |
|---|---|---|---|---|---|
| $\theta_{CW}$ | [K] | 1.074(6) | 2.90(3) | 2.981(6) | $\sim -0.49$ |
| $J_{CW}$ | [K] | 1.074(18) | 1.086(10) | 1.12(2) | $\sim -0.075^{(a)}$ |
| $J_{\text{scaling}}$ | [K] | 1.4(3) (0.1 T)<br>$1.293^{+0.005}_{-0.01}$ (1 T) | 3.2(4) | 3.84(14) | - |
| $J_{\text{ZFS},\chi}$ | [K] | - | - | - | $-0.133^{+0.005}_{-0.004}$ |
| $\lvert J_C \rvert$ | [K] | 0.583(3) (ED)<br>0.514 (5) (HTE) | 2.17(2) (ED) | | 0.0771(8) (HTE) |
| $j$ | [K] | - | $-0.81^{+0.06}_{-0.07}$ | $-1.07(2)$ | - |
| $D_\chi$ | [K] | - | $-19.3^{+1.3}_{-1.4}$ | $-24.0(4)$ | $138^{+5}_{-3}{}^{(b)}$ |
| $D$ | [K] | - | $-8.19(5)$ (ZFS)<br>$9.59(2)^{(c)}$ (INS) | | - |
| $g_{CW}$ | | 2.13086 (12) | 2.1924(4) | 2.24311(9) | $\sim 2.28^{(a)}$ |
| $g_{\text{scaling}}$ | | 2.140(15) (0.1 T)<br>$2.1551^{+0.0005}_{-0.0002}$ (1 T) | 2.204(12) | $2.250^{+0.004}_{-0.005}$ | - |
| $g_{iso,\text{ZFS},\chi}$ | | - | 2.08(12) | 2.13(5) | 2.88(5) |

Table 5.1: Overview of magnetic parameters obtained from measurements of our LDHs' magnetic properties. The given errors are estimated using the methods described in Chapter 4. $\theta_{CW}$, $J_{CW}$ and $g_{CW}$ are obtained by fitting Curie-Weiss models (eq. (2.4.18)) to susceptibility data. $J_{scaling}$, $j$ and $g_{scaling}$ are obtained by fitting non-critical scaling models (eq. (2.4.27)) to susceptibility data. $J_{\text{ZFS},\chi}$, $g_{iso,\text{ZFS},\chi}$ and $D_\chi$ are obtained by fitting ZFS-models (eqs. (2.4.29)-(2.4.30)) to susceptibility data. $J_C$'s are obtained from fitting high-temperature expansion (HTE, eqs. (2.4.40) or (2.4.42)) and/or exact diagonalization (ED) models to heat capacity data; the exact models are given in parentheses. $D$ is estimated by fitting a ZFS-model (eq. (2.4.43)) to heat capacity data, or obtained directly from inelastic neutron scattering (INS) data; the exact model is given in parenthesis. The VSM applied field strengths are also given in parentheses. (a): With $S = 3/2$. (b): With a MF NN exchange perturbation. (c): INS only gives the magnitude of $D$.

When looking at the susceptibility data of all three LDHs (Figures 4.3-4.5), it is clear that the inverse susceptibilities generally behave in a linear manner at high $T$, in addition to behaving smoothly as a function of temperature. Indeed, I was able to fit Curie-Weiss models (eq. (2.4.18)) to all data sets, which in the literature is the go-to method for treating this kind of data; the obtained parameters will be discussed later in this section.

However, determining a unique set of fit parameters from CW models was not an easy task. Intrinsically, the CW-model is a high-T model, as it is derived in the high-T limit (see Section 2.4.3). Therefore, one has to choose a limited range of data to which the model should be fitted. To quantify my choices of fit boundaries, I investigated their influence on the obtained parameters (see Figures 4.3e-f, 4.4e-f and 4.5d-e). To my surprise, it was often difficult to find an unambiguous best choice of fitting range even with this method. Also, even within intervals of lower boundaries which were supposed to be equally good, my choices caused parameter fluctuations larger than the statistical uncertainties from the fits. I therefore chose to combine parameters from within equally good intervals by computing arithmetic means as described in Section 2.4.3; those are given in Table 5.1.

The uncertainties on parameters obtained in the above manner were estimated as the errors on the means; these are also the ones given in Table 5.1. This choice of uncertainty estimation yields three significant figures on $J$, and four to six significant figures on $g$, which, compared to similar kinds of results reported in the literature, are quite precise[23,32,34,81]. My method probably underestimates the uncertainties, especially when compared to the uncertainties from the other models I have employed (see Table 5.1), but at least it does not re-introduce the choice bias I had tried hard to eliminate.

Given the issues with the CW model, I also employed a non-critical scaling model (see Section 2.4.3) when applicable. According to the original authors, this model is valid down to $k_B T > 0.1\,J$[32], which means it would be applicable to the whole experimental range if the initial CW-results were correct. In some cases however, I had trouble fitting the model precisely in the high-temperature region, which became most apparent when plotting $\chi T$, which underlines the importance of fitting $\chi T$ in addition to the traditional $\chi^{-1}$. I found that the error was mainly caused by wrong estimation of the background.

However, rather than being an issue with the model, it turned out to be an issue with the fitting method and the experimental uncertainties. I used a $\chi^2$ fitting routine, which intrinsically puts a lot of weight on data with small uncertainties and only takes statistical uncertainties into account[82]. My experiments were performed with a vibrating sample magnetometer, which uses lock-in amplifiers to measure tiny currents, induced by the magnetised sample, to high accuracy (see Section 3.2). The accuracy becomes even greater as the sample is cooled, since the sample magnetisation gets larger and thus induces a higher voltage, why the statistical uncertainties on low-T data become minuscule. This leaves room for small systematic errors to have an impact, especially considering the weak magnetic signals. Such systematic errors are presumably not temperature depen-

dent, contrary to the statistical ones, thus they will become relatively more important as the sample is cooled. Since the $\chi^2$ fitting method does not consider these systematic uncertainties, it wrongly puts great emphasis on the low-T data and neglects the data at high T, which determines $\chi_0$, which was important to estimate correctly due to the weak signal. I therefore forced the fitting routine to put a greater emphasis on the high-T data by multiplying the statistical uncertainties by $c/T^{1/2}$, choosing $c$ such that the uncertainty on the data point at the highest $T$ was unchanged.

Like for the CW model, I was forced to estimate the parameter uncertainties in an unconventional manner when employing the above method, since the statistical uncertainties on the fit parameters were on the fourth significant figure; a level of precision I deemed impossible due to the fitting difficulties. Instead, my estimation was that the uncertainties are given by the parameter changes induced by altering $\chi_0$ by $\pm 33$ %, motivated by the fact that $\chi_0$-estimation had already proved to be a decisive factor.

I also had to face difficulties when treating the heat capacity. I am only interested in the magnetic contribution, which needs to be extracted from the raw data, which also contains the lattice vibration contribution. I tried to do so by estimating the lattice heat capacity of the magnetic samples as the heat capacity of the non-magnetic Zn-LDH. This way, simply subtracting the Zn-LDH data from the others would extract the magnetic data. Unfortunately, this method yielded negative $C$-values, which is unphysical. This means that the lattice heat capacitiy of Zn-LDH is not completely equal to that of the others, presumably due to small differences in the lattice parameters and the atomic masses. To avoid negative $C$-values, the Zn-data was scaled by small factors close to 1, which removed the negative values. However, the subtraction still was not perfect. The magnetic heat capacity did not go to zero at high temperatures contrary to expectation (see Figure 4.6). Regardless, the subtraction seemed to work well until temperatures much larger than the $J$-values estimated from the $\chi$-data, why assessing the magnetic properties from the heat capacity data should not be problematic.

I always fitted at least one of the two following models to the heat capacity data: One derived from a high-temperature expansion of the partition function, and one built on Blöthe's exact diagonalization (ED) results[37,38], which both have their limitations. Most of the concerns regarding the CW model for susceptibility are also applicable for the HTE model, and for that reason, I again evaluated the influence of the fitting range on the obtained parameters, as I had done for the CW model (see e.g. Figure 4.6d). Blöthe's ED data is naturally limited to a certain temperature range, why the model also had to be, thus in certain cases it might have limited overlap with the experimental data as well.

### 5.1.1 Cu-LDH

Our susceptibility and heat capacity data for Cu-LDH can be found in Figures 4.4 and 4.6c respectively. The parameters obtained from different models can be found in Table 5.1,

which tells that Cu-LDH is a $S = 1/2$ spin chain with weak ferromagnetic interactions. Contrary to the other LDHs, there is no zero-field splitting in Cu-LDH, as that is not possible in a $S = 1/2$ system.

As mentioned in Section 3.1, our Cu-sample contained a small amount of unreacted bayerite. This does not effect our susceptibility measurements, as bayerite's diamagnetic susceptibility is tabulated[71], thus it was simple to subtract it's constant contribution from our data. I measured the susceptibility using applied field strengths of $H = 0.01$ T, 0.1 T and $H = 1$ T. The first was not considered for determining the magnetism, as the signal-to-noise ratio is significantly worse compared to the others. Both the others were used, even though the $H = 1$ T data had some issues. As displayed on Figure 4.4c (insert), I found a strange feature in the $H = 1$ T data not present in any other data sets. It is presumably from the experimental setup, as it matches the temperature of $LN_2$ used for cooling. It is worth to notice that the feature is not visible on the $\chi^{-1}$-plot, which emphasises the need for also plotting $\chi T$ when dealing with susceptibility data.

Due to the anomaly, I could only use part of the $H = 1$ T data set (up to $T = 75$ K), which made background estimation significantly harder, especially for the Curie-Weiss model. Due to the weak signal ($\chi(350\,\mathrm{K}) \approx 1.25 \cdot 10^{-3}$ emu/(mol Oe)), background estimation has a big impact on the obtained parameters, why I do not include the CW results from $H = 1$ T data in the further discussion.

To make things more cumbersome, Cu-LDH displays the fastest magnetic saturation of any of our LDHs (see Figure 4.1). At $T = 2$ K, $H = 1$ T is not inside the linear regime, thus the full $M(T)$ data set cannot be used to obtain the susceptibility for $H = 1$ T. I estimated that only data at $T \geq 13$ K can be used, which limits the useful data to the range $13 - 73$ K for the $H = 1$ T data set. Despite that, scaling model results from $H = 0.1$ T and $H = 1$ T are in compliance (see Table 5.1), which underlines the robustness of the scaling model.

The accuracies of the $H = 1$ T results are an order of magnitude better compared to the $H = 0.1$ T results, which might be surprising at first, since the fit range was rather limited for the $H = 1$ T data. It might be caused by the different approach to error estimation, as described in Section 4.1.2, but the S/N-ratio is better for $H = 1$ T, why improved accuracy can be justified. Also, unlike for the $H = 0.1$ T data, I did not have to scale the uncertainties on the $H = 1$ T data for the scaling model to fit the high-T data, which may explain why the $H = 1$ T data can yield parameters with improved accuracy.

Despite the issues with the CW model mentioned in the beginning of this section, I still obtained reasonable results for the $H = 0.1$ T data when taking the proper measures. My fit (Figure 4.4d, magenta line) uses the parameters obtained from of the mean-method mentioned above and is clearly a good fit to data. The fit becomes worse at the lowest temperatures, as expected for the Curie-Weiss model. The scaling model was also applicable to the $H = 0.1$ T data, after correcting the uncertainties as mentioned above. At

low $T$, it fits the data even more precisely than the CW model (black line, Figure 4.4d), and the obtained parameters are close to those from the CW-model (see Table 5.1).

Despite the necessity to scale the uncertainties for the $H = 0.1$ T data, I have most faith in the scaling model. The parameters I obtained with it from the different data sets are within each other's uncertainties, and it provided the best fits at low $T$. Also, the need for scaling the uncertainties can be explained from a statistical perspective, as mentioned in the beginning of the chapter, and it was only necessary when using data not accounted for with the CW model - had the CW model also been applicable to the lowest $T$, scaling of the uncertainties might have been necessary as well.

Both the HTE and ED models were applicable to the Cu-LDH heat capacity data. The obtained $J$-parameters can be found in Table 5.1. Both models yielded ferromagnetic $J$-values, like the susceptibility models, but they both predicted $J$ to be about 40 % smaller than the susceptibility models. Getting a different $J$-value is not a surprising result, for two reasons: First, none of the $C$-models take the unreacted bayerite into account, and secondly, there is only a limited magnetic signal within the available temperature range. It also speaks to $C-$models' favour that they obtained approximately the same parameters - the heat capacity data tells almost the same thing regardless of model. Therefore, the reason for the discrepancy between $\chi$- and $C$-data should probably be found in the underlying assumptions, which again leads back to the 13 %(w/w) unreacted bayerite not being accounted for in the $C$-modelling.

Intrinsically, the HTE model has similar issues to the CW model, as described in the beginning of this chapter, why evaluation of the fitting range was necessary. However, compared to the susceptibility data, it was more clear what the choice of fitting range should be, since the $J$-parameter depended on the boundaries in a simpler manner (see Figure 4.6d). Also, most of the available range proved useful (3.84 - 19 K), which bodes well for the applicability of the HTE model.

The limited overlap between our experimental range and the supposedly interesting region becomes most clear when considering the ED model (green line on Figure 4.6c). The model only overlaps with about half of the data within the range where the lattice subtraction works well, and the major features of the model lie outside our experimental range. The model's range is determined by that of Blöthe's ED data, why the model is not easily extended. Despite that, the ED model captures the behaviour at the lowest $T$ slightly better than the HTE model and yields approximately the same $J$-value (see Table 5.1), which suggests that the ED model is rather robust.

Both $C$-models gives results to three significant features, based on the statistical uncertainties on the fit parameters, which is an accuracy close to one order of magnitude larger than typically reported[34,83,84]. However, the models visually fit the data quite well, thus the accuracy is not necessarily overestimated. Still, the discrepancy between $\chi$- and $C$-results maybe tells that the precision is off, even if the accuracy is well estimated.

### 5.1.2 Ni-LDH

Our experimental data on Ni-LDH can be found on Figures 4.3, 4.6b, 4.7 and 4.9 for $\chi$-, $C$-, diffraction and spectroscopy data respectively. The various obtained parameters can be found in Table 5.1, from which one can see that modelling of both the $\chi$- and $C$-data yielded ferromagnetic $J$-values.

I measured Ni-LDH's susceptibility with a VSM using three different applied fields: 0.01 T, 0.1 T and 1 T. From Figure 4.2 it was quickly clear that the 0.01 T data, like for Cu-LDH, had a significantly worse S/N-ratio, why that data set was not considered any further. The other two were modelled with Curie-Weiss and scaling models (eqs. (2.4.18) and (2.4.27)), which both yielded positive $J$'s, but failed to capture the local maximum in $\chi T$ at $T \approx 8$ K. It is worth to notice that the maximum is not visible on the $\chi^{-1}$-axis, where the scaling and CW models are nearly indistinguishable. This again emphasises the need for plotting $\chi T$ in addition to $\chi^{-1}$ when treating susceptibility data. Since the scaling model is valid to low $T$[32], contrary to the CW model, a MF perturbation of the form in eq. (2.4.28), designed to account for AFM interchain interactions, was added to the scaling model. This made the model fit the local maximum as seen in Figure 4.3d.

The modelling of the $H = 0.1$ T and $H = 1$ T data sets yielded slightly different results, why they each have a column in Table 5.1. The difference is presumably caused be the 1 T data reaching magnetic saturation at low $T$, as seen on Figure 4.1, which means that only data at $T > 5$ K can be used in that case. The impact of this on the modelling can e.g. be seen by comparing the inserts on Figures 4.3a and 4.3d, from which it is clear that a lack of data below 5 K makes the fit worse. Also, scaling of the uncertainties by $c/\sqrt{T}$ was necessary for the $H = 0.1$ T data. Still, the fact that the two data sets give similar results despite these issues tells that the rather unconventional way of estimating the uncertainties, as described in the beginning of the Discussion, may have some merit.

The heat capacity data initially confirmed the idea that exchange interactions governed the magnetism, as I was able to model the low-$T$ heat capacity with a model built on Blöthe's ED results on finite chains[37]. The model fit the data nicely at the lowest $T$, but failed to capture a broad feature between 10 K and 30 K. It also predicted a slightly lower $J$-value than the $\chi$-data, but overall the picture of a ferromagnetic QSC persisted.

However, the neutron scattering data on Ni-LDH tells a different story. Magnetic signals were completely absent in our diffraction data, as the difference between low- and high-$T$ data was indistinguishable from Gaussian noise as shown in Figure 4.8. This means that little to no spatial spin correlations are present at $T = 1.6$ K, and that a transition to long-range magnetic order happens at a much lower temperature, if it occurs at all, since we would observe magnetic critical scattering if magnetic ordering was eminent[85]. This can either be a sign of a good realisation of a low-D Heisenberg spin systems, as they do not order at any finite temperature according to the Mermin-Wagner theorem[13], or a sign of the spin-spin interactions being different than modelled with the CW and

scaling models, as one would expect spin-spin correlations to be present at temperatures comparable to $J$. On a different note, our diffraction data revealed a significant, non-flat background at all $T$ (see Figure 4.7), which presumably is incoherent $^1$H-scattering from incomplete deuteration of our sample.

What is really interesting is the discrepancy between the NN exchange-based modelling of the bulk properties and the neutron spectroscopy results. The apparent absence of inelastic magnetic signals from spin-spin correlations, such as diffuse scattering originating from the out-smearing of SW-like signals due to a lack of long-range order and powder averaging, is somewhat surprising. Even in the paramagnetic phase, the spins should precess in the fields produced by their neighbours, and one would expect diffuse scattering smeared out along the $E$-axis with a height defined by the SW dispersion.

Instead of the expected "blob", we found an intense, $|q|$-independent signal at $E = 0.8261(17)$ meV; a clear sign of a crystal field excitation. I found that it's intensity decreases with increasing $|q|$, as expected from the magnetic form factor of nickel, which confirms it's magnetic nature. In addition, integration over $E = 0.30 - 0.59$ meV revealed that some intensity is present at low $E$, although it did not seem to depend on either $|q|$ or temperature. Since it does not decrease with increasing $|q|$, it is presumably not of magnetic origin, but it is difficult to say for certain. As of right now, we have no reason to believe it is anything other than broadening of the elastic line. However, there is no doubt about the existence of an excitation coming from a ZFS.

Thus, spin-spin correlations in Ni-LDH either scatter very little, or they are hidden inside the thermal broadening of the elastic scattering ($E_{elas} < 0.25$ meV), since they are not visible in our experiment. If the latter is the case, we can, if the correlations are assumed to be ferromagnetic and one-dimensional, put an upper bound of $J < E_{elas}/(4S) = 0.0625\,\text{meV} = 0.725$ K on the exchange constant. In that case, one could lift the excitations out of the elastic line by application of an external $B$-field, as that simply adds a constant energy to the dispersion as described by eq. (2.5.18).

These neutron scattering results made me rethink the previous data treatment. On top of the exchange-based modelling discussed above, I now modelled both the susceptibility and heat capacity with ZFS-models (eqs. (2.4.29) and (2.4.43) respectively). These proved to be equally good at describing the bulk measurements when compared to the exchange-based models, or even better in the case of the susceptibility, as seen on Figures 4.3b and 4.6b. In addition to the improved fit quality, scaling of the uncertainties was not needed for obtaining a meaningful fit when fitting the $H = 0.1$ T susceptibility data. However, the ZFS susceptibility fit predicts $|D| = 19 - 24$ K depending on the applied field, a quite different value than measured with neutron spectroscopy. Once again, the uncertainties of the fit parameters were estimated from the $\pm 33$ % background changes, since the statistical uncertainties from the fit still were not trustworthy. The heat capacity estimate comes a lot closer with $D = 8.19(5)$ K, but the introduction of a large background

parameter is needed for obtaining a meaningful fit, which might be due to the issues with extracting the magnetic signal.

In reality, the magnetism of Ni-LDH is probably not governed completely by either nearest-neighbour exchange or zero-field splitting, but rather a mixture of the two. It is hard to imagine otherwise when both types of modelling seems to fit the data, especially since the various experiments do not agree on the magnitudes of either $D$ nor $J$. However, we do not have the proper model for fitting this case; adding a NN exchange to the ZFS susceptibility model as a perturbation did not improve the model.

Still, it is worth noting that two sets of intrinsically different models, based on respectively NN exchange and a ZFS, can model experimental data to roughly the same level of success. It certainly illuminates the limitations on the insight model-based data treatment can provide, and underlines the necessity of experimental methods like neutron scattering, which directly measures the involved energies instead of parametrizing them.

### 5.1.3 Co-LDH

Our susceptibility and heat capacity data for Co-LDH can be found in Figures 4.5 and 4.6e respectively, and the parameters obtained from the different models can be found in Table 5.1. In contrast to the two other compounds, Co-LDH proved to have antiferromagnetic nearest neighbour couplings, why scaling model results are absent from Table 5.1, as that model is derived for ferromagnetic chains only.

For an unknown reason, extraction of the magnetic heat capacity signal worked even more poorly for Co-LDH than for the others. At the lowest $T$, a minuscule magnetic signal seems to add to a constant contribution $C_0 \approx 0.2$ J/(mol K), which suddenly disappears at $T \geq 22$ K. Despite that, the HTE model (eq. (2.4.42), now with an added constant parameter) proved to be a good fit to data at $T \leq 22$ K, given the same caveats as described for the HTE fit to Cu-data (except for the considerations regarding bayerite). The obtained parameter is found in Table 5.1. Given this result, the ED model only overlapped with six data points, thus reporting results from that method is redundant. The HTE result is, like the HTE-result for Cu-LDH, accurate to three significant figures, thus the discussion on parameter accuracy from the Cu-data is also applicable here.

Getting consistent results from the Co-LDH susceptibility data was not an easy task. Raw data measured at respectively $H = 0.01$, 0.1 and 1 T did not behave in the same manner at high $T$ (see Figure 4.5a), contrary to expectation for a material in a paramagnetic state. Like for the other samples, the $H = 0.01$ T data was discarded due to the much worse S/N-ratio, but I still fitted CW models to the $H = 0.1$ T and $H = 1$ T data, despite the aforementioned oddity, since the inverse susceptibilities seemed to behave linearly. The $H = 0.1$ T data yielded no consistent result, since my choice of lower fit boundary always had a large impact on the obtained parameters, why $H = 0.1$ T data will no be discussed any further. Only considering the high-field data should not

be problematic, since my estimate is that being at the edge of the linear regime only disqualifies data below $T = 2.44$ K in this case, thus almost all available data is usable, and no significant features lie outside the usable range.

I was able to reproduce the high-temperature region of the $H = 1$ T data by fitting a CW model (see Figure 4.5b), and I was even able to give a best estimate of $J = -6.26(2)$ K. However, this results is not given in Table 5.1, as a ZFS-model (eq. (2.4.30)) proved much more successful in describing the high-$T$ data ($T \geq 7.5$ K, black line on Figure 4.5c) and yielded $D = 125(2)$ K. Also, the heat capacity data (Figure 4.6e) suggests that $J$ is two orders of magnitude smaller than the high-T CW prediction, why I am confident that the ZFS governs the susceptibility at high $T$. Also, density functional theory calculations by J. Vaara and A.B.A. Andersen predicts a large, positive $D$-parameter[62].

However, the ZFS-model was not able to reproduce the $\chi$-behaviour at the lowest $T$. I tried to model the low-$T$ data in two ways: By fitting a CW model to it, inspired by Sandberg et al's success with this method in describing the low-$T$ susceptibility of YbGG[72], and by adding a MF perturbation, in the form of eq. (2.4.28), to the ZFS-model and fitting the whole experimental range. The CW model fits the data nicely at $T \leq 7.5$ K and yielded $-J = 0.075 - 0.16$ K depending on the choices of $g$ and $S$, which are interdependable in the CW model, while $J$ only depends on $S$. This result is in compliance with the HTE-fit to heat capacity data. Adding the MF perturbation made the ZFS-fit even better (red line on Figure 4.5c); the parameters obtained from this model are tabulated in Table 5.1. It also yields a $J$ in compliance with CW and heat capacity results. I was not able to fit a ZFS-model to the heat capacity data, as the features of such a model lie outside the $T$-range where the extraction of $C_{mag}$ works well; for $D \approx 130$ K, the maximum lies at $T \approx 50$ K, way above the the useable range $T \leq 22$ K.

The choice of $g$ for the low-$T$ CW fit is an interesting discussion. On one hand, preliminary EPR results (see Appendix A) suggests an isotropic $g_{iso} \approx 2.9$ in compliance with the ZFS-model. However, the ZFS-values for the components of $\underline{\mathbf{g}}$ ($g_\perp = 2.81(2)$ and $g_\parallel = 3.02^{+0.14}_{-0.17}$) do no in any way match the EPR results (resonances at $g \approx 2$ and $g \approx 5$). Locking $g = 2.9$ in the low-$T$ CW model yielded $S = 1.1$, a value quite different from the expected $S = 3/2$, but yields $J \approx -0.16$ K, which is the closest the low-$T$ CW model comes to the ZFS result. Locking $S = 3/2$ and fitting $g$ yielded $g \approx 2.28$, which is quite different from isotropic value predicted by the ZFS-model, but gives $J \approx -0.075$ K in compliance with the HTE fit to heat capacity data. Preliminary density functional theory (DFT) calculations by J. Vaara (Univ. of Oulu) and A.B.A. Andersen (Univ. of Southern Denmark) yields $g_{iso} = 2.42$, which do not agree with either method. However, DFT yields $g_z = 2.8$, which is rather close to the isotropic ZFS value. Due to these challenges, giving precise estimates of $J$ and $g$ from $\chi$-data is not possible, but estimations of $J \sim -0.1$ K and $g \sim 2.3$ can be justified.

## 5.2 Conclusion

In conclusion, I have managed to shed light on the magnetic properties of a family of layered double hydroxides not previously studied. I found that Cu-LDH is a ferromagnetic $S = 1/2$ spin chain, and my best estimate of the exchange parameter is $J = 1.4(3)$ K, based on fitting a non-critical scaling model to susceptibility data measured at $H = 0.1$ T. Ni- and Co-LDH proved to have significant zero-field splittings which govern their magnetism, while the exchange interaction seems to play a smaller role.

For Ni-LDH, neutron spectroscopy revealed a zero-field splitting $D = -9.59(2)$ K, where knowledge of the sign of $D$ comes from modelling of susceptibility and heat capacity data, and from DFT calculations performed by J. Vaara and A.B.A. Andersen, which all agreed on $D < 0$. However, neither method estimated the same magnitude of $D$ as found from the direct measurement, and $\chi$-modelling yielded some questionable values for $g_\perp$ and $g_\parallel$. Furthermore, models based purely on the Heisenberg Hamiltonian were also capable of fitting the bulk data. Despite not agreeing on the exact magnitude of $J$, they all predicted $J > 0$. For these reasons, I am confident that both the ZFS and the exchange interaction need to be considered in regard to the magnetic properties of Ni-LDH. Modelling $C$ and $\chi$ with a combined model, while locking $D$ to the spectroscopy value, would be a clear next step, but is unfortunately outside the scope of this work.

For Co-LDH, I found that consideration of both the ZFS and exchange interactions was necessary for modelling the bulk magnetic properties. By modelling the susceptibility with a ZFS model with a mean-field exchange interaction incorporated as a perturbation, I found $D = 138^{+5}_{-3}$ K. Different suscpetibility and heat capacity models yielded slightly different results for the exchange parameter, but all agreed on an antiferromagnetic interaction of the order $J \approx -0.1$ K.

Aside from knowledge on my samples, I learnt several other valuable lessons during this work. First and foremost, my treatment of the susceptibility data, on several occasions, underlined the necessity for plotting $\chi T$, since important features can be hidden when only considering the traditional $\chi^{-1}$-plots. I learnt that one should be weary about the choice of applied field when performing experiments with a vibrating sample magnetometer, and that $H = 0.1$ T is generally a good choice. Furthermore, I experienced that extraction of the magnetic part of heat capacity data can be a more difficult task than anticipated.

On a more general note, my work is a good example of a model not necessarily being well suited to describe data, even if it is physically reasonable and fits the data well. In the case of Ni-LDH, it was not until less than a week before deadline that neutron spectroscopy revealed that a ZFS had to be taken into account, despite Heisenberg models fitting the data nicely. The fact that two intrinsically different sets of models were able to reproduce the Ni-LDH bulk data is indeed a lesson that will linger with me, and it certainly underlines the strength of experimental methods that can measure the involved energies directly instead of parametrising them.

All in all, I cannot cannot conclude anything final about the general QSC nature of M(II)$Al_4$-LDHs. What I can say is that none of the three samples I studied order magnetically above $T = 2$ K, and in all cases the spins only couple weakly. I provided some good estimates of some of the magnetic parameters, but further studies are needed, as expected for a completely new set of compounds. I will elaborate on that in the outlook below, but I will say one thing: Experiments at dilution temperatures are a must if we truly want to understand these compounds.

## 5.3 Outlook

As is always the case at the start of any project, the first round of results spark new ideas and ask new questions, and this project is no different. Here, I try to outline some of the most interesting ideas for the continuation of this work.

First of all, direct measurements of the crystal field energy levels in Co-LDH, like the one obtained for Ni-LDH at FOCUS, would be of great interest. This would allow us to compare the estimates from $\chi$- and $C$-modelling to direct measurements. Such an experiment could be performed on the neutron TOF spectrometer IN5 at Institute Laue-Langevin in Grenoble[86], which I conveniently will be connected to from February 1st, as the instrument responsible Jacques Ollivier will be my ILL PhD supervisor.

Furthermore, it could be interesting to investigate spin-spin interactions in the LDHs, especially for the Ni- and Co-variants. So far, my results suggest that the involved energies are tiny, why extra measures would have to be taken in order to lift the scattering signals out of the elastic line if one were to measure the dynamics with neutron spectroscopy. This could be done by performing the experiments in an applied field, as it defines the lower energy of the spin-wave dispersion. At $H = 1$ T, the lower boundary would be $g\mu_B B = 115.8$ $\mu$eV, which is just outside of IN5's elastic energy resolution of $\sim 100$ $\mu$eV[86]. In that case, the top of the excitation would maximally be at $(0.1158 + 4 \cdot 0.0625)$ meV $= 0.366$ meV, assuming that Ni-LDH has the strongest exchange and that my upper bound on $J$ is true. This way, the excitations will not overlap with the ZFS excitations.

If we were able to produce single crystals, the possibilities would be even greater. In addition to the possibility for more advanced neutron spectroscopy experiments, we would be able to directly measure the components of $\underline{\mathbf{g}}$, which could be compared to our bulk estimates, and allow us to to estimate the magnitude of the spin-orbit coupling if we had been able to measure $D$ directly as mentioned above.

# Bibliography


[1] "Nobel prize in physics 2014." `NobelPrize.org`. Accessed 30th Oct 2020.

[2] "Nobel prize in physics 2016." `NobelPrize.org`. Accessed 30th Oct 2020.

[3] "Nobel prize in chemistry 2011." `NobelPrize.org`. Accessed 30th Oct 2020.

[4] "Nobel prize in chemistry 2016." `NobelPrize.org`. Accessed 30th Oct 2020.

[5] "Nobel prize in chemistry 2019." `NobelPrize.org`. Accessed 30th Oct 2020.

[6] F. Cavani, F. Trifirò, and A. Vaccari, "Hydrotalcite-type anionic clays: Preparation, properties and applications.," *Catalysis Today*, vol. 11, no. 2, p. 173, 1991.

[7] G. Fan, F. Li, D. G. Evans, and X. Duan, "Catalytic applications of layered double hydroxides: recent advances and perspectives," *Chemical Society Reviews*, vol. 43, p. 7040, 2014.

[8] M. Shao, R. Zhang, Z. Li, M. Wei, D. G. Evans, and X. Duan, "Layered double hydroxides toward electrochemical energy storage and conversion: design, synthesis and applications," *Chemical Communications*, vol. 51, p. 15880, 2015.

[9] J.-M. Oh, S.-J. Choi, G.-E. Lee, S.-H. Han, and J.-H. Choy, "Inorganic drug-delivery nanovehicle conjugated with cancer-cell-specific ligand," *Advanced Functional Materials*, vol. 19, no. 10, p. 1617, 2009.

[10] S. S. C. Pushparaj, N. D. Jensen, C. Forano, G. J. Rees, V. Prevot, J. V. Hanna, D. B. Ravnsbæk, M. Bjerring, and U. G. Nielsen, "Structural investigation of Zn(II) insertion in bayerite, an aluminum hydroxide.," *Inorganic chemistry*, vol. 55, no. 18, p. 9306, 2016.

[11] F. C. Hawthorne and M. A. Cooper, "The crystal structure of chalcoalumite: mechanisms of Jahn-Teller-driven distortion in $^{[6]}Cu^{2+}$-containing oxysalts," *Mineralogical Magazine*, vol. 77, p. 2901, 2013.

[12] M. Mourigal, M. Enderle, A. Klöpperpieper, J.-S. Caux, A. Stunault, and H. M. Rønnow, "Fractional spinon excitations in the quantum Heisenberg antiferromagnetic chain," *Nature Physics*, vol. 9, p. 435, 2013.

[13] N. D. Mermin and H. Wagner, "Absence of ferromagnetism or antiferromagnetism in one- or two-dimensional isotropic Heisenberg models," *Physical Review Letters*, vol. 17, p. 1133, 1966.

[14] P. W. Anderson, "An approximate quantum theory of the antiferromagnetic ground state," *Physical Review*, vol. 86, p. 694, 1952.

[15] K. Momma and F. Izumi, "Vesta 3 for three-dimensional visualization of crystal, volumetric and morphology data," *Journal of Applied Crystallography*, vol. 44, p. 1272, 2011.

[16] K. Yosida, *Theory of Magnetism*. Springer, 1996.

[17] S. Blundell, *Magnetism in Condensed Matter*. Oxford University Press, 2001.

[18] D. J. Griffith, *Introduction to Quantum Mechanics*. Pearson Education, 2nd ed., 2015.

[19] D. J. Griffith, *Introduction to Electrodynamics*. Prentice Hall, 1999.

[20] K. Lefmann, *Neutron Scattering: Theory, Instrumentation and Simulation*. Lecture Notes, University of Copenhagen, 2018.

[21] L. Landau, "On the theory of phase transitions," *Zh. Eksp. Teor. Fiz.*, no. 7, p. 19, 1937.

[22] B. M. Andersen, "Condensed matter physics 2," 2016. Lecture Notes, University of Copenhagen.

[23] G. D. DeFotis, R. Weise, and C. Scherrer, "$MnCl_2 \cdot H_2O$: A quasi-one-dimensional Heisenberg antiferromagnet," *Journal of Applied Physics*, vol. 67, p. 5857, 1990.

[24] M. E. Fisher, "Magnetism in one-dimensional systems – the Heisenberg model for infinite spin," *American Journal of Physics*, vol. 32, p. 343, 1964.

[25] T. Smith and S. A. Friedberg, "Linear chain antiferromagnetism in $CsMnCl_3 \cdot 2\,H_2O$," *Physical Review*, vol. 176, p. 660, 1968.

[26] P. Nordblad, L. Lundgren, E. Figueroa, and O. Beckman, "Specific heat and magnetic susceptibility of $MnF_2$ and $Mn_{0.98}Fe_{0.02}F_2$ near $T_n$," *Journal of Magnetism and Magnetic Materials*, vol. 23, p. 333, 1981.

[27] P. Nordblad, L. Lundgren, E. Figueroa, U. Gäfvert, and O. Beckman, "Critical behaviour of the magnetic susceptibility of $MnF_2$, near the Néel point," *Physica Scripta*, vol. 20, p. 105, 1979.

[28] J. B. Goodenough, "Theory of the role of covalence in the perovskite-type manganites $[La, M(II)]MnO_3$," *Physical Review*, vol. 100, p. 564, 1955.

[29] J. Kanamori, "Superexchange interaction and symmetry properties of electron orbitals," *Journal of Physics and Chemistry of Solids*, vol. 10, p. 87, 1959.

[30] R. Boča, "Zero-field splitting in metal complexes," *Coordination Chemistry Reviews*, vol. 248, no. 9, p. 757, 2004.

[31] P. M. Schosseler, "Basic concepts of EPR." (https://epr.ethz.ch/education/basic-concepts-of-epr/one-elect–in-the-magn–field/cf-split–so-coupl-.html), *ETH Zürich*. Accessed 2nd Jul 2020.

[32] J. Souletie, P. Rabu, and M. Drillon, "Ferromagnetic Heisenberg chains: A description of the magnetic susceptibility from a noncritical scaling approach," *Physical Review B*, vol. 72, p. 214427, 2005.

[33] J. C. Bonner and M. E. Fisher, "Linear magnetic chains with anisotropic coupling," *Physical Review*, vol. 135, p. A640, 1964.

[34] J. N. McElearney, D. B. Losee, S. Merchant, and R. L. Carlin, "Antiferromagnetic ordering and crystal field behavior of $NiCl_2 \cdot 4\,H_2O$," *Physical Review B*, vol. 7, p. 3314, 1973.

[35] S. Ostrovsky, W. Hasse, M. Drillon, and P. Panissod, "Role of dipolar interactions in three-dimensional magnetic ordering of chain compounds with very large interchain spacing," *Physical Review B*, vol. 64, p. 134418, 2001.

[36] L. J. D. Jongh and A. R. Miedema, "Experiments on simple magnetic model systems," *Advances in Physics*, vol. 50, no. 8, p. 947, 2001.

[37] H. W. J. Blöte, "The heat capacities of linear Heisenberg chains," *Physica*, vol. 78, no. 2, p. 302, 1974.

[38] H. W. J. Blöte, "The specific heat of magnetic linear chains," *Physica B+C*, vol. 79, no. 5, p. 427, 1975.

[39] J. des Cloizeaux and J. J. Pearson, "Spin-wave spectrum of the antiferromagnetic linear chain," *Physical Review*, vol. 128, no. 5, p. 2131, 1962.

[40] F. D. M. Haldane, "Nonlinear field theory of large-spin Heisenberg antiferromagnets: Semiclassically quantized solitons of the one-dimensional easy-axis Néel state," *Physical Review Letters*, vol. 50, p. 1153, 1983.

[41] F. D. M. Haldane, "O(3) nonlinear $\sigma$ model and the topological distinction between integer- and half-integer-spin antiferromagnets in two dimension," *Physical Review Letters*, vol. 61, no. 8, p. 1029, 1988.

[42] A. Vasiliev, O. Volkova, E. Zvereva, and M. Markina, "Milestones of low-d quantum magnetism," *npj Quantum Materials*, vol. 3, p. 18, 2018.

[43] D. S. Inosov, "Quantum magnetism in minerals," *Advances in Physics*, vol. 67, no. 3, p. 149, 2018.

[44] D. A. Yablonskiy, "Tyablikov approximation in the theory of low-dimensional quantum Heisenberg ferromagnets and antiferromagnets," *Physical Review B*, vol. 44, no. 9, p. 4467, 1991.

[45] H. Bethe, "Zur theorie der metalle," *Zeitschrift für Physik*, vol. 71, p. 205, 1931.

[46] L. Hulthén, "Über das austauschproblem eines kristalles," *Arkiv för matematik, astronomi och fysik*, vol. 26A, no. 11, 1938.

[47] L. D. Faddeev and L. A. Takhtajan, "What is the spin of a spin wave?," *Physics Letters A*, vol. 85A, no. 6-7, p. 375, 1981.

[48] G. Müller, H. Thomas, H. Beck, and J. C. Bonner, "Quantum spin dynamics of the antiferromagnetic linear chain in zero and nonzero magnetic field," *Physical Review B*, vol. 24, no. 3, p. 1429, 1981.

[49] A. H. Bougourzi, M. Couture, and M. Kacir, "Exact two-spinon dynamical correlation function of the one-dimensional Heisenberg model," *Physical Review B*, vol. 54, no. 18, p. R12 669, 1996.

[50] J. S. Caux and R. Hagemans, "The four-spinon dynamical structure factor of the Heisenberg chain," *Journal of Statistical Mechanics: Theory and Experiment*, p. 12013, 2006.

[51] J. J. B. Torrance and M. Tinkham, "Excitation of multiple-magnon bound states in $CoCl_2 \cdot 2\,H_2O$," *Physical Review*, vol. 187, no. 2, p. 595, 1969.

[52] I. Affleck, T. Kennedy, E. H. Lieb, and H. Tasaki, *Valence Bond Ground States in Isotropic Quantum Antiferromagnets*, p. 253. Springer Berlin Heidelberg, 2004.

[53] I. Affleck and R. A. Weston, "Theory of near-zero-wave-vector neutron scattering in Haldane-gap antiferromagnets," *Physical Review B*, vol. 45, no. 9, p. 4667, 1992.

[54] M. D. P. Horton and I. Affleck, "Three-magnon contribution to the spin correlation function in integer-spin antiferromagnetic chains," *Physical Review B*, vol. 60, no. 17, p. 11891, 1999.

[55] I. A. Zaliznyak, S.-H. Lee, and S. V. Petrov, "Continuum in the spin-excitation spectrum of a Haldane chain observed by neutron scattering in $CsNiCl_3$," *Physical Review Letters*, vol. 87, p. 017202, 2001.

[56] M. Kenzelmann, R. A. Cowley, W. J. L. Buyers, R. Coldea, J. S. Gardner, M. Enderle, D. F. McMorrow, and S. M. Bennington, "Multiparticle states in the S=1 chain system $CsNiCl_3$," *Physical Review Letters*, vol. 87, no. 1, p. 017201, 2001.

[57] H.-J. Wang, Y. Chen, L.-J. Fu, R.-N. Lin, and C.-C. Song, "The paramagnetic properties of one-dimensional spin-1 single-ion anisotropic ferromagnet," *Journal of Magnetism and Magnetic Materials*, vol. 321, p. 1904, 2009.

[58] J. Deisz, M. Jarrell, and D. L. Cox, "Dynamical properties of one-dimensional antiferromagnets: A monte carlo study," *Physical Review B*, vol. 48, p. 10227, 1993.

[59] S. Itoh, Y. Endoh, K. Kakurai, H. Tanaka, and T. G. Perring, "Temperature dependence of spin dynamics in the s = 3/2 Heisenberg antiferromagnetic chain $CsVCl_3$," *Physica B: Condensed Matter*, vol. 241, p. 546, 1997.

[60] N. D. Jensen, N. T. T. Duong, R. Bolanz, Y. Nishiyama, C. A. Rasmussen, J. Gottlicher, R. Steininger, V. Prevot, and U. G. Nielsen, "Synthesis and structural characterization of a pure $ZnAl_4(OH)_{12}SO_4 \cdot 2.6\,H_2O$ layered double hydroxide," *Inorganic Chemistry*, vol. 58, no. 9, p. 6114, 2019.

[61] Y. A. Uvarova, E. Sokolova, F. C. Hawthorne, V. V. Karpenko, A. A. Agakhanov, and L. A. Pautov, "The crystal chemistry of the 'nickelalumite'-group minerals," *The Canadian Mineralogist*, vol. 43, no. 5, p. 1511, 2005.

[62] A. B. A. Andersen, R. Tang, S. Janas, H. Jacobsen, D. Cheptiakov, J. P. Embs, J. Vaara, K. Lefmann, and U. G. Nielsen, "Synthesis, characterization, and magnetic properties of $MAl_4(OH)_{12}SO_4 \cdot 3\,H_2O$ with M = $Co^{2+}$, $Ni^{2+}$ and $Cu^{2+}$ : A novel class of 1D spin chains," in preparation.

[63] S. Foner, "Versatile and sensitive vibrating-sample magnetometer," *Review of Scientific Instruments*, vol. 30, no. 7, p. 548, 1959.

[64] Quantum Design, *PPMS® Dynacool™ Product Description.* 1307-010 Rev. E0.

[65] Quantum Design, *Vibrating Sample Magnetometer*. 1084-500 Rev. B0.

[66] T. Chatterji, *Neutron Scattering from Magnetic Materials*. Elsevier, 2006.

[67] G. L. Squires, *Introduction to the theory of Thermal Neutron Scattering*. Cambridge University Press, 2012.

[68] "HRPT instrument description." `https://www.psi.ch/en/sinq/hrpt/description`. Accessed 20th Oct 2020.

[69] B. T. M. Willis and C. J. Carlile, *Experimental Neutron Scattering*. Oxford University Press, 2009.

[70] "FOCUS instrument description." `https://www.psi.ch/en/sinq/focus/description`. Accessed 10th Oct 2020.

[71] G. A. Bain and J. F. Berry, "Diamagnetic corrections and Pascal's constants," *Journal of Chemical Education*, vol. 85, p. 532, 2008.

[72] L. Ørduk Sandberg, R. Edberg, K. S. Pedersen, M. C. Hatnean, G. Balaskrishnan, L. Mangin-Thro, A. Wildes, B.Fåk, G. Ehlers, G. Sala, P. Henelius, K. Lefmann, and P. P. Deen, "Emergent magnetic behaviour in the frustrated $Yb_3Ga_5O_{12}$ garnet," *arXiv:2005.10605*, 2020.

[73] "NIST/SEMATECH e-handbook of statistical methods, section 1.3.5.14." `https://doi.org/10.18434/M32189`. Accessed 2nd Nov 2020.

[74] "Mslice web page." `http://mslice.isis.rl.ac.uk/Main_Page`. Accessed 17th Dec 2020.

[75] R. Azuah, L. Kneller, Y. Qiu, P. Tregenna-Piggott, C. Brown, J. Copley, and R. Dimeo, "DAVE: A comprehensive software suite for the reduction, visualization, and analysis of low energy neutron spectroscopic data," *Journal of Research of the National Institute of Standards and Technology*, vol. 114, no. 6, p. 341, 2009.

[76] S. Janas, *Neutron spectroscopy studies of geometrically frustrated antiferromagnets*. PhD thesis, University of Copenhagen, 2020.

[77] K. Lefmann. Personal communication.

[78] H. A. Mook, "Magnetic moment distribution of nickel metal," *Physical Review*, vol. 148, p. 495, 1966.

[79] R. Nathans, C. Shull, G. Shirane, and A. Andresen, "The use of polarized neutrons in determining the magnetic scattering by iron and nickel," *Journal of Physics and Chemistry of Solids*, vol. 10, no. 2, p. 138, 1959.

[80] H. Jacobsen. Personal communication.

[81] S. Pagola, K. T. Trowell, K. C. Havas, Z. D. Reed, D. G. Chan, M. J. Van Dongen, and G. C. DeFotis, "Crystal structures of manganese and cobalt dichloride monohydrate and deuteration effects on magnetic behavior," *Inorganic Chemistry*, vol. 52, no. 23, p. 13341, 2013.

[82] R. J. Barlow, *Statistics: A guide to the use of statistical methods in the physical sciences*. Wiley, 1989.

[83] D. Moses, H. Shechter, E. Ehrenfreund, and J. Makovsky, "Magnetic specific heat of the nearly one-dimensional antiferromagnet CsNiCl3," *Journal of Physics C: Solid State Physics*, vol. 10, no. 3, p. 433, 1977.

[84] J. A. Lukin, S. A. Friedberg, and G. C. DeFotis, "Quasi-one-dimensional antiferromagnetism in $MnCl_2 \cdot H_2O$," *Journal of Applied Physics*, vol. 69, no. 8, p. 5807, 1991.

[85] M. F. Collins, *Magnetic Critical Scattering*. Oxford University Press, 1989.

[86] "IN5 instrument description." `https://www.ill.eu/users/instruments/instruments-list/in-5/characteristics`. Accessed 19th Dec 2020.

# Appendix A

# EPR

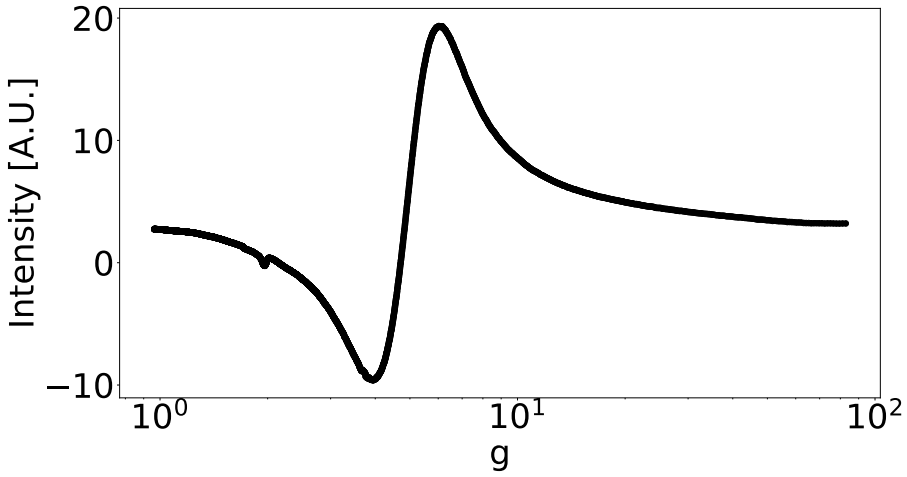


Figure A.1: Raw EPR spectroscopy data of Co-LDH on a logarithmic x-axis measured at $T = 10(1)$ K in the range $B = 80 - 6880$ Oe using a radio wave with $f = 9.64$ GHz. The peaks are situated at $g \approx 2$ and $g \approx 5$. The spectrum is captured in derivative mode.

Electron paramagnetic resonance spectroscopy of Co-LDH (Figure A.1) was measured at $T = 10(1)$ K using a radio-wave with $f = 9.64$ GHz and field strengths in the range $B = 80 - 6880$ Oe. The measurements were performed with the assistance of Prof. Jesper Bendix from the chemistry department at the Univeristy of Copenhagen using their in-house EPR apparatus. The field strengths are translated into $g$-values by the formula

$$g = \frac{hf}{\mu_B B} \tag{A.1}$$

where $h$ is Planck's constant. The peaks are centred around at $g \approx 2$ and $g \approx 5$. Susceptibility data predicts a large ZFS-parameter $D = 138^{+5}_{-3}$ K, which according to Boča means that the $m_S = \pm 1/2$ Kramer's doublet of the $S = 3/2$ ion has the lowest energy [30].

Only transitions with $\Delta m_S = 1$ are allowed in EPR spectroscopy, thus only the transitions $m_S = -1/2 \leftrightarrow m_S = 1/2$, $m_S = -3/2 \leftrightarrow m_S = -1/2$ and $m_S = 1/2 \leftrightarrow m_S = 3/2$ are allowed. The resonance at $g \approx 2$ probably corresponds to the $m_S = -1/2 \leftrightarrow m_S = 1/2$, but the other allowed transitions are not visible if the susceptibility result is even approximately true, as EPR with $f \approx 9$ GHz only probes energy levels split by $E < 0.5$ K[30].